NASA/CR–2014-218146

Investigation of Active Flow Control to Improve Aerodynamic Performance of Oscillating Wings

Robert P. Narducci
The Boeing Company, Philadelphia, Pennsylvania

Rodney Bowersox
Texas A&M University, College Station, Texas

Richard Bussom and Michael McVeigh
The Boeing Company, Philadelphia, Pennsylvania

Surya Raghu
Advanced Fluidics, LLC, Elliott City, Maryland

Edward White
Texas A&M University, Philadelphia, Pennsylvania

January 2014

NASA STI Program . . . in Profile

Since its founding, NASA has been dedicated to the advancement of aeronautics and space science. The NASA scientific and technical information (STI) program plays a key part in helping NASA maintain this important role.

The NASA STI program operates under the auspices of the Agency Chief Information Officer. It collects, organizes, provides for archiving, and disseminates NASA's STI. The NASA STI program provides access to the NASA Aeronautics and Space Database and its public interface, the NASA Technical Report Server, thus providing one of the largest collections of aeronautical and space science STI in the world. Results are published in both non-NASA channels and by NASA in the NASA STI Report Series, which includes the following report types:

- TECHNICAL PUBLICATION. Reports of completed research or a major significant phase of research that present the results of NASA Programs and include extensive data or theoretical analysis. Includes compilations of significant scientific and technical data and information deemed to be of continuing reference value. NASA counterpart of peer-reviewed formal professional papers, but having less stringent limitations on manuscript length and extent of graphic presentations.

- TECHNICAL MEMORANDUM. Scientific and technical findings that are preliminary or of specialized interest, e.g., quick release reports, working papers, and bibliographies that contain minimal annotation. Does not contain extensive analysis.

- CONTRACTOR REPORT. Scientific and technical findings by NASA-sponsored contractors and grantees.

- CONFERENCE PUBLICATION. Collected papers from scientific and technical conferences, symposia, seminars, or other meetings sponsored or co-sponsored by NASA.

- SPECIAL PUBLICATION. Scientific, technical, or historical information from NASA programs, projects, and missions, often concerned with subjects having substantial public interest.

- TECHNICAL TRANSLATION. English-language translations of foreign scientific and technical material pertinent to NASA's mission.

Specialized services also include organizing and publishing research results, distributing specialized research announcements and feeds, providing information desk and personal search support, and enabling data exchange services.

For more information about the NASA STI program, see the following:

- Access the NASA STI program home page at *http://www.sti.nasa.gov*

- E-mail your question to help@sti.nasa.gov

- Fax your question to the NASA STI Information Desk at 443-757-5803

- Phone the NASA STI Information Desk at 443-757-5802

- Write to:
  STI Information Desk
  NASA Center for AeroSpace Information
  7115 Standard Drive
  Hanover, MD 21076-1320

NASA/CR–2014-218146

Investigation of Active Flow Control to Improve Aerodynamic Performance of Oscillating Wings

Robert P. Narducci
The Boeing Company, Philadelphia, Pennsylvania

Rodney Bowersox
Texas A&M University, College Station, Texas

Richard Bussom and Michael McVeigh
The Boeing Company, Philadelphia, Pennsylvania

Surya Raghu
Advanced Fluidics, LLC, Elliott City, Maryland

Edward White
Texas A&M University, Philadelphia, Pennsylvania

National Aeronautics and
Space Administration

Langley Research Center
Hampton, Virginia 23681-2199

Prepared for Langley Research Center
under Contract NNL13AA03C

January 2014

Available from:

NASA Center for AeroSpace Information
7115 Standard Drive
Hanover, MD 21076-1320
443-757-5802

Table of Contents

List of Figures

List of Tables

Acknowledgements

The authors would like to thank Brian Allan and Susan Gorton for their expert technical guidance throughout this project. Also, we would like to thank Jamie Weber of Texas A&M University for her thorough evaluation of pressure instrumentation. Finally, we would like to acknowledge Arvin Shmilnovich and Andrew Weddle of The Boeing Company for their work in active flow control modeling in CFD.

Introduction

Future advanced civil and military rotorcraft are being designed to meet requirements to operate at high cruise speeds. In the case of commercial transport rotorcraft, this is driven by the need for increased productivity, longer range, and larger payloads; for military rotorcraft, higher speed provides reduced mission time-to-target, increased surprise, enhanced maneuver capability, and improved survival of rescued wounded personnel. For conventional helicopters, achieving these goals requires the ability to control airfoil dynamic stall that causes unfavorable changes in the blade aerodynamics and results in loss of performance and high blade loads.

Control of dynamic stall requires control of the upper-surface boundary layer. As the blade pitches, flow tends to remain attached at angles of attack greater than the stall angle of a stationary blade. However, when separation occurs, a vortex forms near the leading edge and travels along the upper surface towards the trailing edge then sheds into the wake. This dynamic stall vortex produces increases in lift and large nose-down pitching moments greater than the static values, which, in turn, produce large control loads, increased vibration, and an increase in rotor drag. The end-result is increased power-required, reduced cruise speed, increased maintenance costs and increased rotor loads that limit maneuver capability for the helicopter.

The objective of this work is to design, fabricate, and evaluate a promising active flow control (AFC) concept for application to a helicopter rotor blade to mitigate the effects of dynamic stall, which generally occurs as the blades pass through the retreating side of the rotor disk. This is a very challenging application of active flow control technology because the rotor flow environment is highly unsteady and the airfoils experience both high and low Mach number flow conditions during a single revolution.

Two types of AFC actuators are being developed in the industry: fluidic actuators and plasma actuators. This investigation focuses on the effectiveness of small fluidic actuators for controlling dynamic stall. Fluidic actuators inject high-energy air into the boundary layer using blowing to control separation. Periodic blowing requires an order-of-magnitude less power than steady blowing. Recent developments in the capabilities of fluidic actuators suggest that they may offer a very effective and practical method for on-blade control of dynamic stall. The issue of how sufficient air is provided to the actuators on the blades may be solved by developments in very compact electric blowers used in the automotive racing industry. These blowers may be able to fit in the root of a rotor blade.

Plasma actuators are attractive because they are electrically powered, compact, and conform to the airfoil surface, but have outstanding issues of operation that need to be addressed: effects of rain, EMI, resilience of the airfoil surface to the plasma, and visual detection of the corona by enemy forces. Nevertheless, experiments have demonstrated some level of dynamic stall alleviation at low-to-mid Mach numbers [1, 2]. Plasma actuators apply a high voltage between electrodes fitted flush to the airfoil surface, producing a surface layer of ionized air (plasma). In the presence of the electric field, the plasma exerts a body force on the boundary layer air to produce a chordwise tangential wall-jet that adds energy to maintain attachment.

Fluidic actuators are of two types: zero-mass-flow blowing using a vibrating membrane ('speaker' type), and sweeping-jet actuators (SJAs). The electrically powered zero-mass actuators have demonstrated improved lift and reduced drag on a VR-7 oscillating airfoil [3]. However, subsequent tests on a VR-12 blade section in the US Army 7'×10' wind tunnel did not show significant benefit [4]. In these experiments, the airfoil tended to separate suddenly from the leading edge, in contrast to prior experiments with the VR-7 section, which separated gradually from the trailing edge. The control jet, placed at 20% chord and limited to an exit jet Mach number of 0.4, could not influence an already separated boundary layer.

We have chosen to evaluate the SJA concept for this project due to its small size and potential to generate much stronger jets. The modern SJA is a simple non-mechanical device that produces a high-speed jet that oscillates from side-to-side to energize the airfoil boundary layer. These devices require no electric power, but do require a source of compressed air in the 13 psig range. Research reported in Refs [5, 6] has demonstrated suppression of separation on wings and flaps beyond what is achievable with zero-mass jets. A substantial advantage of the SJA is that each actuator can be made very small, typically about 0.1" thick, measuring approximately 0.5"×0.7" and weighing only grams. They are capable of jet speeds up to sonic velocities depending on the pressure applied. SJAs can be manufactured inexpensively and fitted into almost any object.

This report presents a plan for the experimental testing of SJAs on a VR-7 airfoil section. The plan involves the modification of the Low Speed Wind Tunnel at Texas A&M University (TAMU) so that testing can be performed at conditions up to Mach 0.5. The wind tunnel is ideally suited because, with the modifications, the facility will allow for low-cost testing of passive and active flow controlled airfoils throughout rotor-relevant Mach numbers, both statically and dynamically. The facility is equipped to make many types of flow measurements including PIV, hot film, and surface pressures so that fundamental physics can be understood. The plan is complemented by CFD analysis to provide substantiation to theories prior to wind tunnel testing and to aid in the design of the wind tunnel model.

The plan was generated by researchers from The Boeing Company, TAMU, and Advanced Fluidics, LLC. It is presented in this report, first with the overall approach, followed by designs for the wind tunnel modifications. A wind tunnel model design is presented next, followed by designs for sweeping-jet actuation. A notional run-matrix is presented, targeting a 15-day entry with an optional five additional days for PIV measurements. CFD was used to provide insight into the physics of sweeping jets for dynamic stall control on a VR-7. Details of calculations are presented before the final section, which offers recommendations and conclusions.

Technical Approach

The Boeing Company has teamed with Texas A&M University and Advanced Fluidics to develop a program to apply sweeping jet technology to mitigate the detrimental effects of retreating blade stall. The program is primarily experimental focusing on two-dimensional testing of an oscillating VR-7 airfoil section. Complementing the experimental measurements are CFD analyses.

Practical dynamic stall control for rotorcraft means achieving control across the range of reduced frequencies from 0.0 to 0.15 and Mach numbers of 0.0 to 0.5. To test at these conditions, modifications to the Texas A&M Oran W. Nicks low speed wind tunnel are necessary. The modifications reduce the test section area to achieve the desired Mach numbers. The proposed experimental tests fall into three segments: (1) a detail assessment of uncontrolled dynamic stall flow fields for the airfoil across a range of reduced frequency and Mach number; (2) experimental trade studies to optimize actuator placement and characteristics; and (3) a detailed assessment of controlled dynamic stall flow fields. Near-real-time integration of surface pressure to obtain lift and pitching moment will be available to assess AFC effectiveness. The flow field will be measured using high-resolution particle image velocimetry (PIV) for off-body visualization.

The wind tunnel model spans the 5-foot test section and can be stationary or oscillating in pitch. The airfoil is a 15-inch chord VR-7 section similar to previous VGARD tests to provide tieback to flow control experiments with zero-mass jets. The model is modular with a detachable leading edge, which would allow for alternate AFC configurations or devices to be tested.

Computational fluid dynamics offers insight into the mechanics of flow control. High-fidelity solutions based on the Navier-Stokes equations will capture the jet interaction with the surrounding flow field and give an idea of promising chordwise locations for the sweeping-jet actuators. In addition, the CFD model will be used as a guide in the development of the experimental test matrix.

Details of SJA technology, experimental program, model hardware, data acquisition, and CFD calculations are provided in the following sections.

Wind Tunnel Modifications

The Texas A&M University Low-Speed Wind Tunnel (LSWT) is one of just several large, low-speed wind tunnels at U.S. universities. It was originally constructed in the late 1940s as an open-return tunnel (Figure 1) with a 7'× 10' (68 ft^2) test section capable of 200 mph, Mach 0.26 operation. The fan is a variable-pitch B-29 propeller driven by a 900-RPM 1250-hp motor. A decade later, work began to close the circuit and yielded the present configuration of the tunnel (Figure 2). The closed-circuit design offers many advantages to open design. However, the current tunnel retains the fan directly downstream of the test section, an undesirable feature of its original open layout.

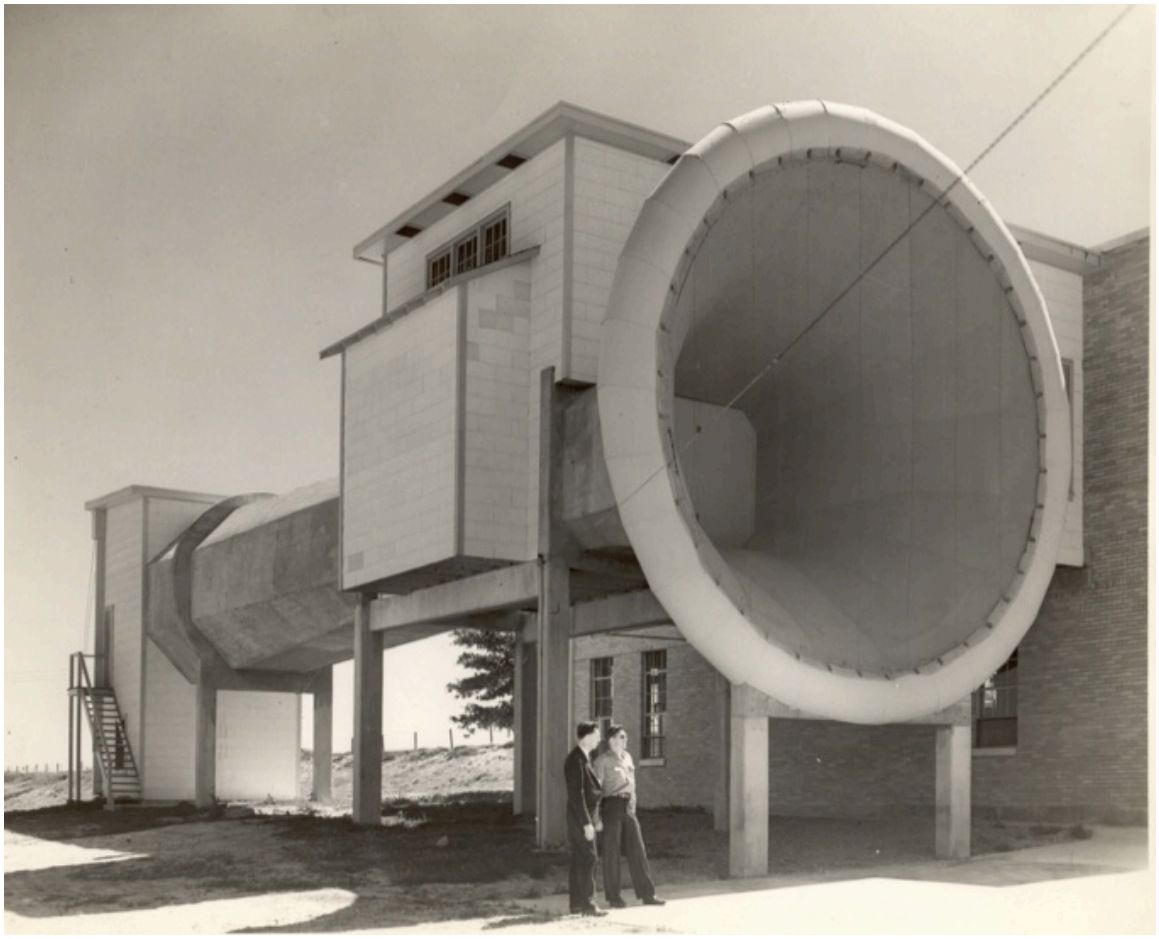

Figure 1: TAMU LSWT circa 1948.

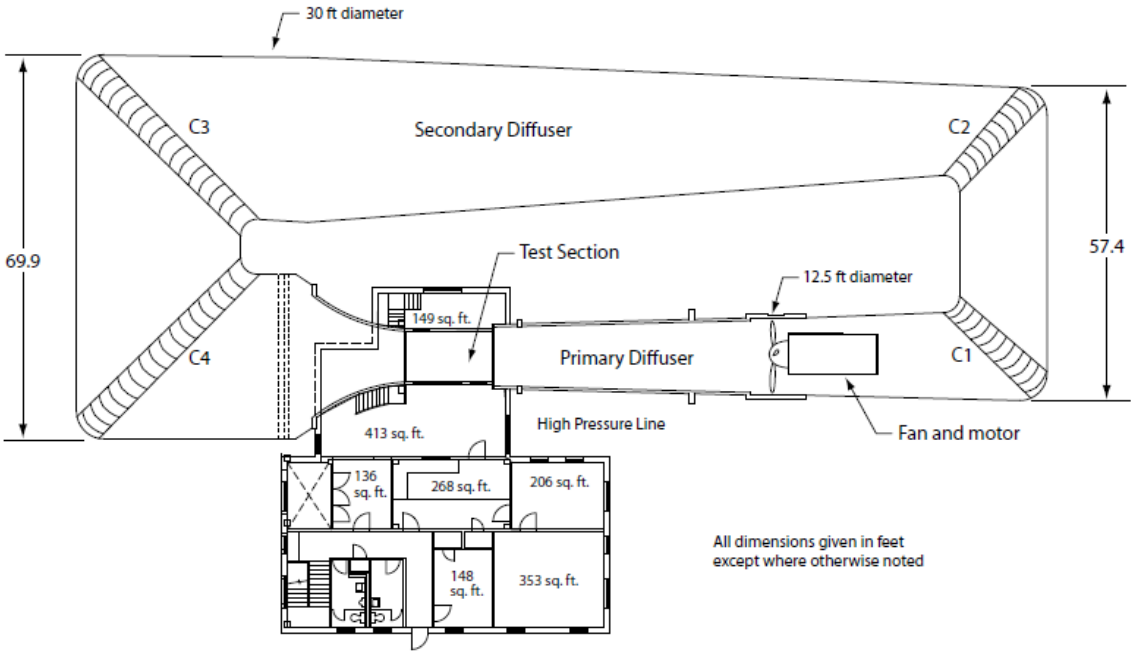

Figure 2: Current layout of the TAMU LSWT.

In the 2000's, research led by co-PI Prof. Rodney Bowersox and funded by the Army Research Office made measurements of dynamic stall on a characteristic helicopter blade airfoil in the LSWT. That work used PIV to image the leading edge and examined the vortex rollup under dynamic stall conditions. No load or surface pressure measurements were made. A feedback-controlled hydraulic actuator provided pitch rates up to 10 Hz on 12-inch-chord blades.

To accommodate the pitch mechanism for those tests, test-section inserts were constructed that reduced the test-section size to 7' × 7'. Besides providing 18 inches at each sidewall for the pitch system, reducing the test section size from 68 ft^2 to 49 ft^2 enabled the tunnel to exceed Mach 0.3. In addition to the test section liners, short contraction liners were installed to provide a smooth interface between the as-built contraction and the reduced-size test section. No change was made to the diffuser so both side-walls of the test section ended with an 18-inch-tall backward facing step at the beginning of the diffuser.

Building on the work using the 7' × 7'test section, liners were constructed to provide a 5-foot-tall × 7-foot-wide, 35 ft^2 test section. That size is sufficiently small that Mach 0.4 would be possible with the 1250 hp motor. Additional contraction liners plus short diffuser liners were constructed. However, the system proved incapable of reaching Mach 0.4. The most likely culprit was separation in the diffuser resulting from inadequately long liners whose equivalent cone angle exceeded guidelines for avoiding wind-tunnel diffuser separation.

Prior to the start of this project, the original 1930s-era 1250 hp motor was replaced with a new variable-speed 3000 hp motor capable of up to 1200 RPM. The project began with the premise that the LSWT would be marginally capable of providing Mach 0.5 flow using the existing 5' ×7' test-section liners and the new motor, provided that new diffuser liners were designed to meet design guidelines. The power required to drive a tunnel scales as the mass flow times the

velocity squared or, equivalently, the test-section area dynamic pressure to the 3/2 power. Data from the as-built 7’ × 10’ test section plus Bowersox’s work with the 7’ × 7’ test section was used to generate Figure 3 that projects a net 11% efficiency improvement is needed to achieve Mach 0.5 in the 5’ × 7’ test section using 3000 hp. This requires the design of an efficient diffuser, as well as finding additional efficiencies elsewhere in the system. If additional losses could not be corrected, a further-reduced test section size could be used to achieve the Mach-number target.

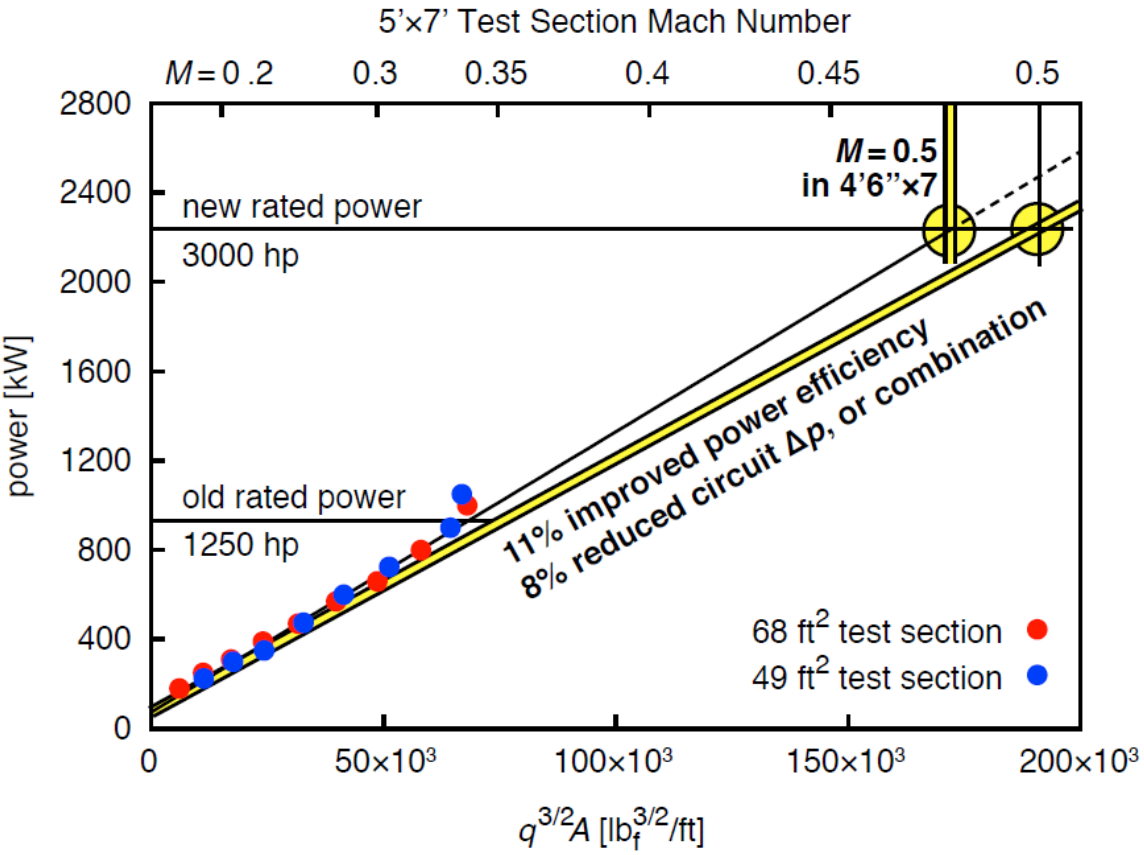

Figure 3: Power scaling for various test-section sizes.

After the project began, design estimates for the new wind-tunnel model showed that the intended 7-foot span would exceed material strength limits and that only a 5-foot span could meet design constraints. This increases the number of LSWT design modifications because it requires new test-section inserts and contraction liners in addition to the improved diffuser. However, by moving to a 6-foot-tall × 5-foot-wide test section, the area is further reduced to 30 ft^2 while the blockage (ratio between chord and tunnel height in a 2D configuration) is reduced. The reduced cross section lowers the anticipated power requirement at Mach 0.5 to 2857 hp, a 5% power margin (Figure 4).

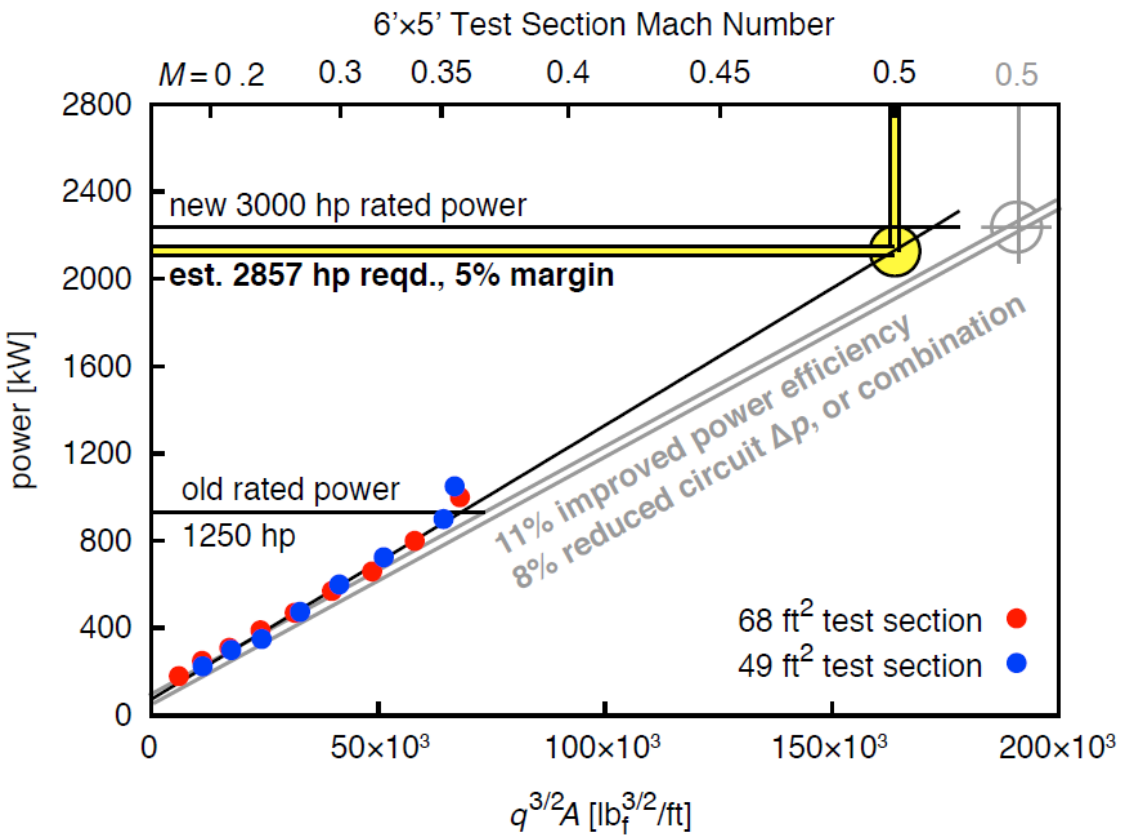

Figure 4: Power scaling for various test-section sizes with Mach numbers reflecting a 6×5 test section.

The 5% power margin is the projection based on performance of the old 1250 hp motor. While a precise improvement value is unknown, the new motor undoubtedly has better power efficiency than the old motor. Even a 5% improvement in motor power efficiency would double the anticipated power margin for Mach 0.5. This suggests that almost any non-separated diffuser design and no new efficiency improvements could be all that is required to achieve the Mach-number target. Nevertheless, efficiency improvements are explored and described.

Diffuser Design

The most critical aspect of the tunnel modifications is the diffuser insert design. As noted above, the fan is located directly downstream of the test section, 46.5 feet behind the test-section exit plane. The challenge is to expand the cross sectional area from 30 ft^2 to 123 ft^2 (12.5-foot diameter) over that short length while avoiding diffuser separation. The recommendation for doing so is to maintain equivalent diffuser cone angles at less than 3°. Given the length constraint, doing this is only possible using splitter plates in some or all of the diffuser. Splitter plates divide the flow into parallel channels of reduced expansion angle but do so at the expense of increased wall friction.

The eventual design choice for the diffuser is a 20-foot-long 1-duct section followed by a 26.5-foot-long 4-duct section with two splitter plates. The first section expands the 6' × 5' rectangular cross section to a 7.5-foot-diameter 12-sided polygon. The second section

maintains the shape and expands to a 12.5-foot diameter polygon. Figure 5 shows how the streamwise location of the transition and the diameter at that point affect diffuser power loss at Mach 0.5. Note the selected design is not the minimum-power point. The design instead minimizes the expansion angle and separation risk in both sections of the diffuser. The angles are 2.6° and 2.5° for the first and second sections, respectively. This reduced separation risk comes with marginally increased power requirements due to increased wall friction losses.

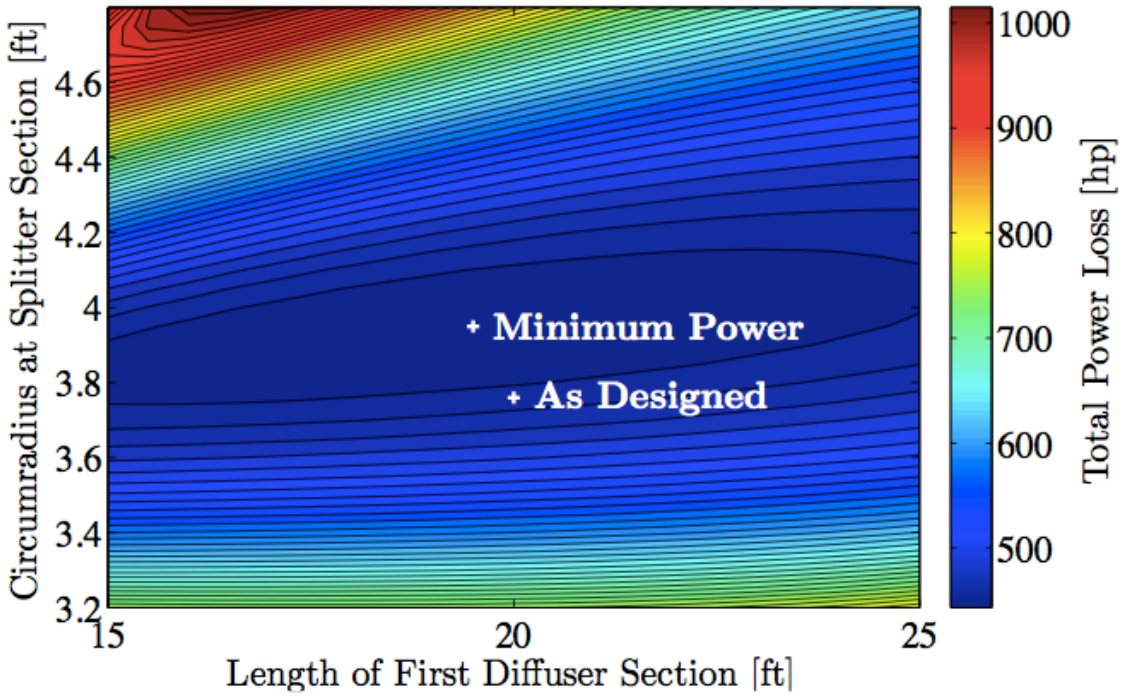

Figure 5: Mach 0.5 Diffuser power loss design estimates.

The mechanical design of the diffuser liners must provide the desired geometry while utilizing parts that can be hand-carried into the diffuser, adjusting for as-built variations in the existing diffuser and sustaining a 350 psf pressure difference, the approximate dynamic pressure at Mach 0.5. The final design consists of eleven 4-foot-spaced frames consisting of 2 inch × 2 inch structural steel tubing (0.25-inch-thick wall) with adjustable feet that push out against concrete structure. These frames fit in place and then anchor to the concrete with masonry screws through anchor points. The diffuser shape is provided by 1/16” sheet steel that is to be precut to the diffuser design and attached in place. That thickness passes finite-element analysis factor-of-safety checks at 350 psf. Implementing this design will be labor-intensive but not complicated. The frame and splitter plates are shown in Figure 6 while a cutaway of the sheet steel (blue) compared to the existing structure (gray) is shown in Figure 7.

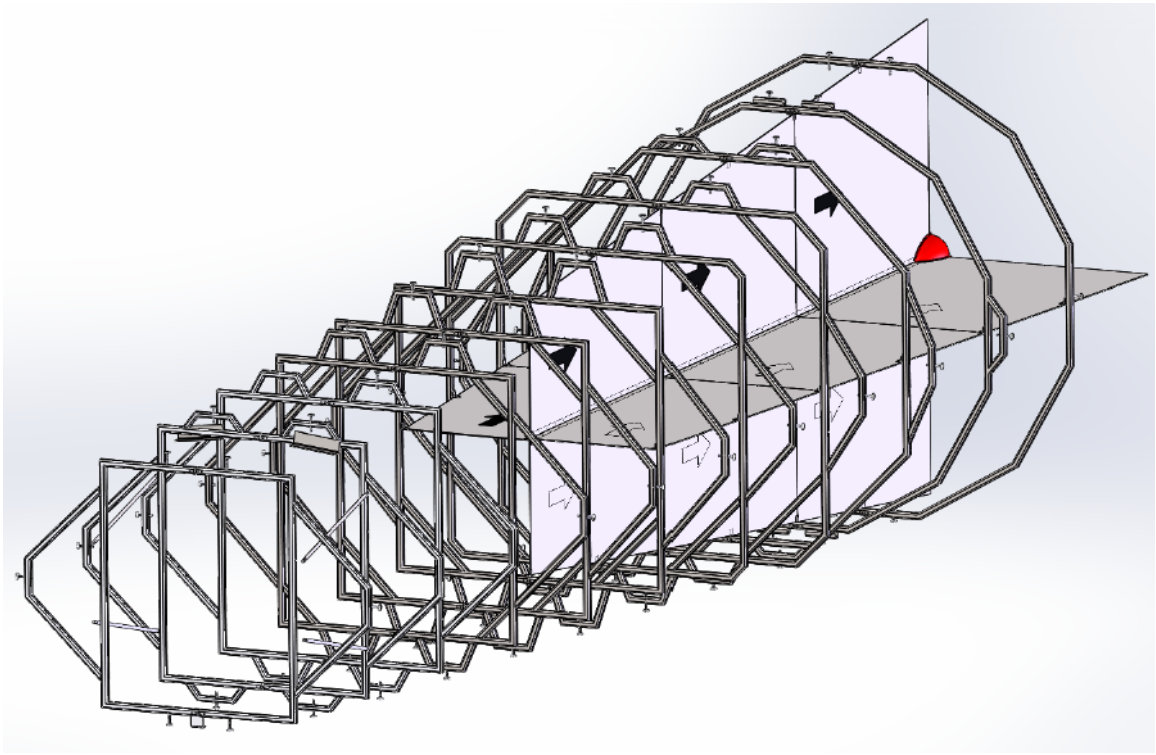

Figure 6: Diffuser-insert frames and splitter plates.

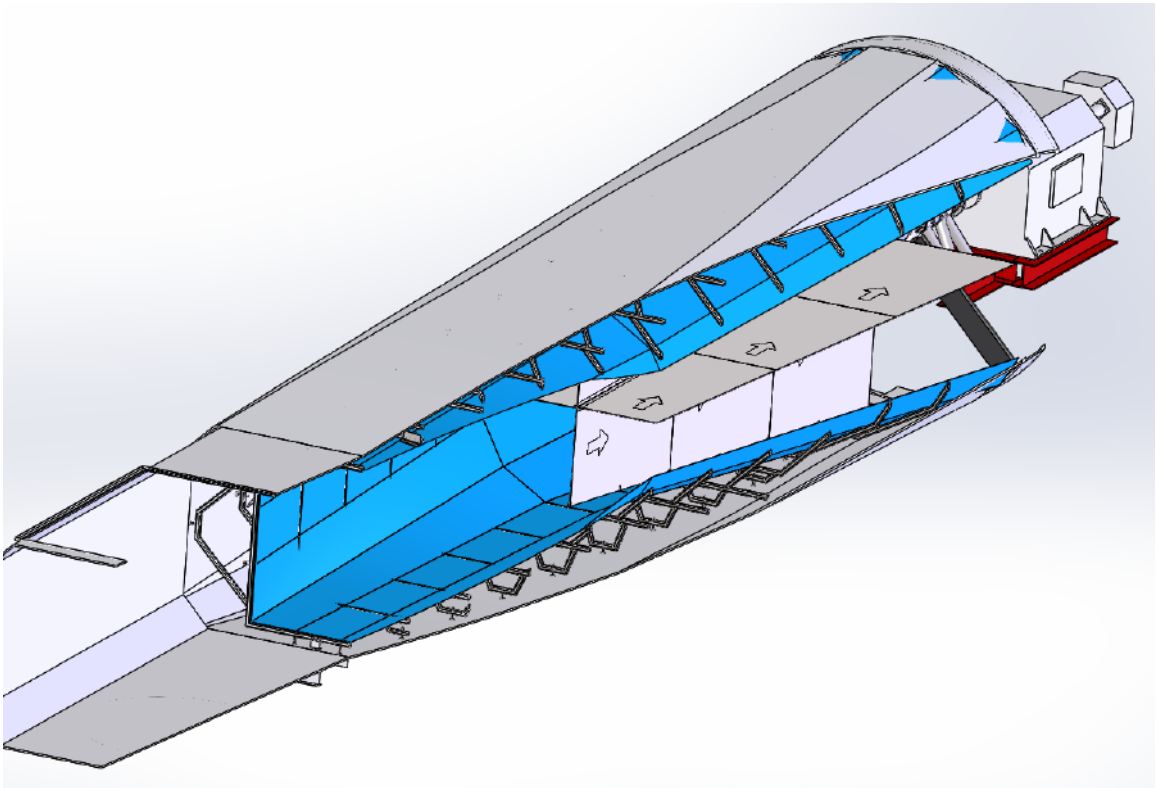

Figure 7: Diffuser sheet metal design.

Contraction Design

The contraction provides a strong favorable pressure gradient so its design details are not as critical to achieving Mach 0.5 as the diffuser details. Nevertheless, changing from a 7' ×10' test section to a 6' × 5' test section increases the risk of contraction separation because the contraction ratio increases from 10.4 to 20.2. Guidelines for contraction design recommend a contraction length 1.25 times the inlet diameter and 5th-degree polynomial shape with the steepest gradient at the midpoint of the contraction length. The current length is only 0.85 times the inlet diameter. Its shape is (apparently) circular arcs tangent at the midpoint. This design is more prone to separation than the polynomial shape.

The optimum diffuser design would apply the polynomial shape from the second screen to the test section inlet plane. The test section inlet plane can be moved 2 feet downstream to lengthen the contraction. Because the start of the contraction is a circular arc and the test section wall inserts are inset from the as-built walls, the optimum polynomial shape would not interfere with the as-built contraction. The challenge of this design is that thin liners would be required over the steepest part of the existing contraction. These would require a substantial number of anchors through the existing concrete. This would require much labor at heights up to 30 feet above ground inside and outside. The risk, time and expense of this approach are deemed too great to pursue.

An alternative contraction design was selected that leaves the first half of the contraction as is and modifies only the part downstream of the existing maximum slope-point. The plan is to start the wall liners at the (approximate) maximum slope point and end 2 feet into the existing test section. Sheet metal (1/16-inch thick as in the diffuser) will be bent to approximately match a 5th-degree polynomial shape with the 6 boundary conditions set by the (x,z) coordinates plus slope, z', and second derivative, $z'' = 0$, at the maximum-slope point in the contraction plus the coordinates (x,z), slope, $z' = 0$, and second derivative, $z'' = 0$, of the test-section inlet. Primary structural support will be provided by 4 inch × 4 inch structural steel tubing cantilevered from the test section with 2 inch × 2 inch steel extending to support the bent sheet steel. The last portion of sheet steel where it meets the maximum-slope point will be anchored to the as-built concrete but no other modifications are necessary to the existing contraction and all the needed work can occur inside without scaffolding. This increases safety and substantially reduces labor cost of installation. A local company in College Station, Exosent, Inc., has been identified that can cut and bend sheet steel to the appropriate dimensions using CNC equipment. Exosent can also assist with the welding required to fabricate the contraction framework in place.

Efficiency Improvements

Together, the reduced test-section area and improved motor efficiency are believed to be sufficient to provide Mach 0.5 flow. Therefore, tunnel efficiency improvements are not believed to be required. Nevertheless, improved efficiency would reduce operating costs and could improve flow quality at all velocities. Furthermore, improvements in power margin could be beneficial at any speed and were aggressively pursued. First, a large number of leaks around the tunnel were located and sealed. The tunnel vents to atmosphere at the test-section exit plane but the test section operates several psf below atmospheric pressure. All other points around the tunnel are at a higher-than-ambient static pressure. This higher pressure drives air

out through leaks. To conserve mass, equivalent air must be drawn into the test section and pass through the fan. This leads to increased power draw by the fan because more mass flow passes through the fan than passes through the test section. Sealing approximately 1 ft^2 of leaks (a reasonable estimate for the work completed, especially at hatches) and assuming a fan efficiency of 75% would save approximately 25 hp at 100 psf operation (Mach 0.26) and 160 hp at 350 psf (Mach 0.5). At Mach 0.5, that represents about 5% of the power estimated from the projection in Figure 4.

The second efficiency improvement approach was attempting to identify and correct separated flow downstream of the fan. At the outset of the project, separation seemed most likely from the downstream end of the motor housing and from the wooden inserts on the tunnel walls between the fan and corner 2. Yarn tufts were installed on these surfaces and video recordings were made at test-section dynamic pressures up to 50 psf (Mach 0.18). These images showed that the suspect areas maintain reasonably well attached flow. However, the corner 1 and corner 2 turning vanes, which were also tufted, showed violently-separated flow at the leading edge. The vanes are saw-cut 0.25-inch-thick steel bent into a 90° bend with an extended, straight trailing edge. They are spaced 2.5 feet apart. The likely reason for the separation is the absence of a rounding leading edge and non-aligned flow at the start of the corner.

Separated flow on the corner-1 and corner-2 vanes represents a substantial power loss because the area is still relative small (18-foot diameter) so the local dynamic pressure is high. A loss coefficient for a well-designed 90° bend with turning vanes is k = 0.15. At a test-section dynamic pressure of 100 psf, the local dynamic pressure is approximately 7.2 psf. At k = 15%, this translates to a 40 hp power loss for each set of vanes. Given the separation observed, the actual loss is likely to be at least double this value.

To determine the potential efficiency improvement that could be achieved using turning vane reconditioning, three proof-of-concept vane covers and rib sets were fabricated and installed. Before-and-after vane wake surveys were made to measure the loss coefficient with and without the vane covers. The cross section of the modified vanes is shown in Figure 8. The pressure side is the existing vane while the suction side is the same as the SA-070.61 vane developed by Sahlin and Johansson [7]. The suction side was fabricated as 3-foot-tall sections of bent galvanized steel sheet metal. The ribs are lumber cut using a CNC router. Individual components are shown in Figure 9.

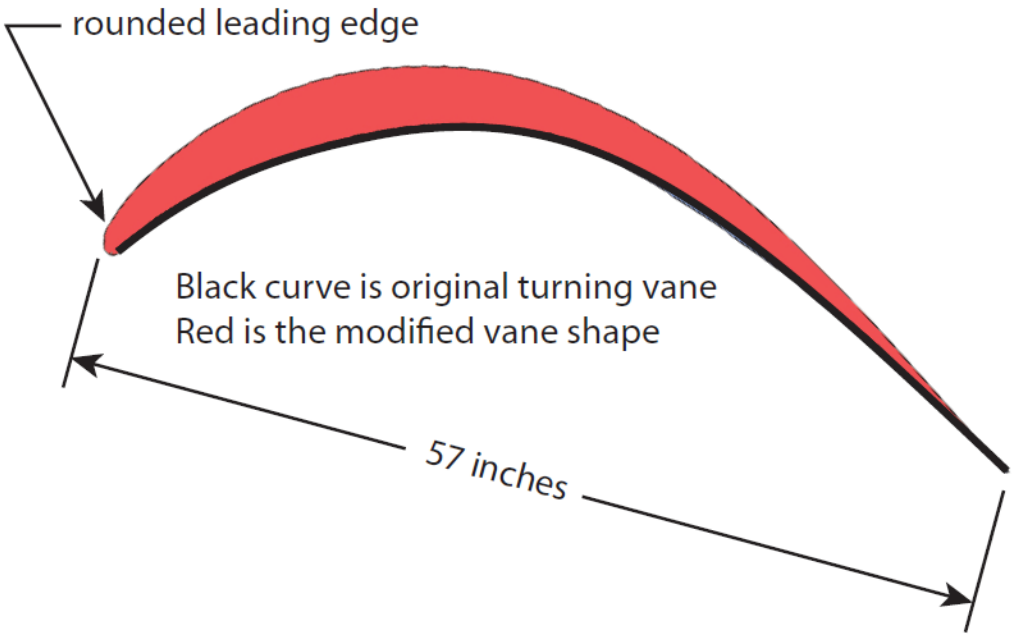

Figure 8: Turning vane airfoil shape modification.

Figure 9: Turning vane airfoil shape modification.

Upstream and downstream velocity profiles were measured using a pitot tube mounted to an automated 1D traverse. The traverse was oriented such that it moved parallel to the vane cascade with the pitot tube oriented at a 45° angle, directly into the oncoming flow. The traverse is shown upstream of modified blades in Figure 10. Upstream and downstream static pressures are essentially uniform across the flow. The dynamic pressure upstream is similarly uniform while the downstream dynamic pressure shows a characteristic wake profile (Figure 11). Subtracting the integral of the total pressure (static plus dynamic pressure) measured across one cascade spacing downstream of the cascade from a similar integral upstream gives the vane loss. Prior to modification, the loss is measured to be 4.5% of the test-section dynamic pressure or k = 63% using the local dynamic pressure. After modification that loss is reduced to 1.0% of the test-section dynamic pressure (k = 14%), almost exactly the expected value for a correctly-designed vane.

Figure 10: Modified turning vanes and pitot traverse.

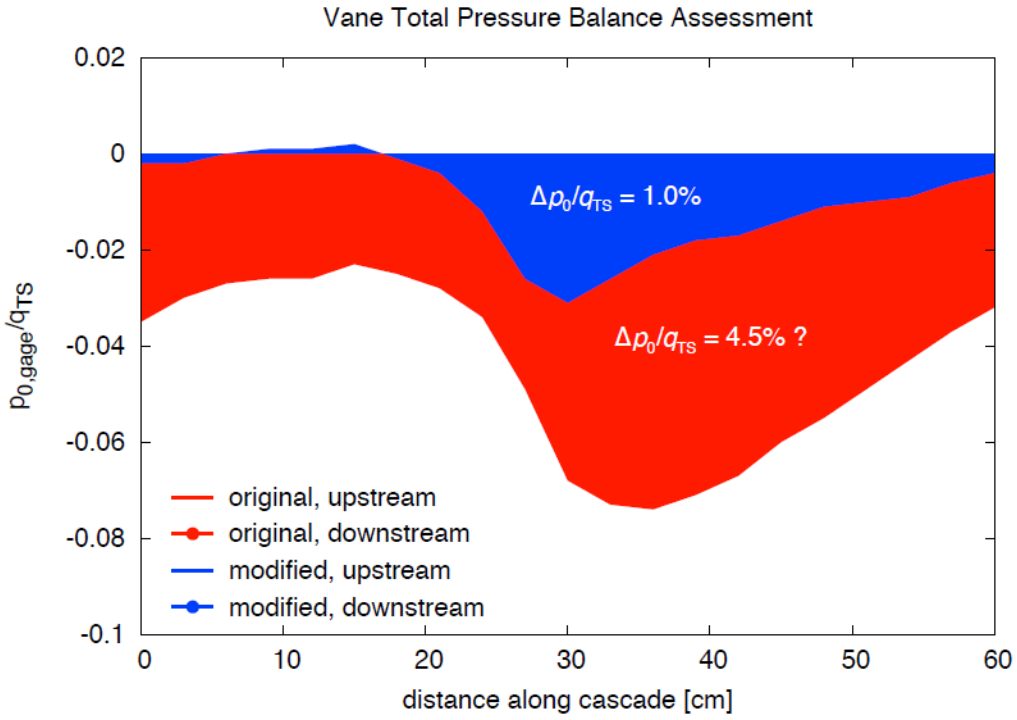

Figure 11: Total pressure losses across an as-built and modified corner-2 turning vane.

The actual potential improvement in vane performance is not as dramatic as Figure 11 would indicate. The corresponding dynamic pressure plot (not shown) for the as-built vane, fails to satisfy mass-conservation requirements. This suggests that the blockage of the traverse is sufficient to divert flow from the cascade passage of interest and corrupt the measurement. This artificially increases the measured loss given in Figure 11. Mass conservation is satisfied in the modified-vane measurement so k = 14%. Regardless of the precise as-built loss coefficient, the modified vanes are a dramatic improvement as they provide attached flow. Besides meeting mass-conservation requirements, tuft tests of the modified vanes showed that the flow remains attached on the suction side of the vanes (Figure 12).

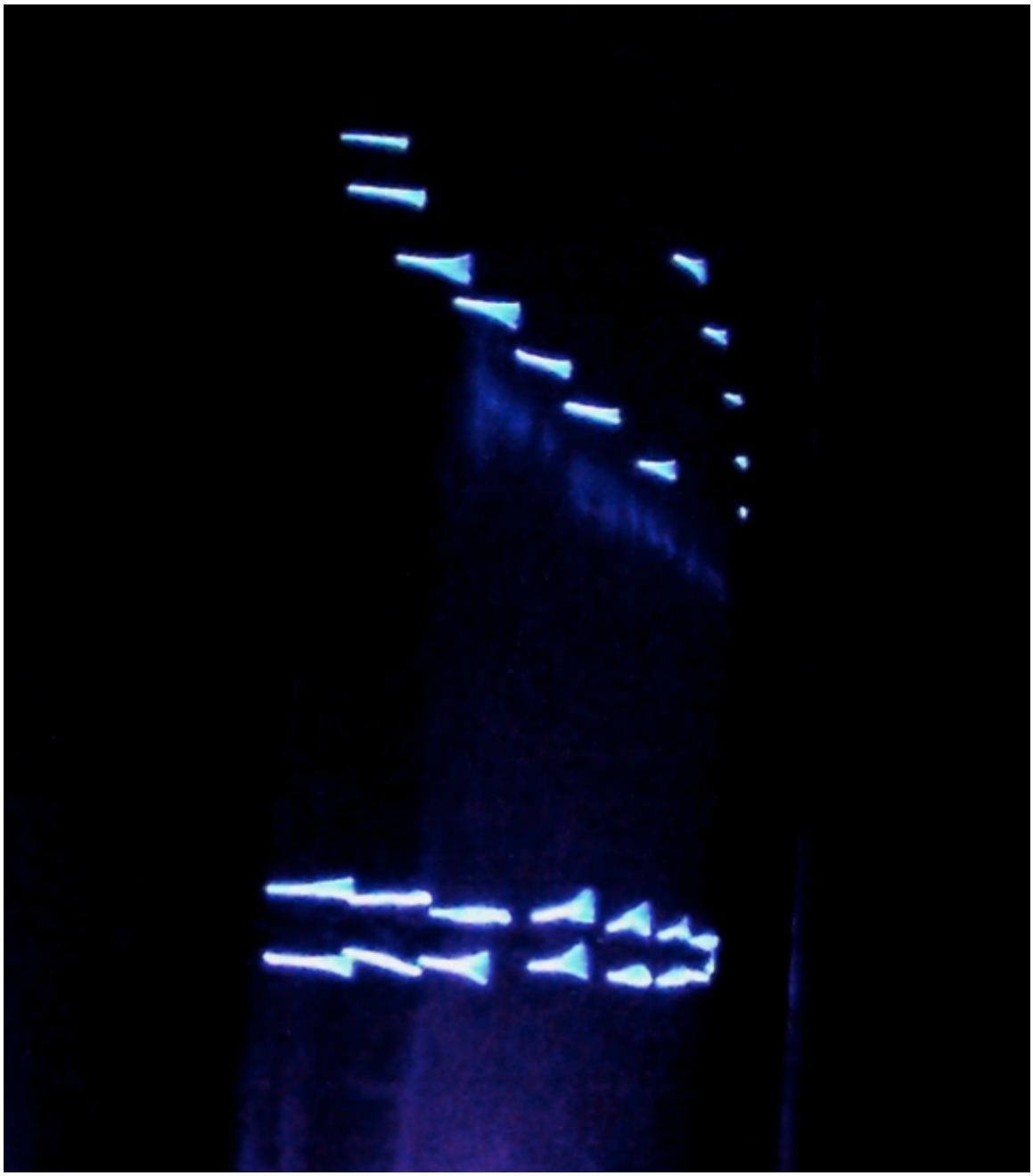

Figure 12: Vane suction-side tuft flow visualization. Flow is from left to right. The tufts indicate attached flow.

A whole-tunnel circuit efficiency measurement was made by measuring total pressures at various stations around the entire tunnel circuit. These are presented in Figure 13 as total pressure coefficients, $Cp_0 = (p_0 - p_{0,TS})/q_{TS}$, using the test section total pressure and dynamic pressure as reference quantities. Measurements between q_{TS} = 50 and 100 psf collapse to the curve shown. For comparison, a design estimate for the LSWT is also given. Pressure losses were estimated using NASA TN D-8243 [8]. These measurements show the total pressure loss across corners 1 and 2 is about 65% larger than predicted using k = 15%. This value likely underestimates the present loss because the measurement just upstream of corner 1 is thought

to underestimate the total pressure there due to the turbulent flow downstream of the fan. Therefore, a current loss coefficient for the existing corner 1 and corner 2 turning vanes is between k = 25% (circuit total pressure measurements) and k = 63% with the actual value likely closer to the low end of the range.

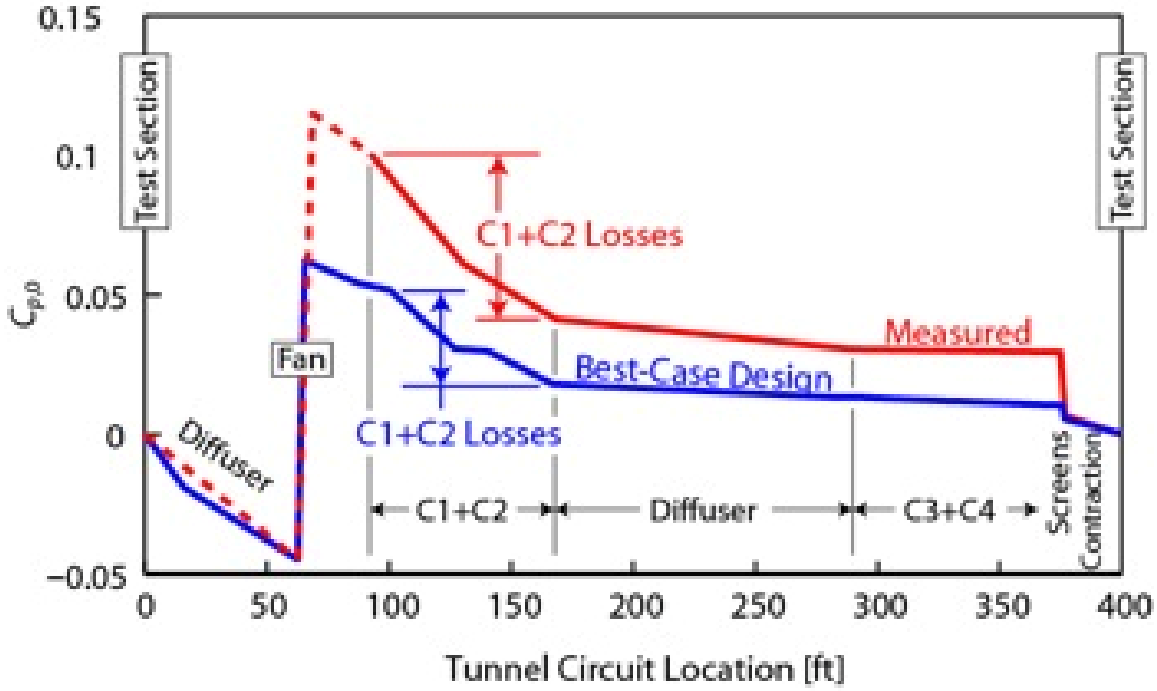

Figure 13: Whole-circuit loss for the 7×10 LSWT configuration.

The measurements suggest that the worst-performing parts of the LSWT system are the turbulence screens upstream of the contraction. Indeed, improving the screens would lead to substantially reduced total pressure loss around the circuit. The power loss associated with a pressure loss is proportional to the local velocity. Because the speeds at corners 1 and 2 are nearly triple that at the screens, improving the corners is a much higher priority. Moreover, a preliminary screen replacement cost is $300,000 while corners 1 and 2 could be reconditioned for less than $50,000.

Unfortunately, turbulent flow contaminated the total-pressure measurement upstream of the fan so the increase in total pressure across the fan is unknown. Using NASA TN D-8243 to estimate the upstream total pressure and disregarding any measurement error downstream suggests $\Delta p_0 \approx 0.15\ q_{TS}$. Corresponding motor power measurements indicate the combined motor and fan efficiency is between 65% and 75%. With a reduced-area test section, the mass flow across the fan will not exceed current values so similar efficiencies are expected for the target Mach numbers.

Our calculations show that Mach 0.5 flow can be achieved in a 6’ × 5’ test section in the TAMU LSWT using the new 3000 hp motor. Although the efficiency of the existing circuit is poor relative to modern design expectations, the motor is sufficiently powerful to overcome these

losses using a straightforward extrapolation to Mach 0.5. Without improvement, the reduced-area test section gives a 5% power margin. Every factor considered increases this margin. Most significantly, the extrapolation uses data from the old 1250 hp motor. Improved motor efficiency at least doubles the margin and potentially gives a much larger margin. Even sealing tunnel leaks is likely to have increased the margin from 5% to 10%.

Work on circuit efficiency improvements show that the tunnel losses at corners 1 and 2 could likely be halved for relatively modest cost using turning vane covers. Because the test section area will be reduced to achieve increased Mach numbers, the tunnel losses shift from being largely due to these corners to being largely due to wall friction in the test section and diffuser. In fact, with Mach 0.5 in a 6' × 5' test section, there is less mass flow through the system than there is presently at Mach 0.26. The breakdown of the estimated total power for the modified tunnel (without turning vane modifications), is presented in Table 1. In Table 1, Total power is the power dissipated by wind-tunnel losses, "Total with ηf" is the power required by the motor to deliver the power required by the flow, and efficiency, ηf, is the net motor and fan efficiency. This shows that the majority of the required power comes from the high-speed sections, namely the test section and two diffuser sections. Thus, modifications to the remaining portions of the system are valuable for normal operations but offer little for high-speed, reduced-area operation.

Table 1: Mach 0.5 power requirement estimates.

Number	Type	Mach	K [NA]	P [hp]	Circuit P %
1	Constant Area Duct	0.02	0.00	0.0	0.0
2	Contraction	0.02	0.02	0.3	0.0
3	Test Section	0.50	0.02	250.8	27.8
4a	Diffuser (1st Section)	0.50	0.02	209.7	23.3
4b	Diffuser (2nd Section)	0.33	0.06	307.1	34.1
5	Power Section (Contraction)	0.11	0.00	0.4	0.0
6	Power Section (Diffuser)	0.13	0.02	14.7	1.6
7	Diffuser	0.09	0.01	4.4	0.5
8	Corner 1	0.08	0.14	48.5	5.4
9	Diffuser	0.07	0.01	1.5	0.2
10	Corner 2	0.06	0.14	31.6	3.5
11	Diffuser	0.05	0.06	8.7	1.0
12	Contraction	0.02	0.00	0.0	0.0
13	Corner 3	0.02	0.15	2.5	0.3
14	Constant Area Duct	0.02	0.00	0.0	0.0
15	Corner 4	0.02	0.15	2.5	0.3
16	Constant Area Duct	0.02	0.00	0.0	0.0
17	Screen	0.02	0.57	9.3	1.0
18	Screen	0.02	0.57	9.3	1.0
	Total			901.3	
	Total with η_f = 75%			1,201.7	
	Total with η_f = 50%			1,802.6	

These results initially seem at odds with the projections in Figure 13, 2857 hp versus 1803 hp for the same conditions. The differences reflect both the unknown, but certainly favorable, increase in efficiency of the new motor. Figure 13 was generated using old-motor data while the estimate of 65% to 75% net efficiency was made for the new motor. Furthermore, the $Aq^{3/2}$ scaling used in Figure 13 does not account for the observation that, as the test section area decreases, the losses through the unmodified portion of the tunnel quickly decrease in importance relative to those of the high-speed section. When the test section is reduced to 30 ft^2, the test section and diffuser represent 85% of the total power loss. For the 68 ft2 tunnel, those same sections contribute only 43% of the loss while corners 1 and 2 are 30% of the power loss and the screens are 13%. So, again, the estimate of a 5% power margin at Mach 0.5 is a highly conservative estimate. The actual margin may exceed 40%.

The Wind Tunnel Model

The wind tunnel model fits in the planned 6’ × 5’ test section of the TAMU wind tunnel, designed to achieve Mach 0.5 flow. The model spans the width of the test section to connect to the outside-mounted pitch-oscillating rig for frequencies up to 10 Hz. The model is of the VR-7 airfoil, with a 15-inch chord, and a 4% tab angled 3 degrees trailing-edge up from the chord line. This represents the airfoil used on today’s CH-47 Chinook helicopters.

Figure 14 presents the general features and arrangement of the airfoil model. The model is modular with a separable leading edge containing the AFC actuators. The spar is the primary structure and is made of steel. It is sized by the magnitude of alternating aerodynamic loads that are larger than the inertial loads from the dynamic motion. The spar holds ESP modules, air supply for the AFC actuators, and instrumentation wires. The trailing edge is of lightweight aluminum and contains instrumentation primarily for pressure measurements. Figure 15 shows images of the modules.

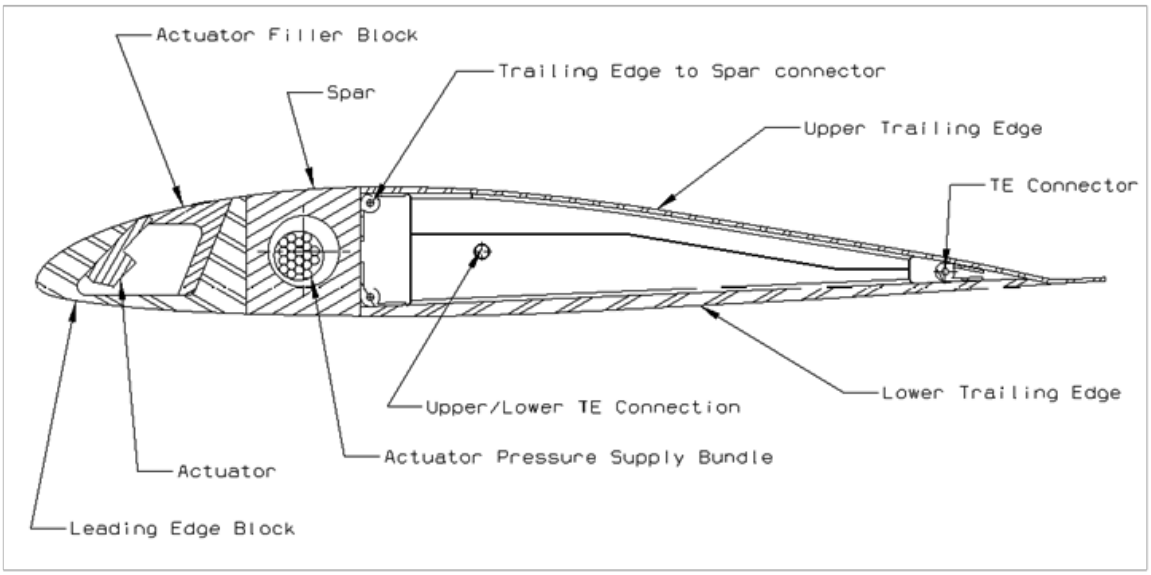

Figure 14: General features of the wind tunnel model.

The design allows for easy assembly. First, the AFC actuators are installed in the leading edge and held in place by screws. Movement of the actuators is further prevented by the filler block, which also serves to align the actuators and constrain the air hoses from moving. Second, the ESP modules are installed in the spar and pressure taps are connected to it. Next, the leading edge is connected to the spar and aligned with pins. The upper pin engages both the leading edge and the filler block. The leading edge is bolted to the spar from the aft surface. Finally, the trailing edge module is attached to the spar. The upper and lower trailing-edge surfaces are bolted together at the ribs and the assembly is connected to the spar with a piano hinge pin.

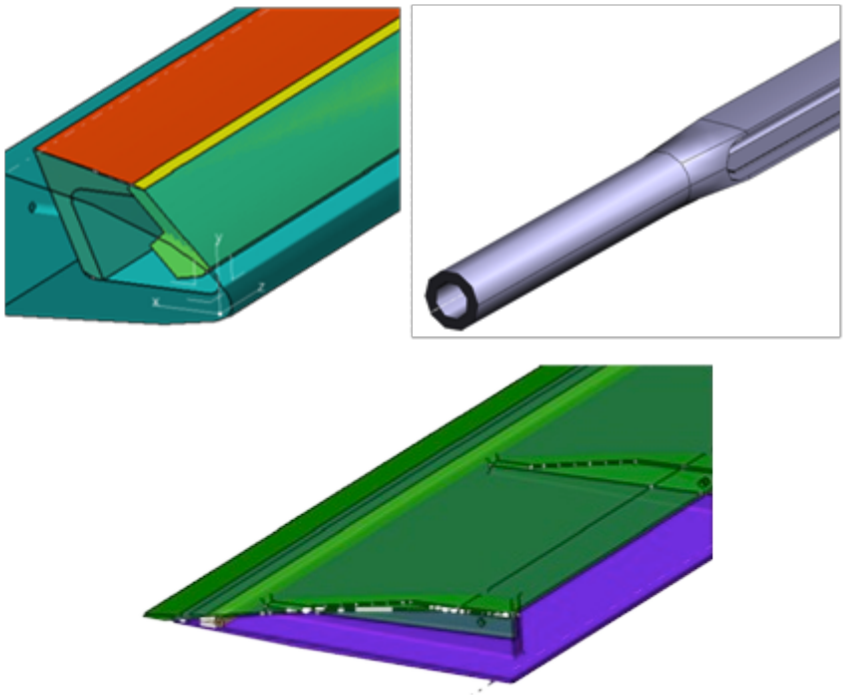

Figure 15: Modules of the wind tunnel model; leading edge (left), spar (middle), trailing edge (right)

Forty-five pressure tap locations were defined to maximize accuracy in integrated force and moment measurements. The positions are a result of an optimization algorithm that utilized 20 snapshots of the pressure distribution from a dynamic stall simulation. The locations are shown in Figure 16 and tabulated in Appendix C.

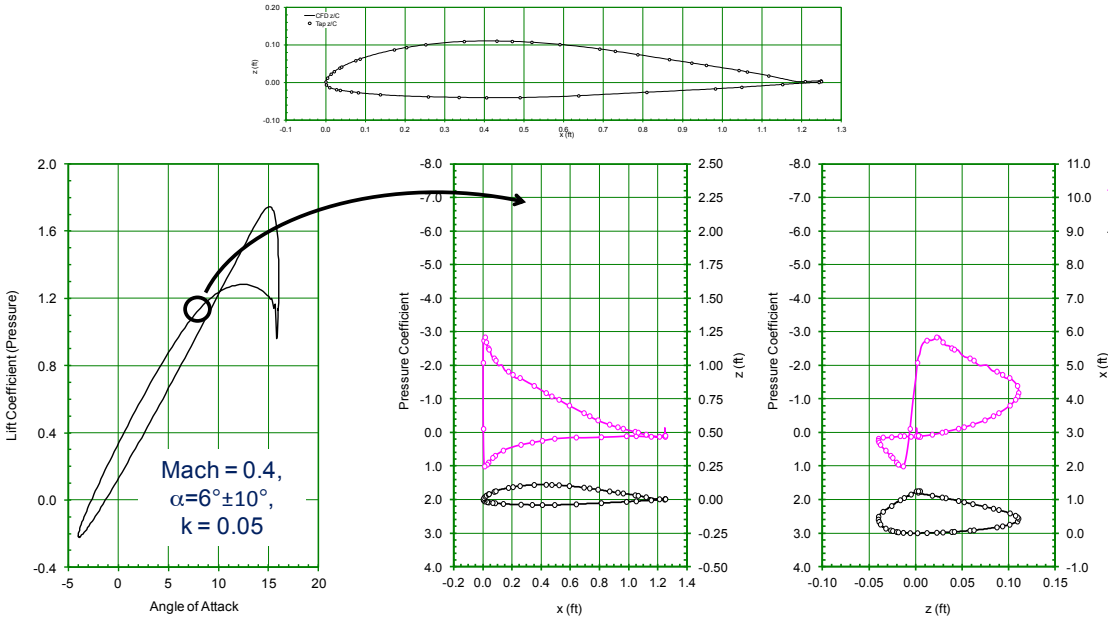

Figure 16: Results of an optimization to define 45 pressure-tap locations for accurate force and moment measurements during dynamic stall.

AFC Actuator Description

Control of flow separation on a dynamically oscillating airfoil at Mach 0.5 may require sweeping jets operating up to their maximum jet speed capability of Mach 1.0. Based on previous studies by Advanced Fluidics [9], the requirement to produce this speed and fit in the available small space inside the airfoil leading edge, sizes the actuators to 0.5 × 0.5 inches with jet exit dimensions of 1.0 mm high by 2.0 mm wide.

The actuators will be manufactured in five, 10.5-inch long, identical arrays each containing 20 jets. These arrays will be used to span the wing. One quarter of an inch is reserved on both ends of each array to fasten it securely to the wind tunnel model. A gap of 1 inch between arrays provides structural integrity of the wind tunnel model. Figure 17 shows this arrangement. The design provides the option to test actuators arrangements with two larger spacings of 1 inch and 1.5 inches by blocking every other actuator or every two actuators respectively. This is shown in Figure 18.

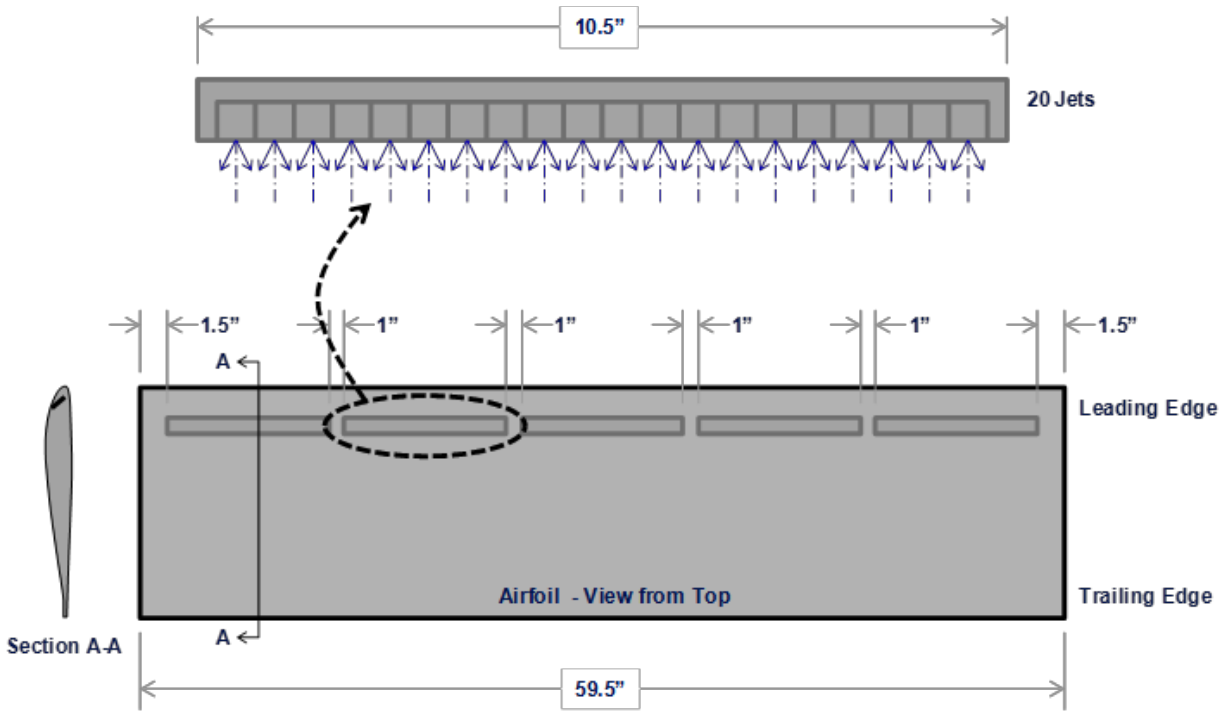

Figure 17: Notional arrangement of actuators in the array and arrays in the wind tunnel model.

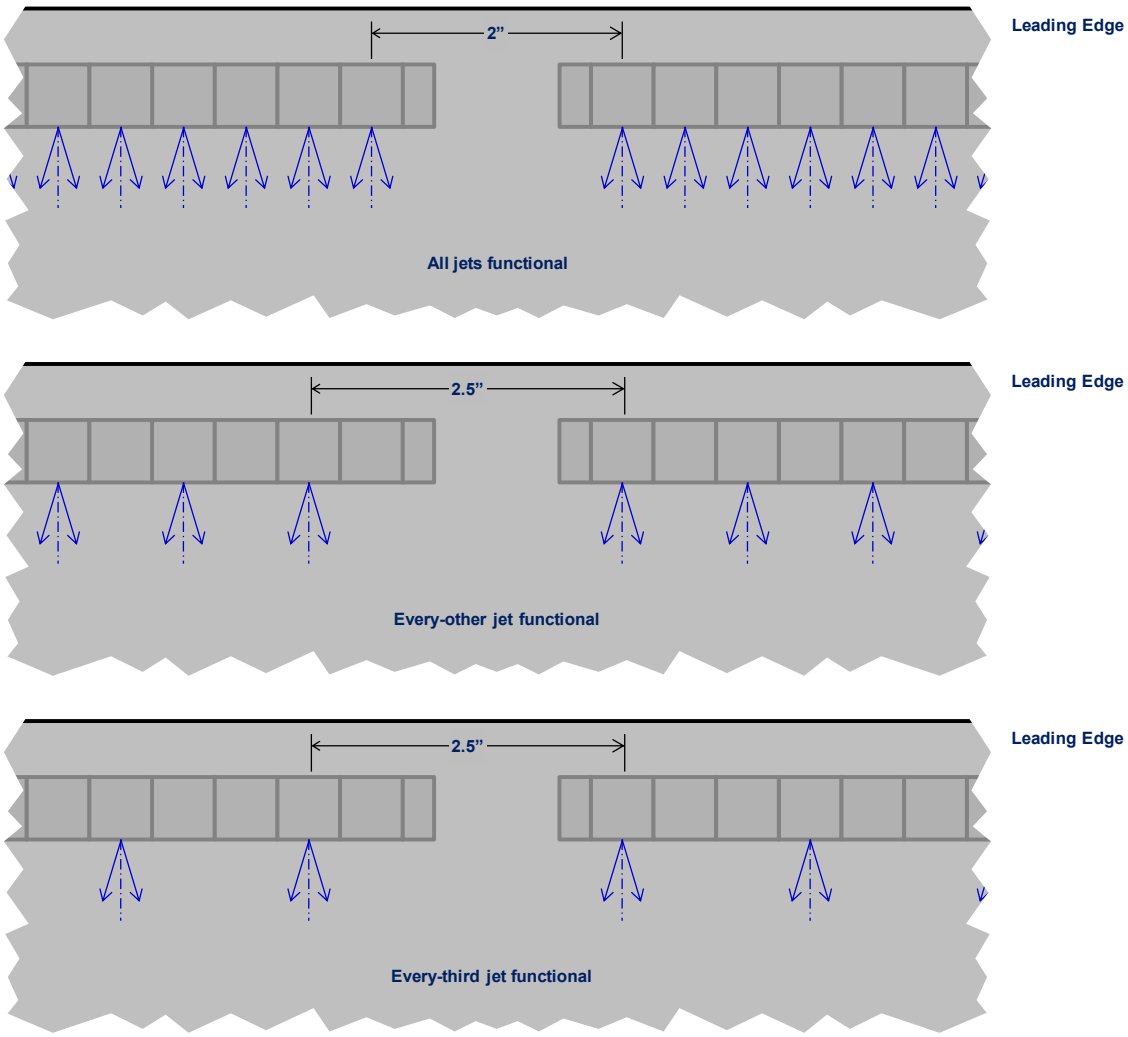

Figure 18: Variations in jet spacing using the same jet array.

The required mass flow into the arrays, assuming 100 jets and a sonic jet Mach number, is approximately 11 lbs/min. Air is supplied to the manifold that feeds the actuators through four 1/8” pipe fittings spaced throughout each length of the array. For continuous operation, the jets will be fed from shop air at about 30 psi.

The sweeping jet actuators install in the model according to the arrangement shown in Figure 19. The actuator will be bolted to the leading edge by a pair of ¼-20 screws on the actuator segments. The jet exits will be positioned at 8% of the chord, which is the nearest to the leading edge they can be due to geometric constraints. The angle that the emerging jets make with the local tangent of the airfoil surface is 30 degrees. The chordwise location of the actuators is a subject for further investigation. Larger chord airfoils will not be subject to the same geometric constraints as the current model and sweeping jet actuators may prove more effective if they are placed forward of shocks that develop in High Mach number flows.

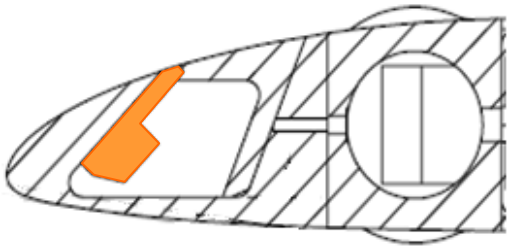

Figure 19: Arrangement of sweeping jet actuator (orange) installed in the wind tunnel model.

Each jet is designed to sweep through a total angle ranging from 30 to 100 degrees relative to the chord-line direction, with no tunnel flow. With tunnel flow, the sweep angles will be reduced due to the interaction with the free stream. The reduction depends on the wind-tunnel speed. The current intent is to obtain a sweep angle between 60 and 75 degrees. To provide this, the angle built into the jet exits is 120 degrees. This should work for Mach numbers from 0.2 to 0.5.

The design of the actuator array is shown in Figure 20 and Figure 21, and the manufactured prototype in Figure 22. The prototype was bench-top tested for basic functionality. Figure 23 shows the experimental arrangement for testing the array. A compressor supplied air to a manifold having four outlets. The outlets were then connected to the four ports in the array with 1/16" NPT-27 barbs having an inside diameter of 0.1". A microphone obtained the acoustic data from the sweeping jets. The microphone was placed about ¼" above the exit of the actuators as shown in the figure. The data from the microphone was processed to provide the spectra of the signals.

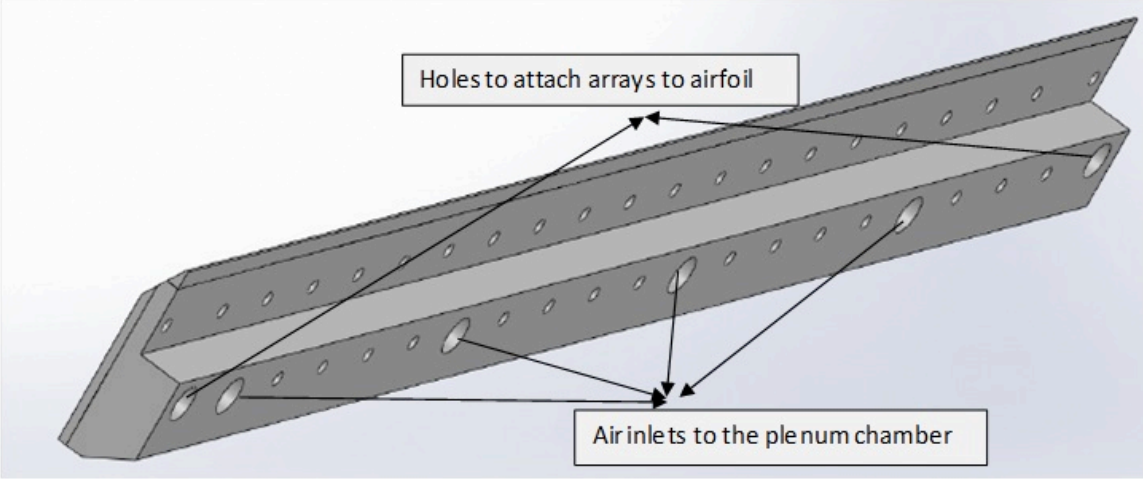

Figure 20: An actuator array showing the air inlets to the plenum and the holes to attach the array to the airfoil.

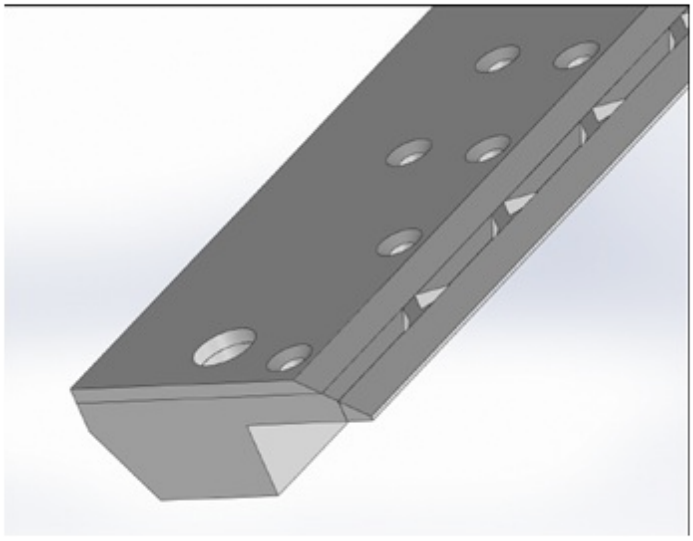

Figure 21: Top view of a section of the array

Typical spectra at 5 and 8 psi are shown in Figure 24 and Figure 25, respectively. Because of the limited air supply, only 3 jet exits were open, and the rest were taped closed. The sweep frequency of the jet is manifested in the acoustic signature with oscillations of approximately 1.9KHz with 5psi air supplied and 2.2 KHz with 8 psi.

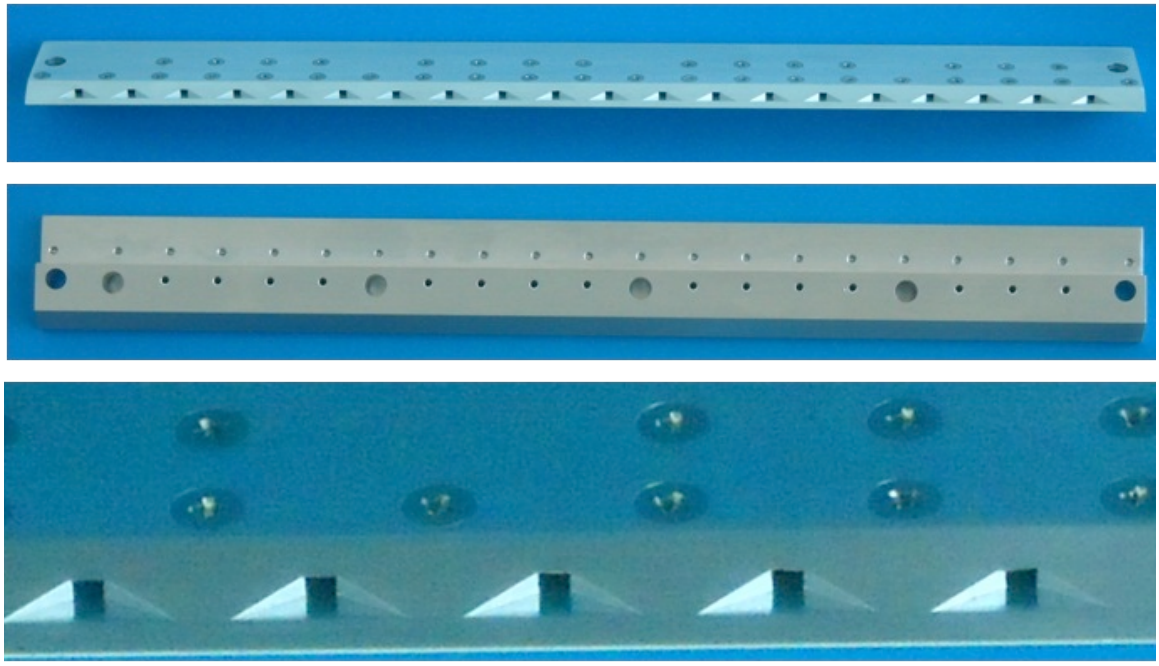

Figure 22: Actuator Array and a close-up view of the exit geometry.

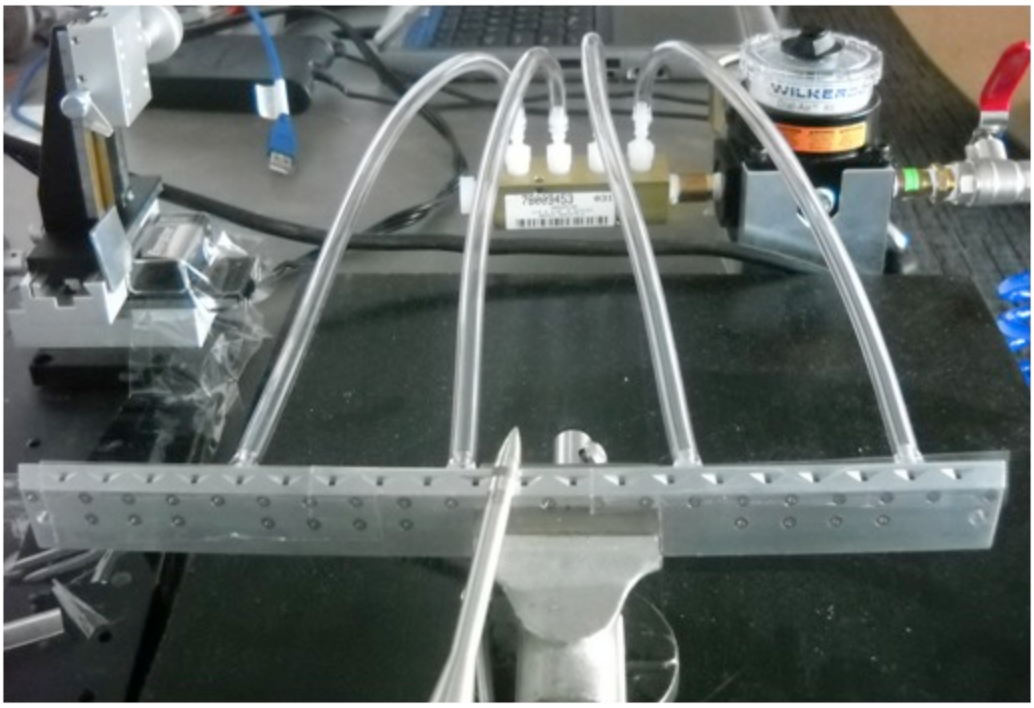

Figure 23: Experimental set up for preliminary testing of the array.

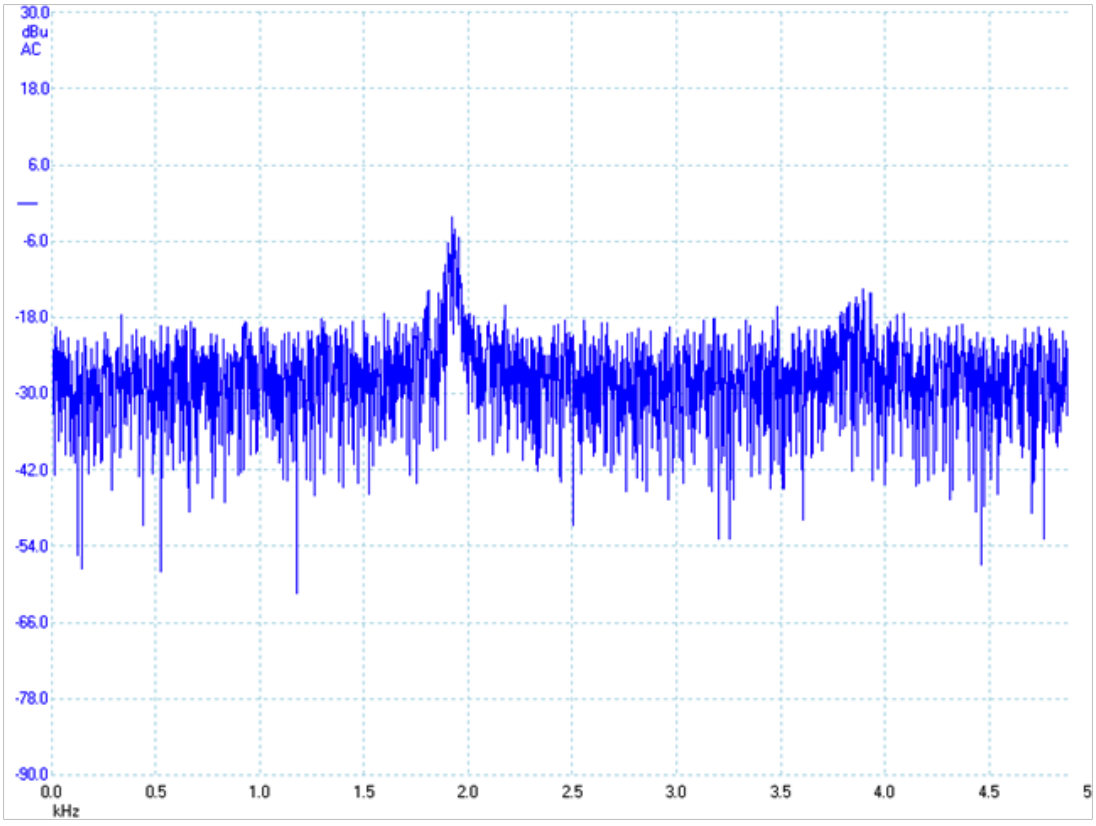

Figure 24: Spectra from microphone signals for supply pressure of 5 psi. Frequency ~ 1.9 kHz

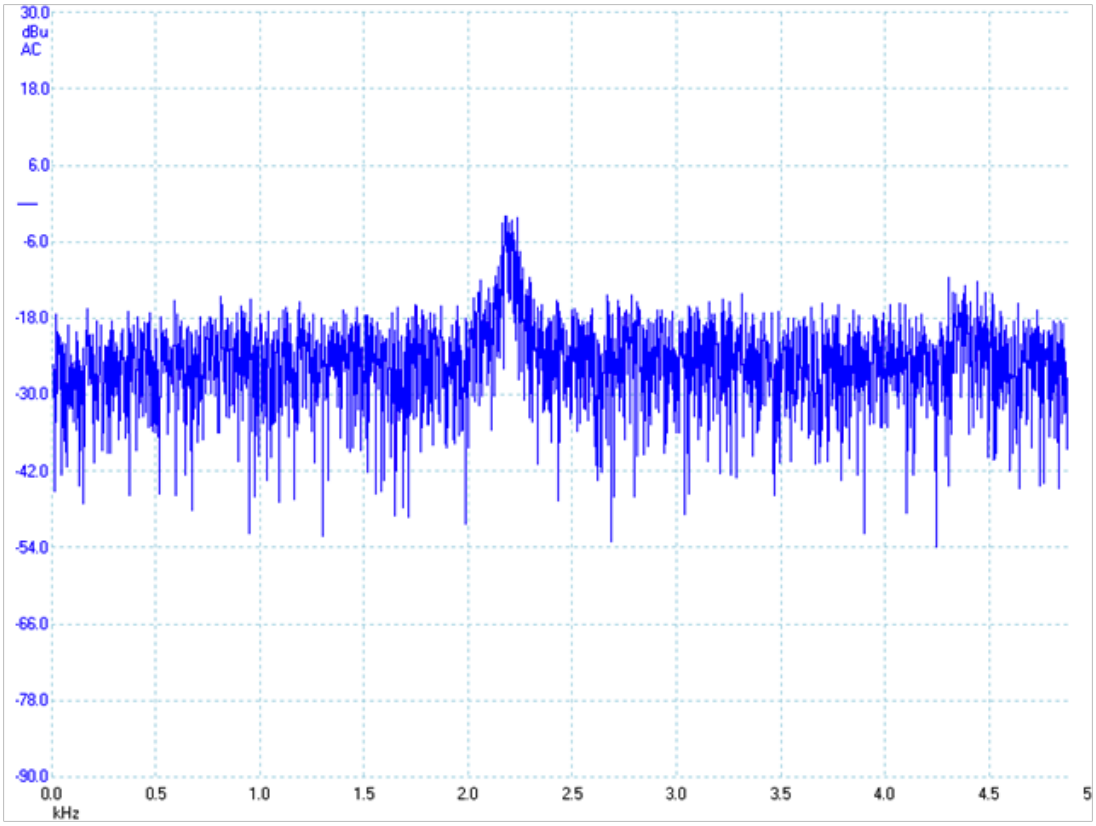

Figure 25: Spectra from microphone signals for supply pressure of 8 psi. Frequency ~ 2.2 KHz.

Notional Wind-Tunnel Test Matrix

The matrix of wind tunnel test runs is outlined in this section. It is comprised of a combination of baseline runs without AFC and runs with AFC. All test points will obtain surface pressure measurements, which will be integrated to obtain lift, drag, and pitching moments. Certain key evaluation points will be further investigated using PIV to quantify off-body flow features.

The test will begin with an evaluation of the flow quality in the empty tunnel. The new test section, contraction, and diffuser, warrant a mapping of flow quantities to document uniformity and flow angularity. This evaluation will be conducted across the Mach number range from 0.2 to 0.5. If the flow quality is satisfactory, the next step is to install the model, conduct runs (no pitching, no AFC) without boundary layer trips then install the boundary layer trips and rerun. The boundary layer trips will be installed ahead of the 8% chord point. Surface flow visualization will be conducted to ensure that the tripping is effective.

Quasi-steady, and dynamic key conditions will be measured for both the baseline and several active flow control configurations. The conditions will span the Mach number range and focus on pitch frequencies and angle-of-attack ranges for which there is modest separation on the upper surface. The spacing between sweeping-jet actuators will be varied as follows: all jets open, every-other jet open, and every third jet open. Shop air will regulate the actuators' jet frequency. At the conclusion of this group of tests, we will select an AFC configuration for further testing. Measurements of the baseline and the selected AFC configuration flow field will be obtained using PIV.

The baseline and AFC configuration evaluation will be expanded in the next two run groups. Here the effect of additional mean pitch angles, amplitudes, and reduced frequencies will be tested. The conditions, covering the range of Mach numbers from 0.2 to 0.5, will be characterized by light, medium, and deep stall.

The final section of the run matrix is reserved for additional PIV measurements. Preliminary conditions have been selected, however these will likely be replaced when actual data is obtained.

Considering the time required by test section installation, model installation, testing, and removal of equipment at the end of the test to return the wind tunnel to its original configuration, the test matrix shown is aggressive and is not likely to fit within the allotted time. When the test time nears, a conference will be held to reduce the test conditions to a manageable number.

Run No.	Mach	Angle of Attack		Frequency		Press.	PIV
		Mean	Amp.	Red.	Hz		
Flow Quality Survey							
1	0.5	NA	NA	NA	NA		
2	0.4	NA	NA	NA	NA		
3	0.3	NA	NA	NA	NA		
4	0.2	NA	NA	NA	NA		
No AFC							
5	0.5	6	10	0.100	7.1	✓	
2	0.4	6	10	0.100	5.7	✓	
3	0.3	6	10	0.050	2.1	✓	
4	0.2	6	10	0.010	0.3	✓	
Baseline AFC: All jets open							
5	0.5	6	10	0.100	7.1	✓	
6	0.4	6	10	0.100	5.7	✓	
7	0.3	6	10	0.050	2.1	✓	
8	0.2	6	10	0.010	0.3	✓	
Revision 1 AFC: Every-other jet closed							
9	0.5	6	10	0.100	7.1	✓	
10	0.4	6	10	0.100	5.7	✓	
11	0.3	6	10	0.050	2.1	✓	
12	0.2	6	10	0.010	0.3	✓	
Revision 2 AFC: Every two jet closed							
13	0.5	6	10	0.100	7.1	✓	
14	0.4	6	10	0.100	5.7	✓	
15	0.3	6	10	0.050	2.1	✓	
16	0.2	6	10	0.010	0.3	✓	

Run No.	Mach	Angle of Attack		Frequency		Press.	PIV
		Mean	Amp.	Red.	Hz		
AFC Configuration Down Selection							
No AFC							
17	0.5	6	10	0.100	7.1	✓	✓
18	0.4	6	10	0.100	5.7	✓	✓
19	0.3	6	10	0.050	2.1	✓	✓
20	0.2	6	10	0.010	0.3	✓	✓
AFC with Selected Configuration							
21	0.5	6	10	0.100	7.1	✓	✓
22	0.4	6	10	0.100	5.7	✓	✓
23	0.3	6	10	0.050	2.1	✓	✓
24	0.2	6	10	0.010	0.3	✓	✓
No AFC							
25	0.5	9	5	0.005	0.4	✓	
26	0.5	9	5	0.020	1.4	✓	
27	0.5	9	5	0.050	3.6	✓	
28	0.5	9	5	0.100	7.1	✓	
29	0.5	9	5	0.120	8.5	✓	
30	0.5	10	5	0.005	0.4	✓	
31	0.5	10	5	0.020	1.4	✓	
32	0.5	10	5	0.050	3.6	✓	
33	0.5	10	5	0.100	7.1	✓	
34	0.5	10	5	0.120	8.5	✓	
35	0.5	11	5	0.005	0.4	✓	
36	0.5	11	5	0.020	1.4	✓	
37	0.5	11	5	0.050	3.6	✓	
38	0.5	11	5	0.100	7.1	✓	
39	0.5	11	5	0.120	8.5	✓	

Run No.	Mach	Angle of Attack		Frequency		Press.	PIV
		Mean	Amp.	Red.	Hz		
40	0.5	6	10	0.005	0.4	✓	
41	0.5	6	10	0.020	1.4	✓	
42	0.5	6	10	0.050	3.6	✓	
43	0.5	6	10	0.100	7.1	✓	
44	0.5	6	10	0.120	8.5	✓	
45	0.5	7	10	0.005	0.4	✓	
46	0.5	7	10	0.020	1.4	✓	
47	0.5	7	10	0.050	3.6	✓	
48	0.5	7	10	0.100	7.1	✓	
49	0.5	7	10	0.120	8.5	✓	
50	0.5	8	10	0.005	0.4	✓	
51	0.5	8	10	0.020	1.4	✓	
52	0.5	8	10	0.050	3.6	✓	
53	0.5	8	10	0.100	7.1	✓	
54	0.5	8	10	0.120	8.5	✓	
55	0.5	9	10	0.005	0.4	✓	
56	0.5	9	10	0.020	1.4	✓	
57	0.5	9	10	0.050	3.6	✓	
58	0.5	9	10	0.100	7.1	✓	
59	0.5	9	10	0.120	8.5	✓	
60	0.4	9	5	0.005	0.3	✓	
61	0.4	9	5	0.020	1.1	✓	
62	0.4	9	5	0.050	2.8	✓	
63	0.4	9	5	0.100	5.7	✓	
64	0.4	9	5	0.120	6.8	✓	
65	0.4	10	5	0.005	0.3	✓	

Run No.	Mach	Angle of Attack		Frequency		Press.	PIV
		Mean	Amp.	Red.	Hz		
66	0.4	10	5	0.020	1.1	✓	
67	0.4	10	5	0.050	2.8	✓	
68	0.4	10	5	0.100	5.7	✓	
69	0.4	10	5	0.120	6.8	✓	
70	0.4	11	5	0.005	0.3	✓	
71	0.4	11	5	0.020	1.1	✓	
72	0.4	11	5	0.050	2.8	✓	
73	0.4	11	5	0.100	5.7	✓	
74	0.4	11	5	0.120	6.8	✓	
75	0.4	6	10	0.005	0.3	✓	
76	0.4	6	10	0.020	1.1	✓	
77	0.4	6	10	0.050	2.8	✓	
78	0.4	6	10	0.100	5.7	✓	
79	0.4	6	10	0.120	6.8	✓	
80	0.4	7	10	0.005	0.3	✓	
81	0.4	7	10	0.020	1.1	✓	
82	0.4	7	10	0.050	2.8	✓	
83	0.4	7	10	0.100	5.7	✓	
84	0.4	7	10	0.120	6.8	✓	
85	0.4	8	10	0.005	0.3	✓	
86	0.4	8	10	0.020	1.1	✓	
87	0.4	8	10	0.050	2.8	✓	
88	0.4	8	10	0.100	5.7	✓	
89	0.4	8	10	0.120	6.8	✓	
90	0.4	9	10	0.005	0.3	✓	
91	0.4	9	10	0.020	1.1	✓	
92	0.4	9	10	0.050	2.8	✓	

Run No.	Mach	Angle of Attack		Frequency		Press.	PIV
		Mean	Amp.	Red.	Hz		
93	0.4	9	10	0.100	5.7	✓	
94	0.4	9	10	0.120	6.8	✓	
95	0.3	9	5	0.005	0.2	✓	
96	0.3	9	5	0.020	0.9	✓	
97	0.3	9	5	0.050	2.1	✓	
98	0.3	9	5	0.100	4.3	✓	
99	0.3	9	5	0.120	5.1	✓	
100	0.3	10	5	0.005	0.2	✓	
101	0.3	10	5	0.020	0.9	✓	
102	0.3	10	5	0.050	2.1	✓	
103	0.3	10	5	0.100	4.3	✓	
104	0.3	10	5	0.120	5.1	✓	
105	0.3	11	5	0.005	0.2	✓	
106	0.3	11	5	0.020	0.9	✓	
107	0.3	11	5	0.050	2.1	✓	
108	0.3	11	5	0.100	4.3	✓	
109	0.3	11	5	0.120	5.1	✓	
110	0.3	6	10	0.005	0.2	✓	
111	0.3	6	10	0.020	0.9	✓	
112	0.3	6	10	0.050	2.1	✓	
113	0.3	6	10	0.100	4.3	✓	
114	0.3	6	10	0.120	5.1	✓	
115	0.3	7	10	0.005	0.2	✓	
116	0.3	7	10	0.020	0.9	✓	
117	0.3	7	10	0.050	2.1	✓	
118	0.3	7	10	0.100	4.3	✓	
119	0.3	7	10	0.120	5.1	✓	

Run No.	Mach	Angle of Attack		Frequency		Press.	PIV
		Mean	Amp.	Red.	Hz		
120	0.3	8	10	0.005	0.2	✓	
121	0.3	8	10	0.020	0.9	✓	
122	0.3	8	10	0.050	2.1	✓	
123	0.3	8	10	0.100	4.3	✓	
124	0.3	8	10	0.120	5.1	✓	
125	0.3	9	10	0.005	0.2	✓	
126	0.3	9	10	0.020	0.9	✓	
127	0.3	9	10	0.050	2.1	✓	
128	0.3	9	10	0.100	4.3	✓	
129	0.3	9	10	0.120	5.1	✓	
130	0.2	9	5	0.005	0.1	✓	
131	0.2	9	5	0.020	0.6	✓	
132	0.2	9	5	0.050	1.4	✓	
133	0.2	9	5	0.100	2.8	✓	
134	0.2	9	5	0.120	3.4	✓	
135	0.2	10	5	0.005	0.1	✓	
136	0.2	10	5	0.020	0.6	✓	
137	0.2	10	5	0.050	1.4	✓	
138	0.2	10	5	0.100	2.8	✓	
139	0.2	10	5	0.120	3.4	✓	
140	0.2	11	5	0.005	0.1	✓	
141	0.2	11	5	0.020	0.6	✓	
142	0.2	11	5	0.050	1.4	✓	
143	0.2	11	5	0.100	2.8	✓	
144	0.2	11	5	0.120	3.4	✓	
145	0.2	6	10	0.005	0.1	✓	
146	0.2	6	10	0.020	0.6	✓	

Run No.	Mach	Angle of Attack		Frequency		Press.	PIV
		Mean	Amp.	Red.	Hz		
147	0.2	6	10	0.050	1.4	✓	
148	0.2	6	10	0.100	2.8	✓	
149	0.2	6	10	0.120	3.4	✓	
150	0.2	7	10	0.005	0.1	✓	
151	0.2	7	10	0.020	0.6	✓	
152	0.2	7	10	0.050	1.4	✓	
153	0.2	7	10	0.100	2.8	✓	
154	0.2	7	10	0.120	3.4	✓	
155	0.2	8	10	0.005	0.1	✓	
156	0.2	8	10	0.020	0.6	✓	
157	0.2	8	10	0.050	1.4	✓	
158	0.2	8	10	0.100	2.8	✓	
159	0.2	8	10	0.120	3.4	✓	
160	0.2	9	10	0.005	0.1	✓	
161	0.2	9	10	0.020	0.6	✓	
162	0.2	9	10	0.050	1.4	✓	
163	0.2	9	10	0.100	2.8	✓	
164	0.2	9	10	0.120	3.4	✓	
AFC with Downselected Configuration							
165	0.5	9	5	0.005	0.4	✓	
166	0.5	9	5	0.020	1.4	✓	
167	0.5	9	5	0.050	3.6	✓	
168	0.5	9	5	0.100	7.1	✓	
169	0.5	9	5	0.120	8.5	✓	
170	0.5	10	5	0.005	0.4	✓	
171	0.5	10	5	0.020	1.4	✓	
172	0.5	10	5	0.050	3.6	✓	

Run No.	Mach	Angle of Attack		Frequency		Press.	PIV
		Mean	Amp.	Red.	Hz		
173	0.5	10	5	0.100	7.1	✓	
174	0.5	10	5	0.120	8.5	✓	
175	0.5	11	5	0.005	0.4	✓	
176	0.5	11	5	0.020	1.4	✓	
177	0.5	11	5	0.050	3.6	✓	
178	0.5	11	5	0.100	7.1	✓	
179	0.5	11	5	0.120	8.5	✓	
180	0.5	6	10	0.005	0.4	✓	
181	0.5	6	10	0.020	1.4	✓	
182	0.5	6	10	0.050	3.6	✓	
183	0.5	6	10	0.100	7.1	✓	
184	0.5	6	10	0.120	8.5	✓	
185	0.5	7	10	0.005	0.4	✓	
186	0.5	7	10	0.020	1.4	✓	
187	0.5	7	10	0.050	3.6	✓	
188	0.5	7	10	0.100	7.1	✓	
189	0.5	7	10	0.120	8.5	✓	
190	0.5	8	10	0.005	0.4	✓	
191	0.5	8	10	0.020	1.4	✓	
192	0.5	8	10	0.050	3.6	✓	
193	0.5	8	10	0.100	7.1	✓	
194	0.5	8	10	0.120	8.5	✓	
195	0.5	9	10	0.005	0.4	✓	
196	0.5	9	10	0.020	1.4	✓	
197	0.5	9	10	0.050	3.6	✓	
198	0.5	9	10	0.100	7.1	✓	
199	0.5	9	10	0.120	8.5	✓	

Run No.	Mach	Angle of Attack		Frequency		Press.	PIV
		Mean	Amp.	Red.	Hz		
200	0.4	9	5	0.005	0.3	✓	
201	0.4	9	5	0.020	1.1	✓	
202	0.4	9	5	0.050	2.8	✓	
203	0.4	9	5	0.100	5.7	✓	
204	0.4	9	5	0.120	6.8	✓	
205	0.4	10	5	0.005	0.3	✓	
206	0.4	10	5	0.020	1.1	✓	
207	0.4	10	5	0.050	2.8	✓	
208	0.4	10	5	0.100	5.7	✓	
209	0.4	10	5	0.120	6.8	✓	
210	0.4	11	5	0.005	0.3	✓	
211	0.4	11	5	0.020	1.1	✓	
212	0.4	11	5	0.050	2.8	✓	
213	0.4	11	5	0.100	5.7	✓	
214	0.4	11	5	0.120	6.8	✓	
215	0.4	6	10	0.005	0.3	✓	
216	0.4	6	10	0.020	1.1	✓	
217	0.4	6	10	0.050	2.8	✓	
218	0.4	6	10	0.100	5.7	✓	
219	0.4	6	10	0.120	6.8	✓	
220	0.4	7	10	0.005	0.3	✓	
221	0.4	7	10	0.020	1.1	✓	
222	0.4	7	10	0.050	2.8	✓	
223	0.4	7	10	0.100	5.7	✓	
224	0.4	7	10	0.120	6.8	✓	
225	0.4	8	10	0.005	0.3	✓	
226	0.4	8	10	0.020	1.1	✓	

Run No.	Mach	Angle of Attack		Frequency		Press.	PIV
		Mean	Amp.	Red.	Hz		
227	0.4	8	10	0.050	2.8	✓	
228	0.4	8	10	0.100	5.7	✓	
229	0.4	8	10	0.120	6.8	✓	
230	0.4	9	10	0.005	0.3	✓	
231	0.4	9	10	0.020	1.1	✓	
232	0.4	9	10	0.050	2.8	✓	
233	0.4	9	10	0.100	5.7	✓	
234	0.4	9	10	0.120	6.8	✓	
235	0.3	9	5	0.005	0.2	✓	
236	0.3	9	5	0.020	0.9	✓	
237	0.3	9	5	0.050	2.1	✓	
238	0.3	9	5	0.100	4.3	✓	
239	0.3	9	5	0.120	5.1	✓	
240	0.3	10	5	0.005	0.2	✓	
241	0.3	10	5	0.020	0.9	✓	
242	0.3	10	5	0.050	2.1	✓	
243	0.3	10	5	0.100	4.3	✓	
244	0.3	10	5	0.120	5.1	✓	
245	0.3	11	5	0.005	0.2	✓	
246	0.3	11	5	0.020	0.9	✓	
247	0.3	11	5	0.050	2.1	✓	
248	0.3	11	5	0.100	4.3	✓	
249	0.3	11	5	0.120	5.1	✓	
250	0.3	6	10	0.005	0.2	✓	
251	0.3	6	10	0.020	0.9	✓	
252	0.3	6	10	0.050	2.1	✓	
253	0.3	6	10	0.100	4.3	✓	

Run No.	Mach	Angle of Attack		Frequency		Press.	PIV
		Mean	Amp.	Red.	Hz		
254	0.3	6	10	0.120	5.1	✓	
255	0.3	7	10	0.005	0.2	✓	
256	0.3	7	10	0.020	0.9	✓	
257	0.3	7	10	0.050	2.1	✓	
258	0.3	7	10	0.100	4.3	✓	
259	0.3	7	10	0.120	5.1	✓	
260	0.3	8	10	0.005	0.2	✓	
261	0.3	8	10	0.020	0.9	✓	
262	0.3	8	10	0.050	2.1	✓	
263	0.3	8	10	0.100	4.3	✓	
264	0.3	8	10	0.120	5.1	✓	
265	0.3	9	10	0.005	0.2	✓	
266	0.3	9	10	0.020	0.9	✓	
267	0.3	9	10	0.050	2.1	✓	
268	0.3	9	10	0.100	4.3	✓	
269	0.3	9	10	0.120	5.1	✓	
270	0.2	9	5	0.005	0.1	✓	
271	0.2	9	5	0.020	0.6	✓	
272	0.2	9	5	0.050	1.4	✓	
273	0.2	9	5	0.100	2.8	✓	
274	0.2	9	5	0.120	3.4	✓	
275	0.2	10	5	0.005	0.1	✓	
276	0.2	10	5	0.020	0.6	✓	
277	0.2	10	5	0.050	1.4	✓	
278	0.2	10	5	0.100	2.8	✓	
279	0.2	10	5	0.120	3.4	✓	
280	0.2	11	5	0.005	0.1	✓	

Run No.	Mach	Angle of Attack		Frequency		Press.	PIV
		Mean	Amp.	Red.	Hz		
281	0.2	11	5	0.020	0.6	✓	
282	0.2	11	5	0.050	1.4	✓	
283	0.2	11	5	0.100	2.8	✓	
284	0.2	11	5	0.120	3.4	✓	
285	0.2	6	10	0.005	0.1	✓	
286	0.2	6	10	0.020	0.6	✓	
287	0.2	6	10	0.050	1.4	✓	
288	0.2	6	10	0.100	2.8	✓	
289	0.2	6	10	0.120	3.4	✓	
290	0.2	7	10	0.005	0.1	✓	
291	0.2	7	10	0.020	0.6	✓	
292	0.2	7	10	0.050	1.4	✓	
293	0.2	7	10	0.100	2.8	✓	
294	0.2	7	10	0.120	3.4	✓	
295	0.2	8	10	0.005	0.1	✓	
296	0.2	8	10	0.020	0.6	✓	
297	0.2	8	10	0.050	1.4	✓	
298	0.2	8	10	0.100	2.8	✓	
299	0.2	8	10	0.120	3.4	✓	
300	0.2	9	10	0.005	0.1	✓	
301	0.2	9	10	0.020	0.6	✓	
302	0.2	9	10	0.050	1.4	✓	
303	0.2	9	10	0.100	2.8	✓	
304	0.2	9	10	0.120	3.4	✓	
Flow Visualization							
305	0.5	9	5	0.100	7.1	✓	✓
306	0.5	9	5	0.100	7.1	✓	✓

Run No.	Mach	Angle of Attack		Frequency		Press.	PIV
		Mean	Amp.	Red.	Hz		
307	0.5	11	5	0.100	7.1	✓	✓
308	0.5	11	5	0.100	7.1	✓	✓
309	0.5	7	10	0.100	7.1	✓	✓
310	0.5	7	10	0.100	7.1	✓	✓
311	0.5	9	10	0.100	7.1	✓	✓
312	0.5	9	10	0.100	7.1	✓	✓
313	0.4	9	5	0.100	5.7	✓	✓
314	0.4	9	5	0.100	5.7	✓	✓
315	0.4	11	5	0.100	5.7	✓	✓
316	0.4	11	5	0.100	5.7	✓	✓
317	0.4	7	10	0.100	5.7	✓	✓
318	0.4	7	10	0.100	5.7	✓	✓
319	0.4	9	10	0.100	5.7	✓	✓
320	0.4	9	10	0.100	5.7	✓	✓
320	0.3	9	5	0.100	4.3	✓	✓
321	0.3	9	5	0.100	4.3	✓	✓
322	0.3	11	5	0.100	4.3	✓	✓
323	0.3	11	5	0.100	4.3	✓	✓
324	0.3	7	10	0.100	4.3	✓	✓
325	0.3	7	10	0.100	4.3	✓	✓
326	0.3	9	10	0.100	4.3	✓	✓
327	0.3	9	10	0.100	4.3	✓	✓

CFD Simulations

Calculations of static and dynamic stall can provide insight to the placement and effectiveness of sweeping-jet actuators for flow control. The calculations are resource intensive and are subject to the limitations of numerical accuracy that may be significant in simulations with large separated flows. Nevertheless, results from computational fluid dynamics are presented in this section because they are generally accurate up until the inception of stall. Both static and dynamic scenarios are presented. Two levels of fidelity are offered. The first is strictly two-dimensional and is useful to identify conditions which will benefit from flow control. The second is three-dimensional where higher fidelity is sought in the modeling of the separated flow region and for the interactional aerodynamics with the sweeping jets. In both situations, simulations are produced by OVERFLOW [10].

Two-Dimensional Flow Simulations

Two-dimensional calculations were run on the VR-7 geometry using a C-grid topology. The surface contains 549 points including 13 points along the finite-thickness trailing edge. The wake is captured with 73 points leading to the far-field which is 25 chord-lengths away. There are 241 points normal to the surface, with the initial spacing set to produce a $y+ < 1$ for most conditions analyzed. The turbulence in the boundary layer is modeled with the Spalart-Allmaras equations and calculations assume fully turbulent conditions.

Results were obtained for both a static and pitching VR-7 across the Mach number range from 0.2 to 0.5. The uncontrolled static results are shown in Figure 26 for lift and Figure 27 for pitching moment. The results indicate a gentle reduction in lift coefficient past the stall angle, in contrast to an abrupt reduction which is a typical indicator of leading-edge separation. The flow visualization in Figure 28, just beyond the maximum lift coefficient at Mach 0.5, confirms that the flow is still attached through the front section of the airfoil. This is a good indicator that active flow control with actuators placed near the leading edge could improve flow attachment beyond the angle of natural separation. Fluidic control devices in a region of separated flow are not generally effective.

A number of dynamic simulations were also evaluated to address flow controllability under conditions which are more representative of an airfoil on a rotor. Table 2 summarizes the conditions and Figure 29 to Figure 40 show the lift and pitching moment hysteresis curves for the cases. Generally, low Mach number cases have small hysteresis loops and no large adverse pitching moment excursions. Benefits of active flow control would appear most prominently at Mach numbers of 0.4 and greater for traditional helicopters. Flow visualization for Case 1 near the peak angle of attack reveals separated flow creeping from the trailing edge and moving forward; a scenario where sweeping jets AFC is expected to help. However, the simulation repeated at a higher reduced frequency (Case 2) has a hysteresis loop with characteristic leading-edge separation. This situation is more challenging to control.

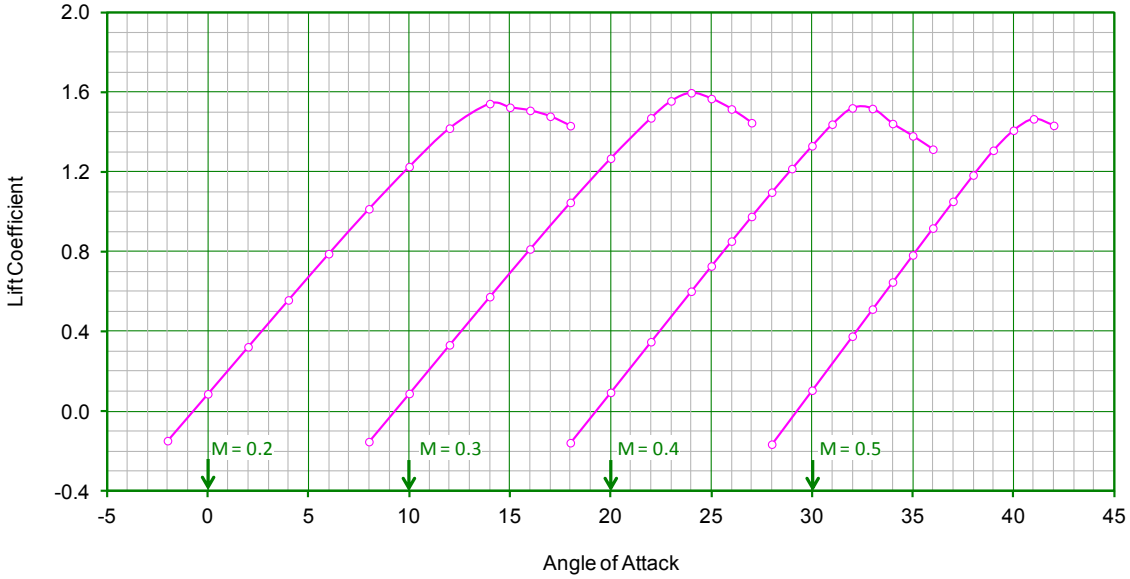

Figure 26: Lift predictions from OVERFLOW for the VR-7 at sea-level standard conditions (Chord = 1 ft).

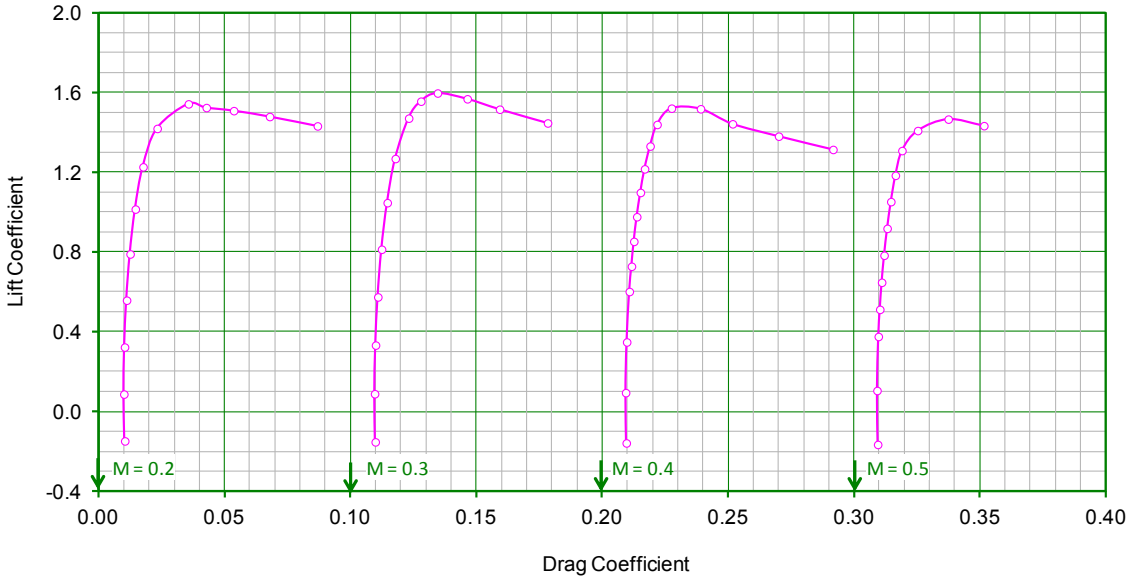

Figure 27: Pitching moment predictions from OVERFLOW for the VR-7 at sea-level standard conditions (Chord = 1 ft).

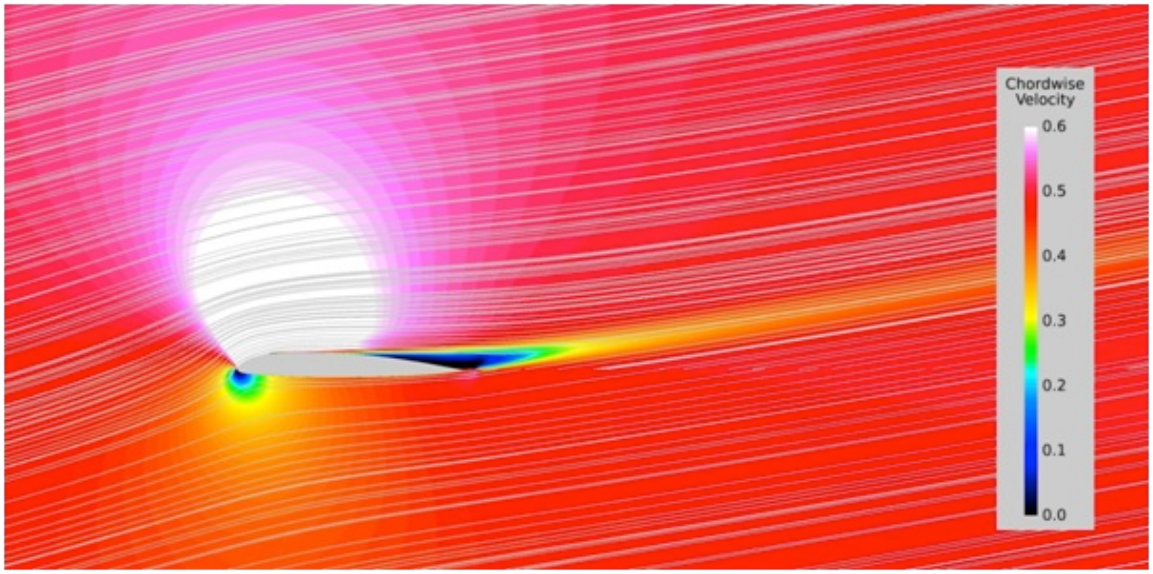

Figure 28: Chordwise Mach number contours (black indicates separation) for the VR-7 at Mach 0.5; sea-level standard conditions (chord = 1 ft). The angle of attack is 12°.

Table 2: Table of analysis conditions for the VR-7.

Case	Mach	α_{Min}	α_{Max}	k
1	0.4	10	5	0.05
2	0.4	10	5	0.10
3	0.4	6	10	0.05
4	0.4	6	10	0.10
5	0.3	10	5	0.05
6	0.3	10	5	0.10
7	0.3	6	10	0.05
8	0.3	6	10	0.10
9	0.2	10	5	0.05
10	0.2	10	5	0.10
11	0.2	6	10	0.05
12	0.2	6	10	0.10

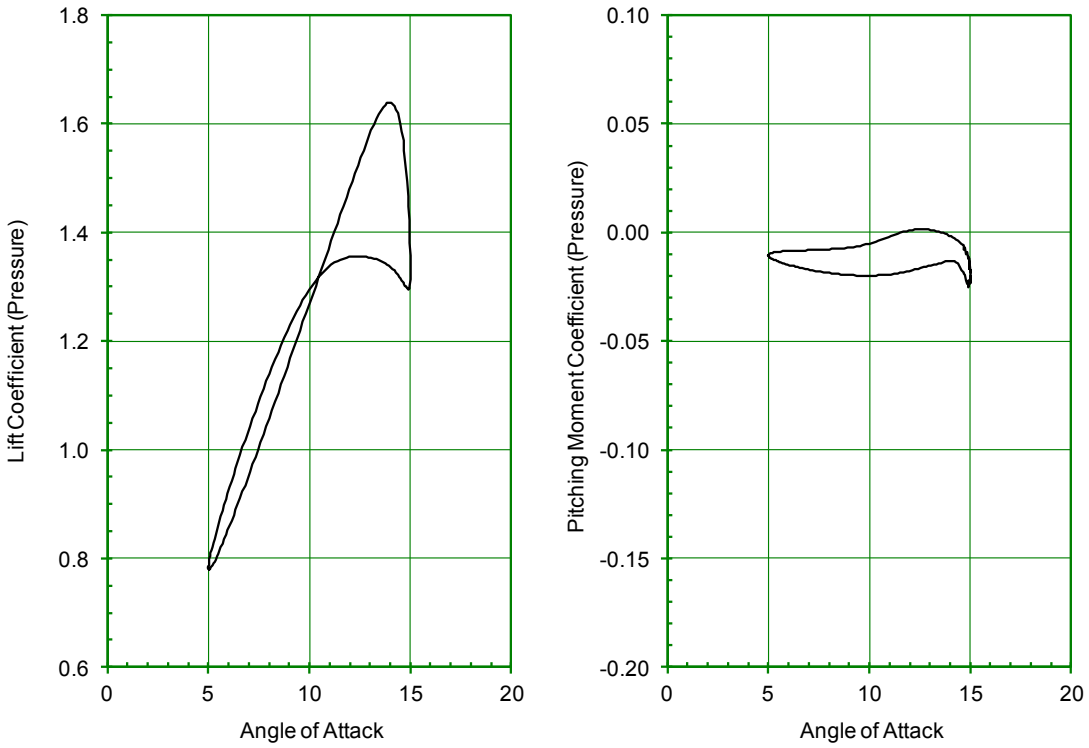

Figure 29: Lift and pitching moment predictions from OVERFLOW for the VR-7 at sea-level standard conditions for Case 1, $M_\infty = 0.4$, $\alpha = 10 \pm 5$, k = 0.05, chord = 1 ft.

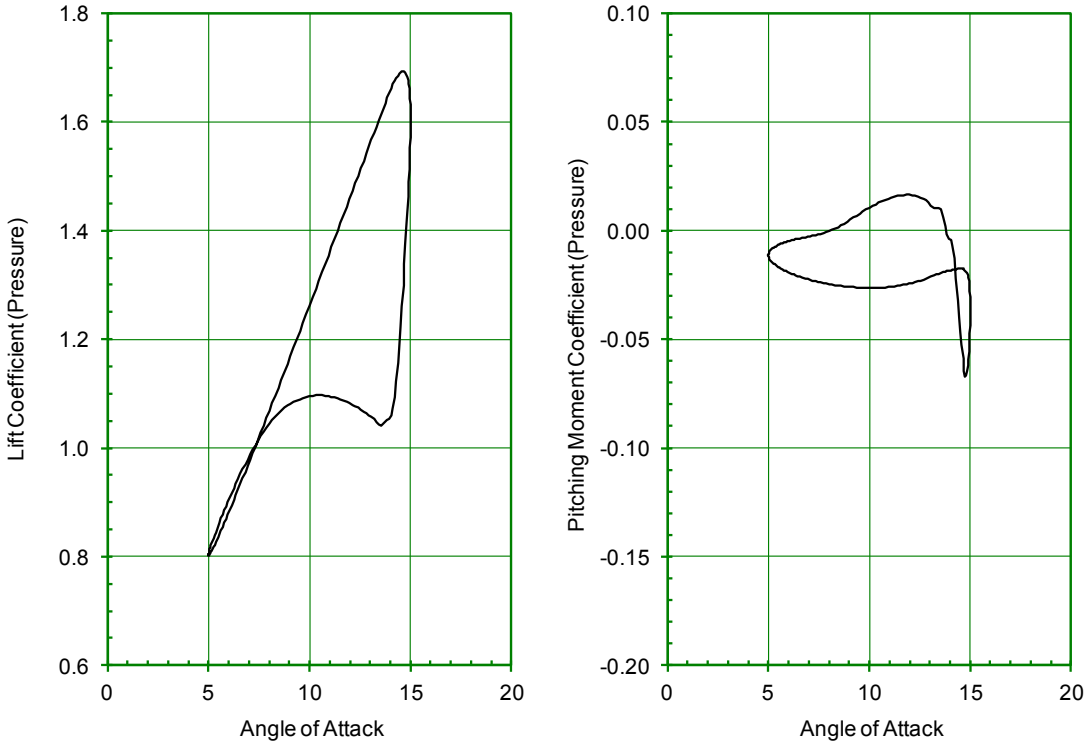

Figure 30: Lift and pitching moment predictions from OVERFLOW for the VR-7 at sea-level standard conditions for Case 2, $M_\infty = 0.4$, $\alpha = 10 \pm 5$, k = 0.10, chord = 1 ft.

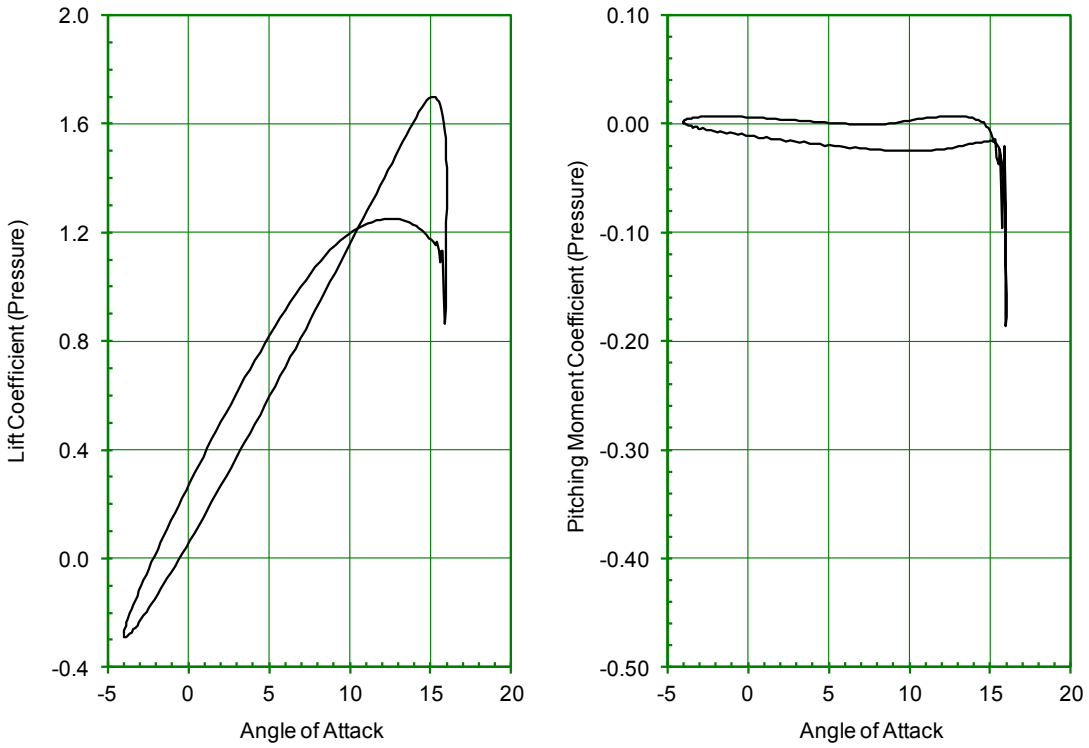

Figure 31: Lift and pitching moment predictions from OVERFLOW for the VR-7 at sea-level standard conditions for Case 3, M_{∞} = 0.4, α = 6 ± 10, k = 0.05, chord = 1 ft.

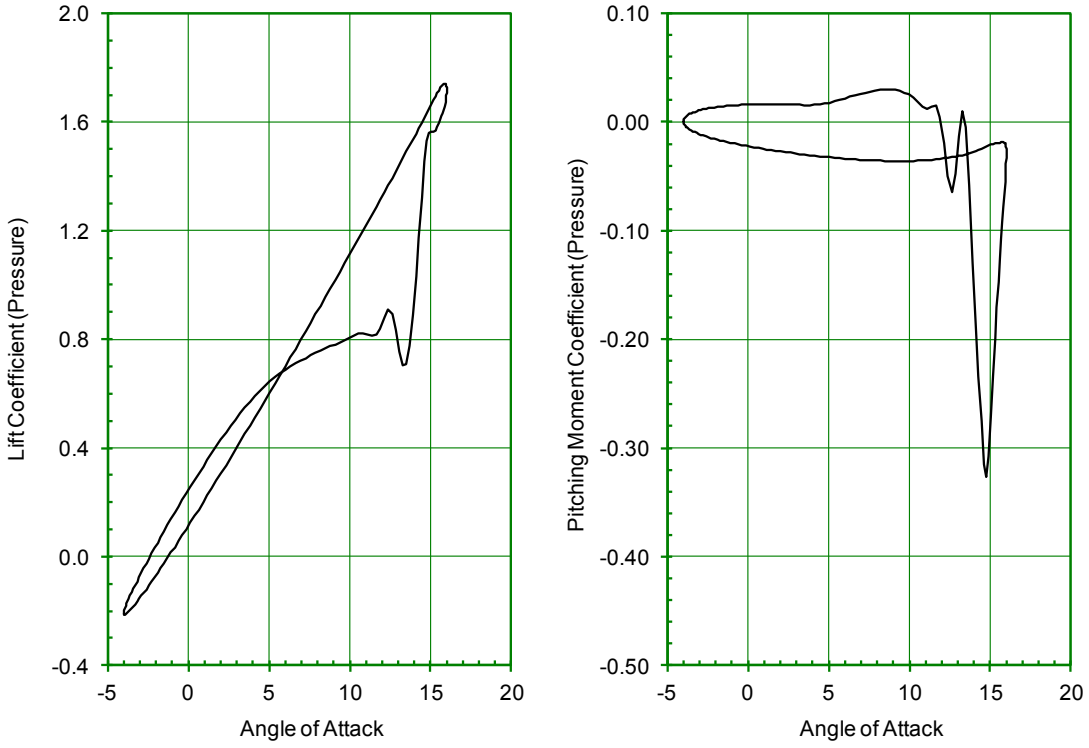

Figure 32: Lift and pitching moment predictions from OVERFLOW for the VR-7 at sea-level standard conditions for Case 4, M_{∞} = 0.4, α = 6 ± 10, k = 0.10, chord = 1 ft.

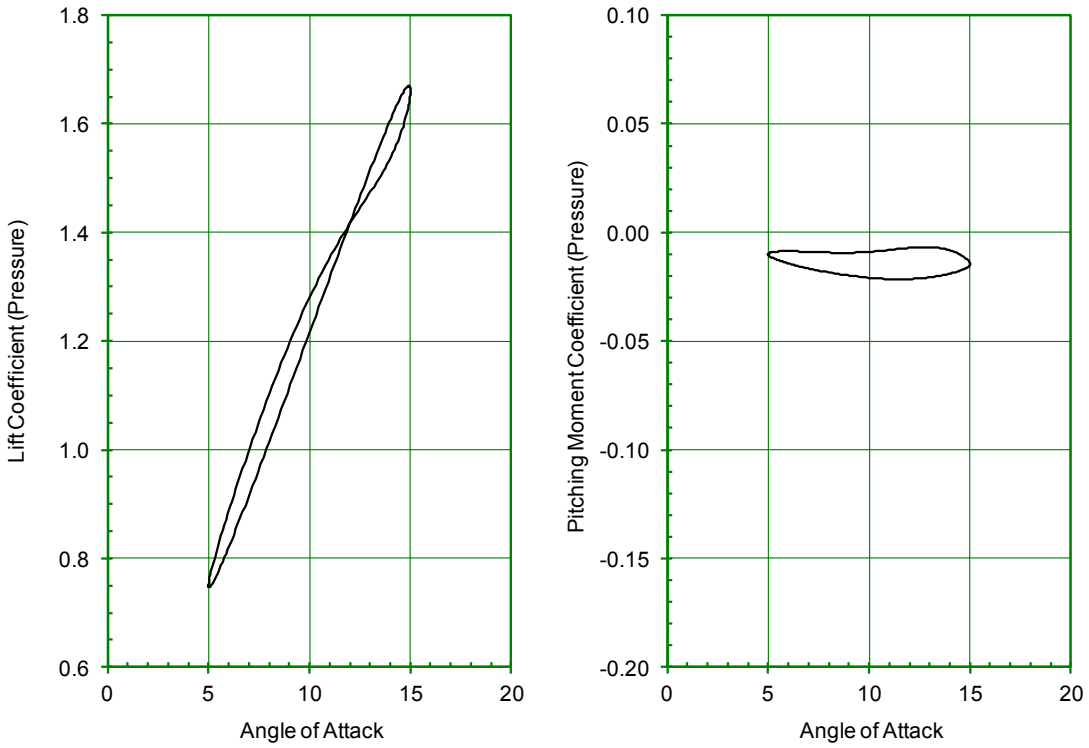

Figure 33: Lift and pitching moment predictions from OVERFLOW for the VR-7 at sea-level standard conditions for Case 5, $M_\infty = 0.3$, $\alpha = 10 \pm 5$, k = 0.05, chord = 1 ft.

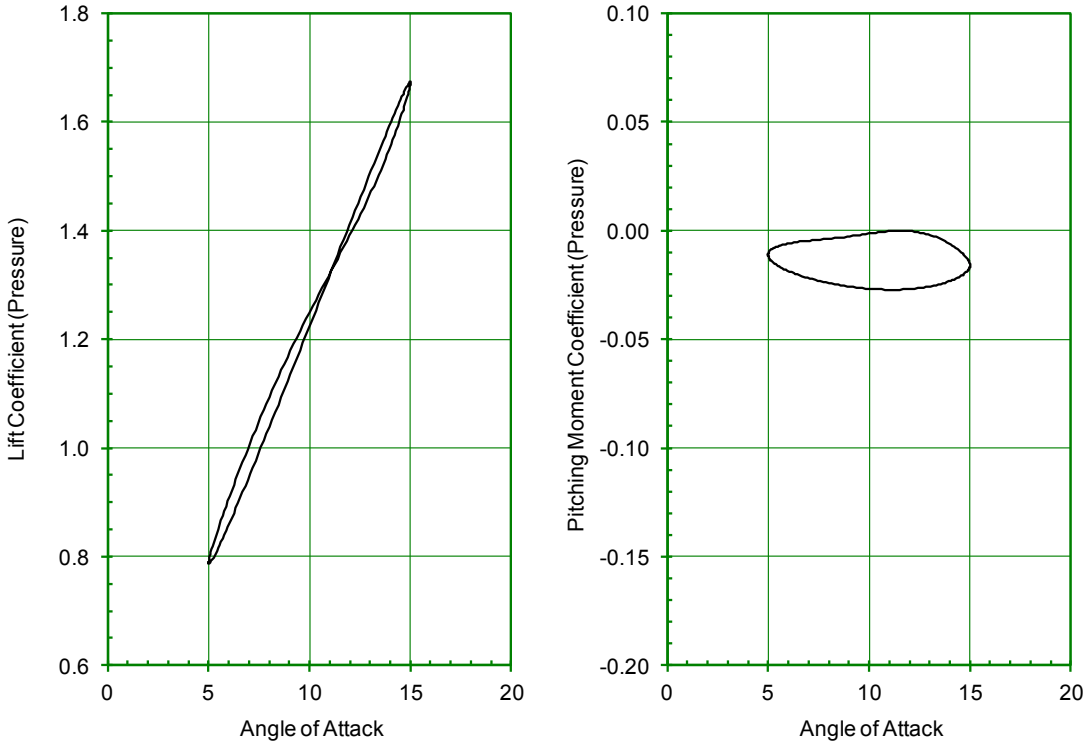

Figure 34: Lift and pitching moment predictions from OVERFLOW for the VR-7 at sea-level standard conditions for Case 6, $M_\infty = 0.3$, $\alpha = 10 \pm 5$, k = 0.10, chord = 1 ft.

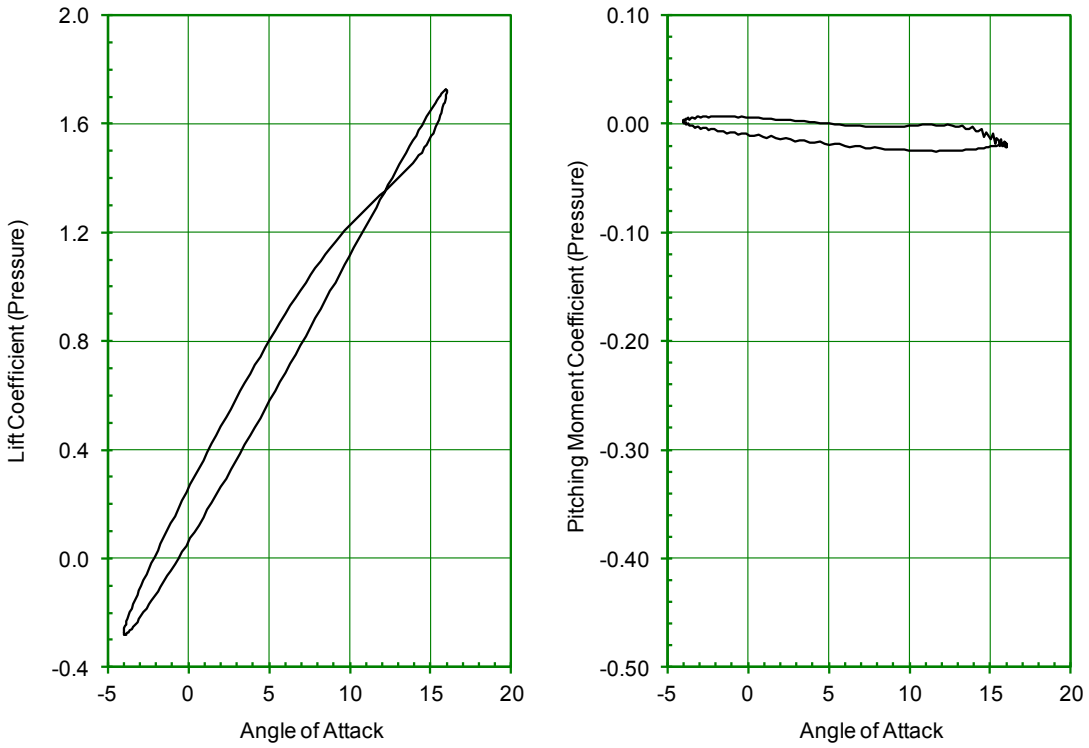

Figure 35: Lift and pitching moment predictions from OVERFLOW for the VR-7 at sea-level standard conditions for Case 7, M_{∞} = 0.3, α = 6 ± 10, k = 0.05, chord = 1 ft.

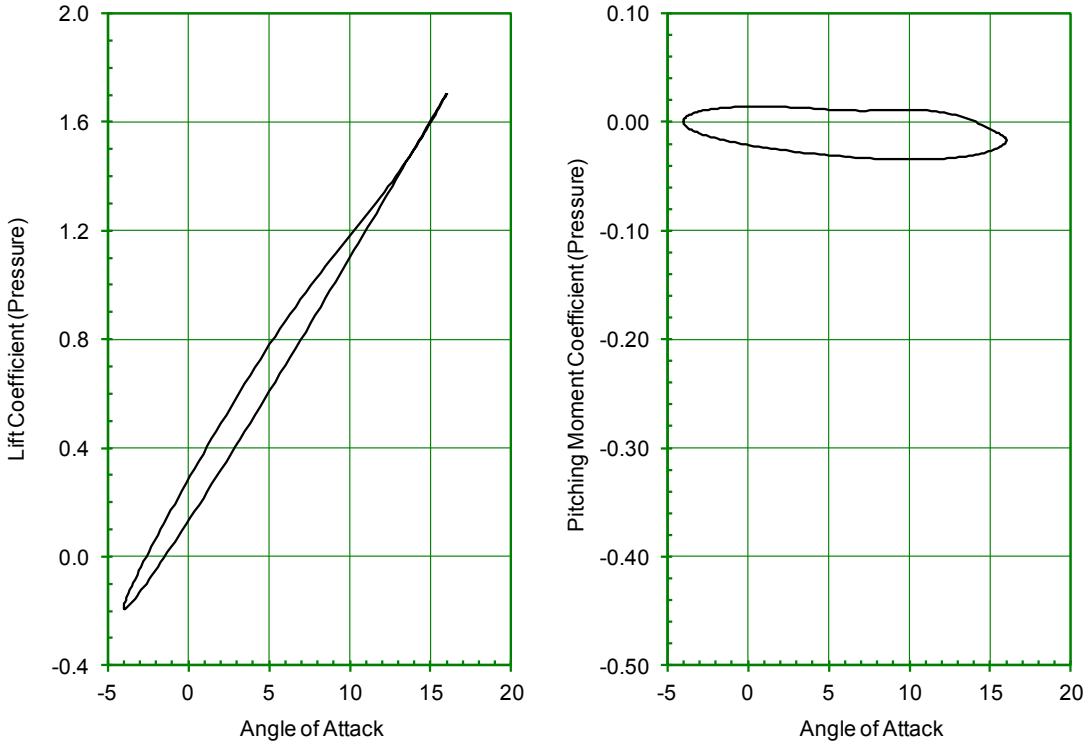

Figure 36: Lift and pitching moment predictions from OVERFLOW for the VR-7 at sea-level standard conditions for Case 8, M_{∞} = 0.3, α = 6 ± 10, k = 0.10, chord = 1 ft.

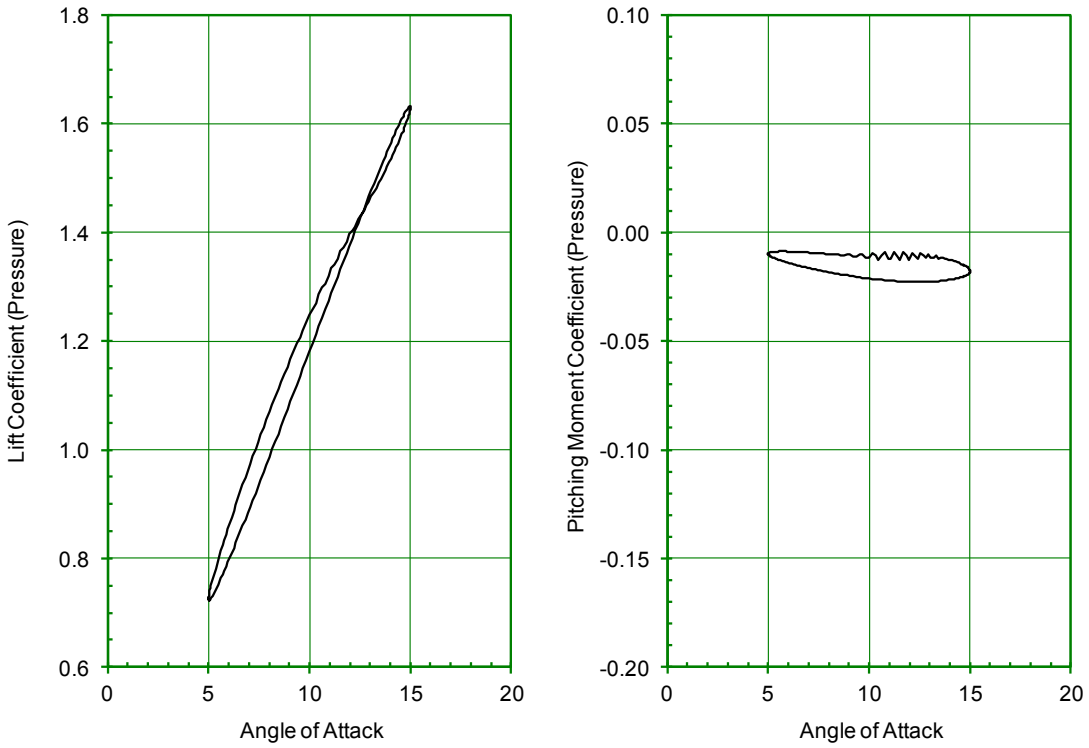

Figure 37: Lift and pitching moment predictions from OVERFLOW for the VR-7 at sea-level standard conditions for Case 9, $M_\infty = 0.2$, $\alpha = 10 \pm 5$, k = 0.05, chord = 1 ft.

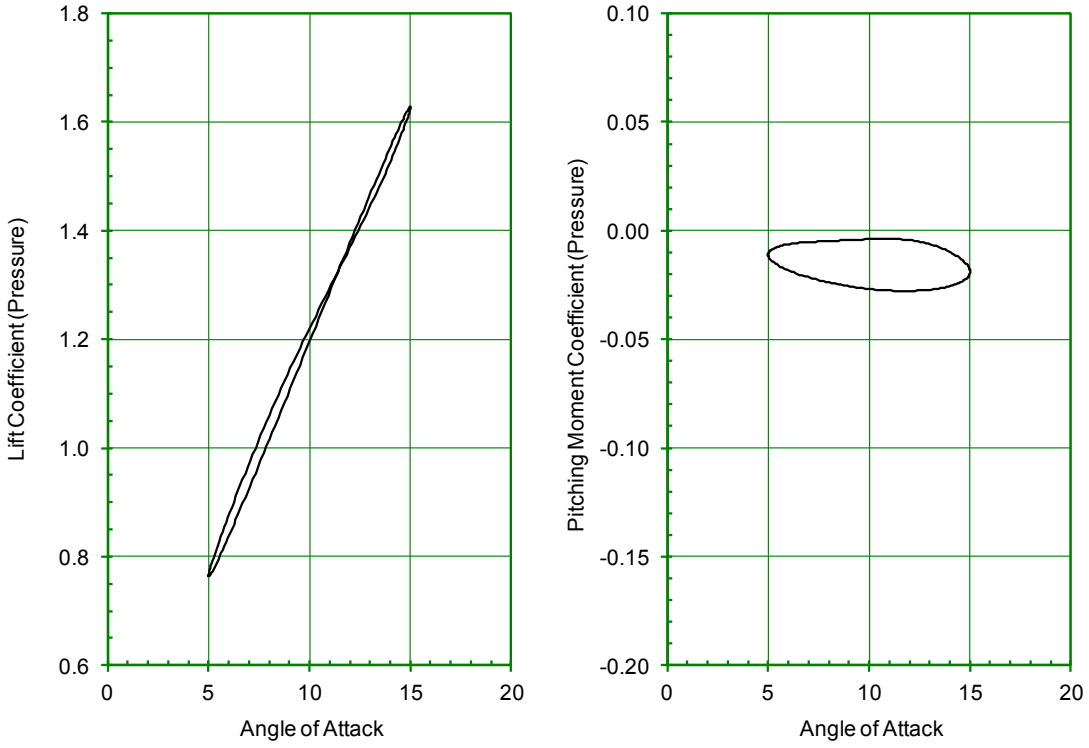

Figure 38: Lift and pitching moment predictions from OVERFLOW for the VR-7 at sea-level standard conditions for Case 10, $M_\infty = 0.2$, $\alpha = 10 \pm 5$, k = 0.10, chord = 1 ft.

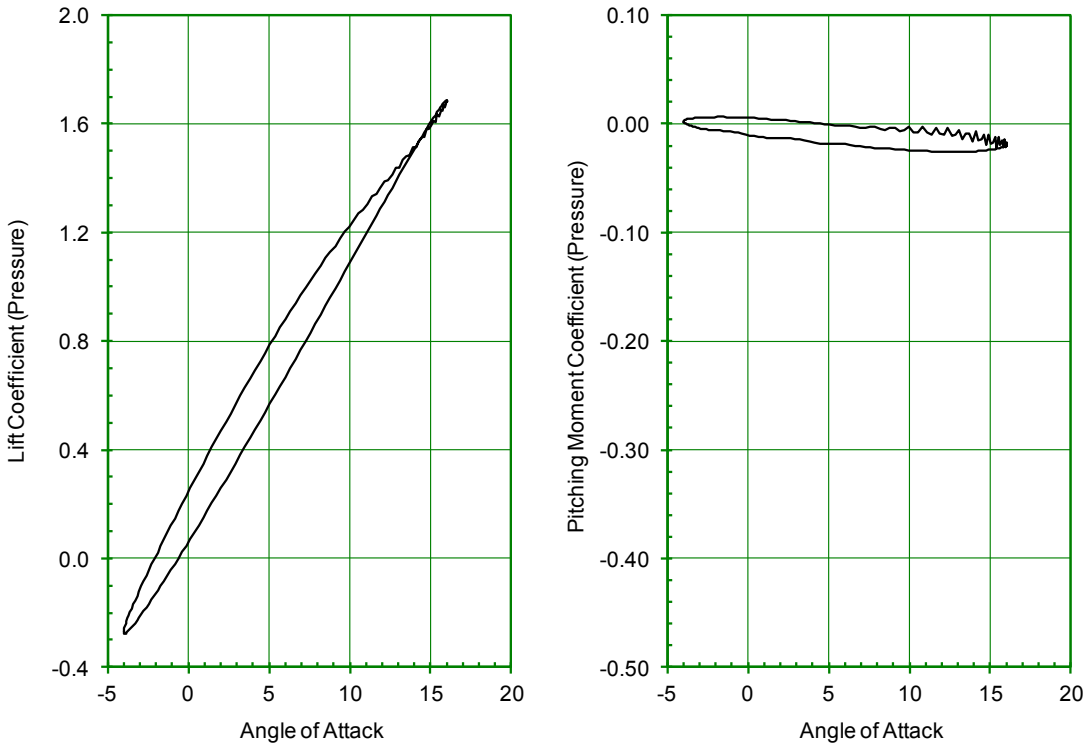

Figure 39: Lift and pitching moment predictions from OVERFLOW for the VR-7 at sea-level standard conditions for Case 11, $M_\infty = 0.2$, $\alpha = 6 \pm 10$, k = 0.05 chord = 1 ft.

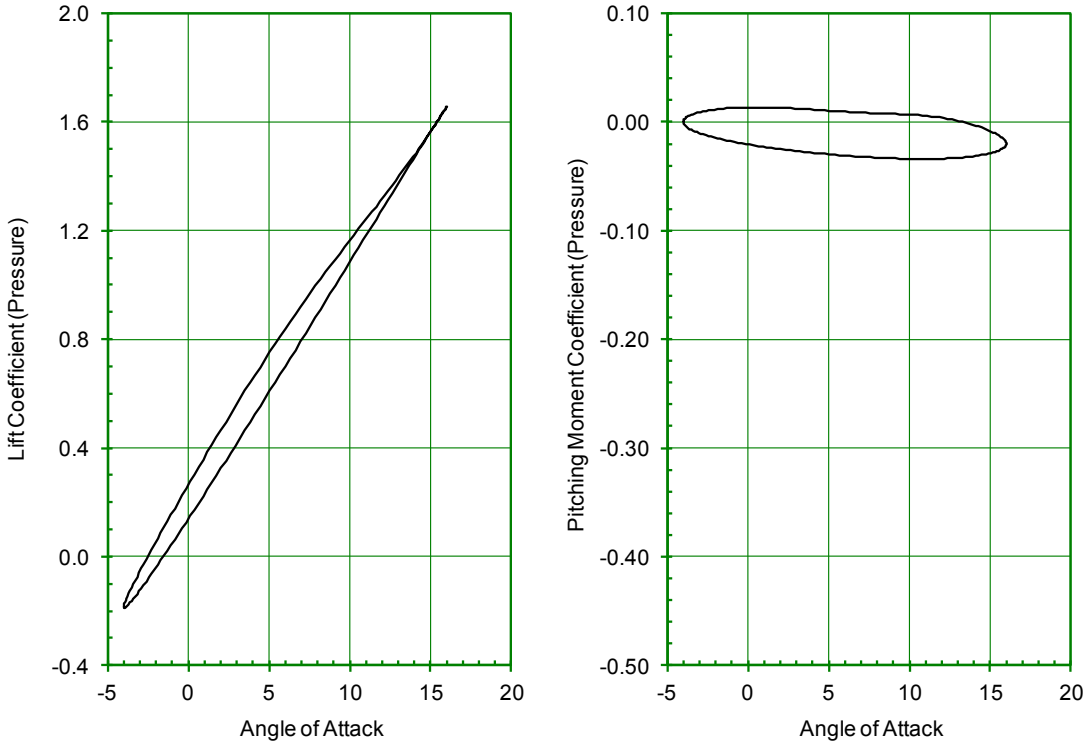

Figure 40: Lift and pitching moment predictions from OVERFLOW for the VR-7 at sea-level standard conditions for Case 12, $M_\infty = 0.2$, $\alpha = 6 \pm 10$, k = 0.10, chord = 1 ft.

α = 14.763°

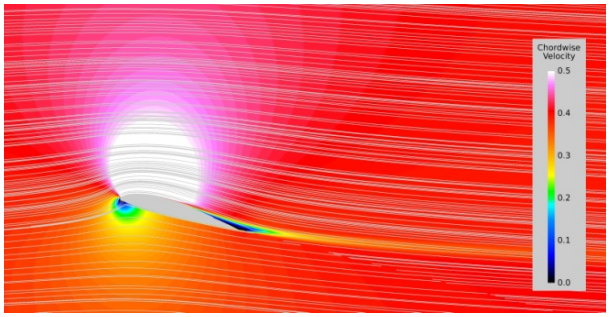

α = 15.298°

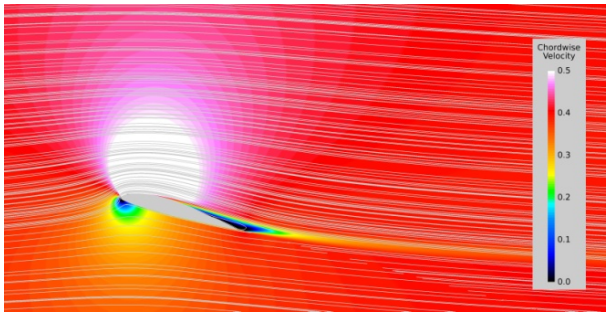

α = 15.685°

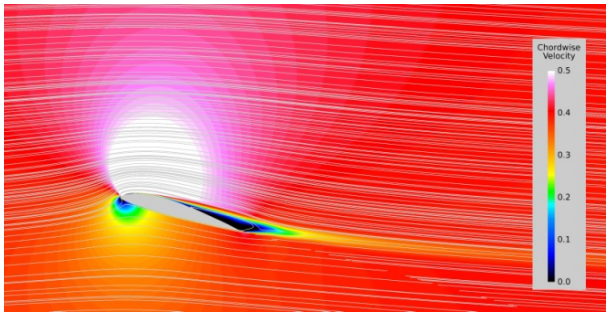

α = 15.921°

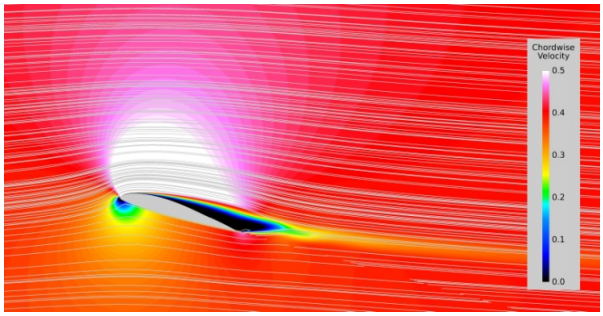

α = 16.000°

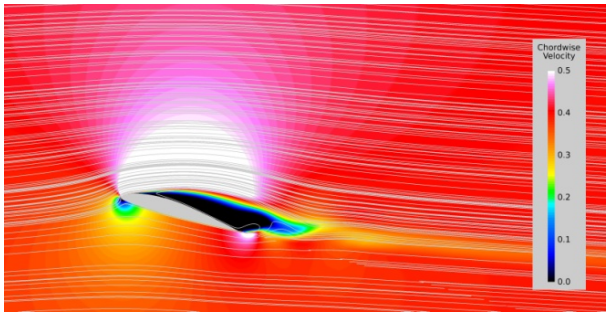

Figure 41: Contours of chordwise velocity (black indicates separation) for the VR-7 for flow near the peak of the lift hysteresis. The dynamic stall condition is Mach 0.4, α = 6°±10°, k = 0.05, chord = 1 ft, sea-level standard.

Two-dimensional simulations are attractive since they are an order- of-magnitude faster to run. However, to analyze sweeping jet effects, two dimensional analysis misses much of the physics since the cross flow is absent. Two-dimensional analysis can model a steady jet from a slot and the impact of the jet on the separated flow can be quantified. This analysis was done for a stationary airfoil subject to Mach 0.5 flow. Note that the chord was increased to 15 inches, the same as the wind-tunnel model. The results on lift and pitching moment are shown in Figure 42. In this simulation, the jet was positioned at 10% chord and angled at 30 degrees to the local surface. The momentum coefficient, defined as

$$C_\mu = 2\frac{h}{c}\left(\frac{M_j}{M_\infty}\right)^2, \tag{1}$$

is set to 0.3%, which value produces a jet Mach number of approximately 1.0. The jet produces more than a 10% increase in the maximum lift coefficient and the flow remains attached beyond the angle where separation would occur under natural condition. Though surely not conclusive because of the limited nature of the two-dimensional calculation, nevertheless, it does show the benefit of a strong jet from a slot.

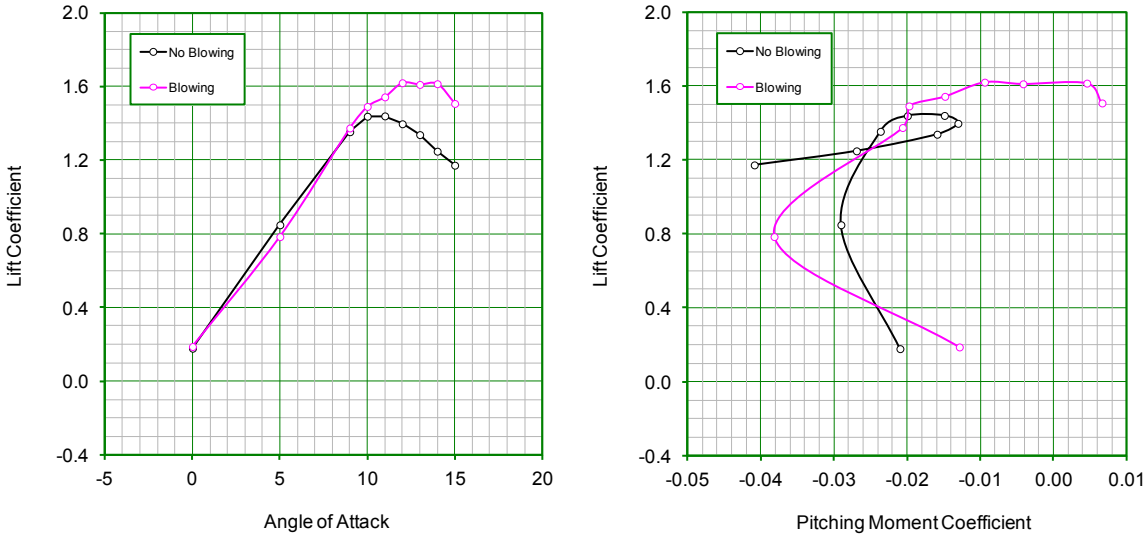

Figure 42: Two-dimensional CFD evaluation of steady blowing on a stationary 15”-chord VR-7 airfoil at Mach 0.5, sea-level standard conditions.

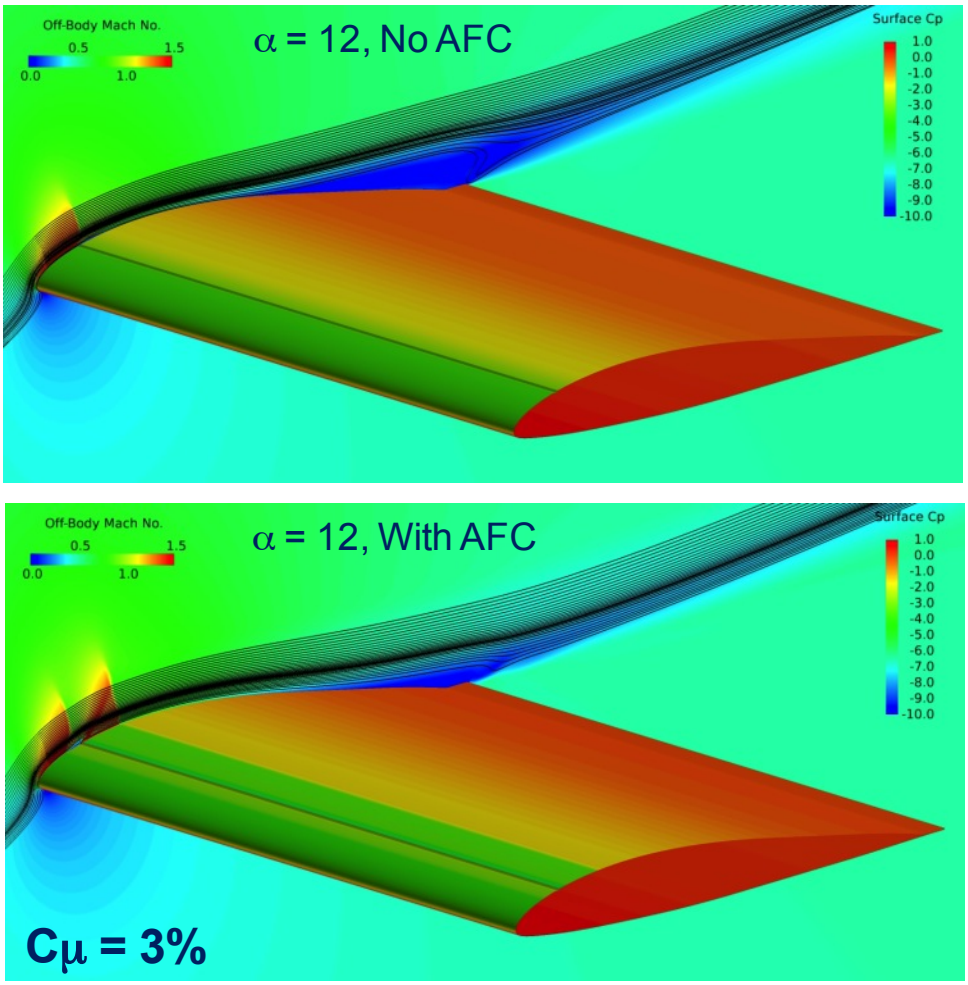

Figure 43: Flow field visualization with and without steady blowing from the 10% chord location. The simulation is the 15"-chord VR-7 airfoil at Mach 0.5, α = 12°, sea-level standard conditions.

Three-Dimensional Flow Simulations

Three-dimensional flow calculations over the airfoil section not only offer the ability to model the sweeping jet by adding the cross flow direction, it also allows for better modeling of the separated flow region, which is inherently three-dimensional. To perform the calculations, the two-dimensional grid was extruded in the spanwise direction over a distance equivalent to the width of a sweeping -jet actuator (0.5"). There are 81 computational planes in the spanwise direction. Periodic boundary conditions were applied at the edges to simulate an infinitely long wing with an array of actuators. The jet is modeled with a sprinkler-type boundary condition where the mass flow, sweep angle, and oscillation frequency are specified. The jet is placed at the mid span of the CFD model over a width of 1mm. The periodic boundary conditions which endplate the computational domain means that the simulation will capture the effects of an array of perfectly synchronous jets; however, this may not be the ideal mode of operation nor is it something that can be controlled in the lab.

The sweeping jet, located at 8% chord, is modeled within an embedded block that has an increased cell density to capture interactional aerodynamic effects. Though the jet is located at

the center of the computational domain, the embedded grid runs across the span of the airfoil. It has a slot to direct the jet at a 30 degree angle to the airfoil surface. The CFD grid is shown in Figure 44 with an expanded view of the embedded block. The dark patch is the location of the jet.

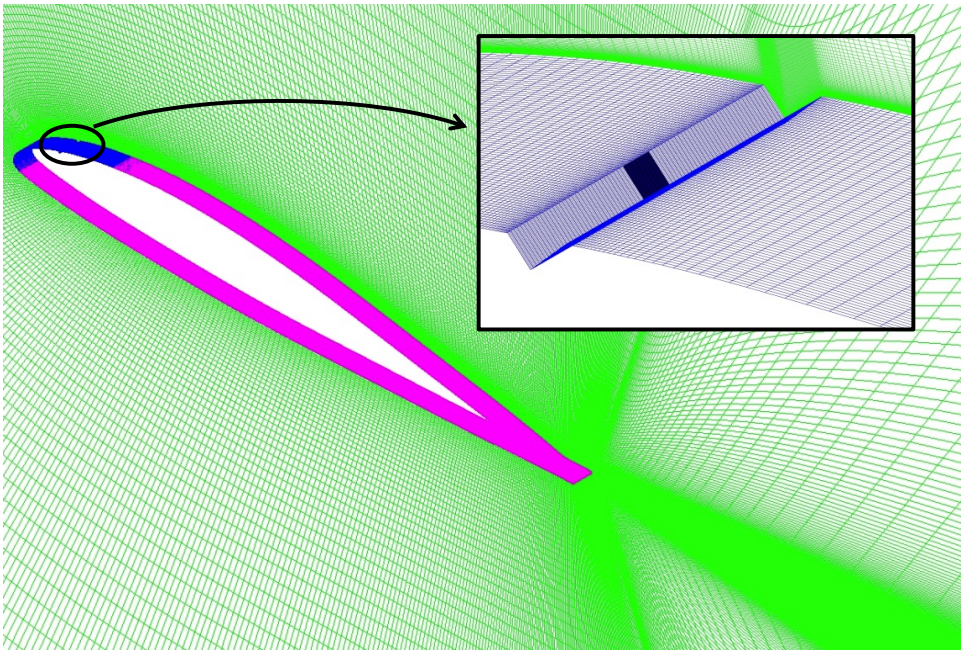

Figure 44: Computational grid for the thee-dimensional calculations.

In the calculations presented herein, the boundary layer turbulence is modeled using the Spalart-Allmaras approach; detached-eddy simulation is used elsewhere. This approach captures some very fine details in the turbulent wakes of massively separated flow, though the limited spanwise extent of the domain may not be sufficiently wide to capture these with great accuracy.

Static stall calculations were revisited with the three-dimensional CFD model first. For low angles of attack below the inception of stall, the model was run in OVERFLOW's steady-state mode. For angles of 12.5 degrees and higher, the calculations are time-accurate using a time-step such that 100 iterations are executed within one period of an oscillating jet. Twenty Newton sub-iterations are used to converge the solution between time-steps.

The static calculations simulate Mach 0.4 flow over the VR-7 airfoil at sea-level standard atmospheric conditions. For the jet, a mass flow rate was used to produce a jet of roughly Mach 0.92. The jet was set to oscillates between ±60 degrees at a frequency of 350 Hz, which is much slower than the expected sweep frequency range between 1 and 2 KHz. The lower frequency was chosen to avoid excessive simulation run times, particularly in dynamic stall simulations where several airfoil pitch cycles are desired. It turns out that the period of an oscillating jet is nearly the same as the length of time required by a particle to travel the distance of one chord length. The uncontrolled simulation was run for a sufficient number of solution iterations to

establish a mean of the lift, drag, and pitching moment. Similarly for the flow-control case, a mean was established for the forces and moments well within the 100 jet cycles simulated.

Figure 45 presents the results of the simulation with and without blowing. Only modest improvements in lift are predicted beyond the natural stall and there is no increase in the maximum lift coefficient. This is in contrast to the two-dimensional results that indicated an improvement for a jet blown through a slot along the length of the airfoil. However, the visualization of the three-dimensional flow solution (Figure 46), shows that the jet does impact the flow across the span of the computational domain. One period of the sweeping jet is shown, with the direction of the jet indicated by black arrows. Section cuts of vorticity, taken every ¼-inch, shows the roll-up of a vortex as the flow interacts with the jet. In this sense, the sweeping jet behaves as a vortex generator, but, in addition to producing vortices, the jet adds momentum to the flow. The small change in calculated lift and pitching moment may be caused by the low value of sweeping frequency used. In practice, the jets usually sweep in the kilohertz range at least three times larger than what was simulated. Again, the low frequency was used to minimize the computational cost. However, the simulation results are encouraging since they appear to show what would be expected from flow physics.

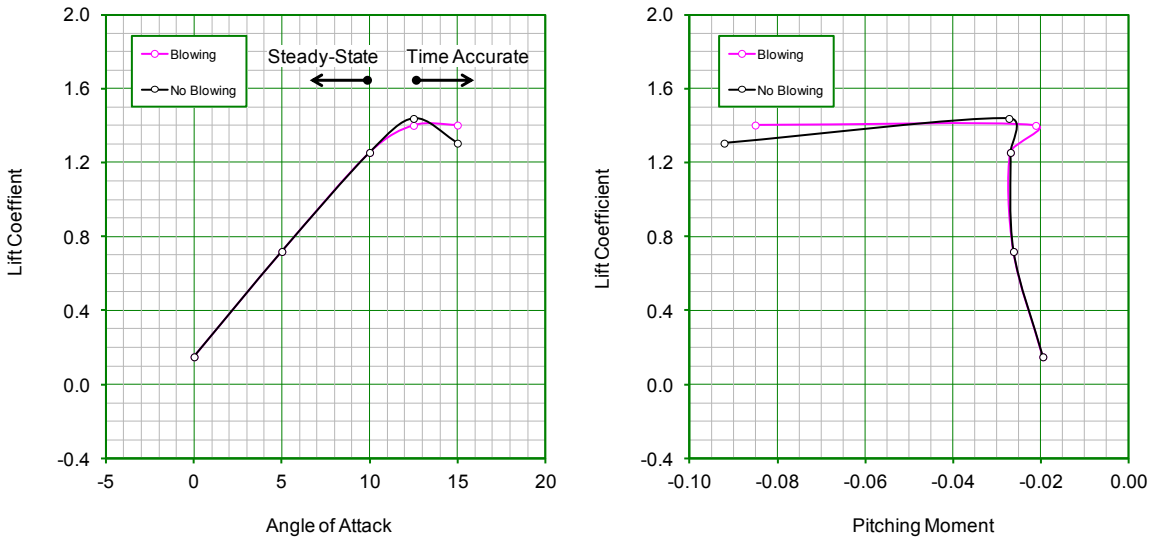

Figure 45: Three-dimensional CFD evaluation of sweeping jets on a stationary 15”-chord VR-7 airfoil at Mach 0.4, sea-level standard conditions; M_{jet} = 0.92, x/C_{jet} = 0.08, f_{jet} = 350 Hz.

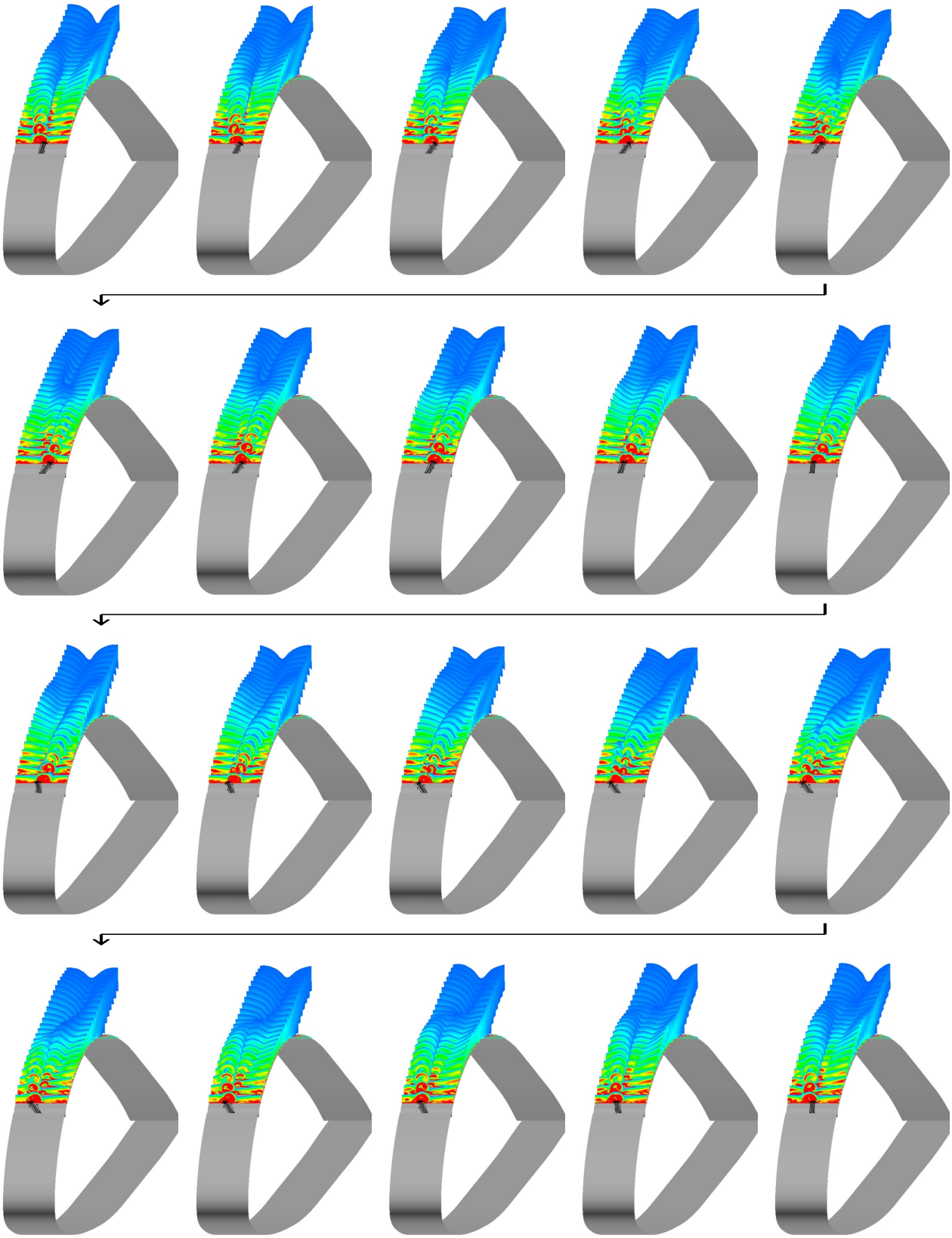

Figure 46: Flow field of the active flow control jet in Mach 0.4 flow at α = 15°.

Calculations to quantify the effectiveness of sweeping jets AFC under dynamic conditions were made for Case 4 (see Table 2). This is a representative Mach number with a large angle of attack excursion from the mean. This case is of interest because it occurs on each rotor blade of a 50,000lbs Chinook flying at 130 knots, at 4,000 feet on a 95 °F day. Figure 47 shows the lift and moment hysteresis curves. The uncontrolled results resemble the two-dimensional counterparts shown in Figure 32.

The sweeping jet shows that it reduces the size of the loop of the lift hysteresis curve and the pitching moment excursion after stall. For this case, the jet was sweeping at 350 Hz while the airfoil was oscillating at 11.4 Hz. Thus, the jet is not pointed in the same direction each time the airfoil reaches its peak angle of attack. To thoroughly evaluate the jet effects, the simulation should go through several pitch cycles to quantify an average effect of the jet. For the sake of computational resources, only two pitch cycles were computed with no appreciable difference in the hysteresis loops.

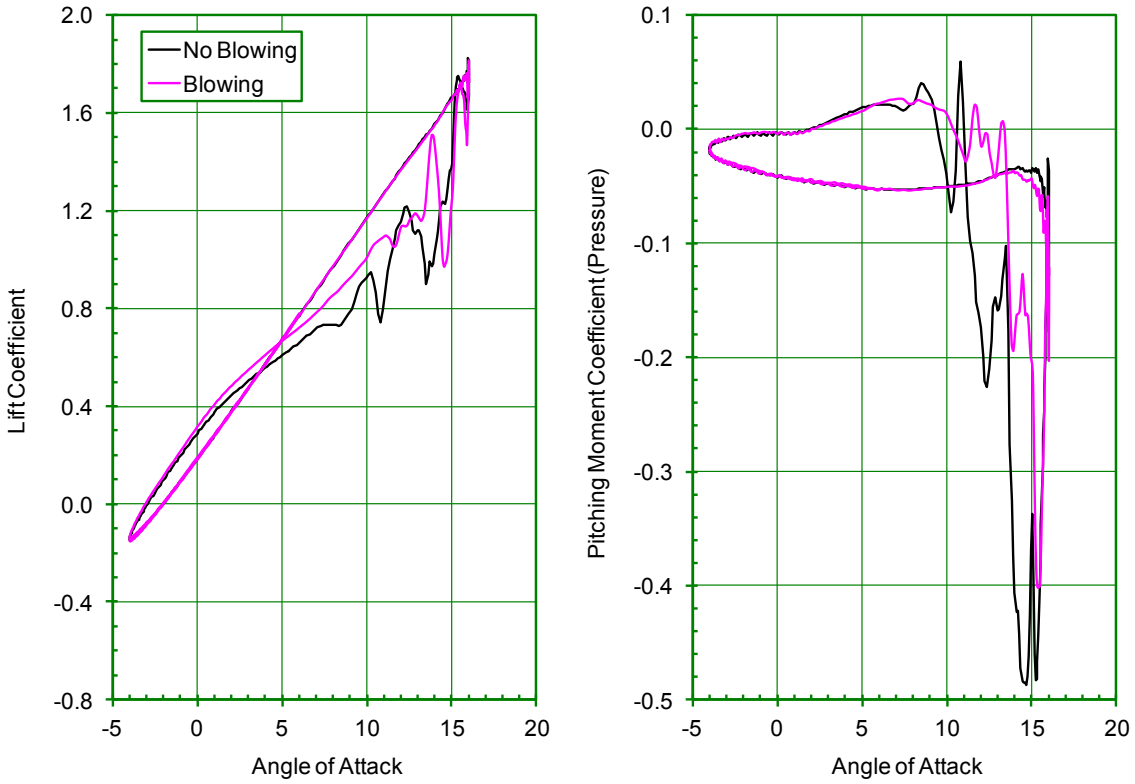

Figure 47: The effect of sweeping jets on lift of the VR-7 airfoil at Mach 0.4, k = 0.1, α = 6+10sin(ωt); M_{jet} = 0.92, x/C_{jet} = 0.08, f_{jet} = 350 Hz.

Summary

This report summarizes the work accomplished in the first year of what was originally a three-year program to investigate the use of active flow control (AFC) to improve the performance of airfoils on a helicopter rotor blade. Unfortunately, budget constraints modified the plan and reduced the original program to one year. The AFC technique selected uses sweeping-jet actuator inserted in the upper surface near the leading edge of an oscillating airfoil subject to flow velocities up to Mach 0.5. The application is to helicopter rotors that are subject to dynamic stall in high-speed forward flight. The planned approach is primarily experimental, with CFD introduced to lend insight to actuator flow effects and actuator placement, as well as underlying flow physics.

The CFD approach utilizes the OVERFLOW code to model a section of the airfoil having the width of one sweeping-jet actuator. Detached-eddy simulation with the Spalart Allmaras turbulence model in the boundary layer was used to capture the jet interactional aerodynamics and potentially large regions of separated flow in the wake. The jet was modeled with a sprinkler-jet boundary condition with specified mass-flow.

The larger experimental portion of this program would use the Oran W. Nicks Low Speed Wind Tunnel located on the campus of Texas A&M University. The facility is ideally suited for this test because of its oscillating-pitch rig, PIV measurement capability, and affordability. The current configuration is not capable of reaching the desired rotor-relevant Mach numbers without several modifications. A design is presented for a reduced cross-sectional area test section, contraction section, diffuser section, and tunnel circuit efficiency improvements. These tunnel improvements promise to make the LSWT at TAMU more capable for future programs.

The test model would use a 5-ft span wing having a 15-inch chord VR-7 airfoil. The wing would span a new 6x5 ft insert to the test section of the 7 x 10 ft Texas A&M wind tunnel so as to produce Mach 0.5 flow, appropriate to the helicopter high-speed flight condition of interest. The test article is modular, featuring an interchangeable leading edge designed to contain fluidic actuator arrays positioned at 8% chord with the jet angled at 30 degrees to the local airfoil surface. The actuator array can contain up to 100 jets to span the 5-foot wide airfoil section, spaced nominally 0.5 inches apart. In future tests, the interchangeable leading edge could be modified to test other active flow devices, such as plasma actuators.

The primary recordable data are surface pressures along a chord section. Data will be measured at 45 locations with ESP modules. These locations were determined using a design-of-experiments optimization process to minimize numerical error from lift, drag, and pitching moment integration. Particle Image Velocimetry and hot film measurements are planned.

A lot has been accomplished in this abbreviated one year study. A sweeping-jet active-flow-controlled airfoil model has been designed, and required improvements to the Texas A&M 7 x 10 wind tunnel have been defined, analyzed, and detailed. In addition, a CFD model of a sweeping jet has been developed and exercised to predict the detailed physics of the unsteady flows from the actuators and the effect on the flow over pitching airfoils.

It is hoped that the work described in this report may be continued.

References

1. Post, M.L., and Corke, T.C., “Separation Control using Plasma Actuators - Stationary and Oscillatory airfoils,” AIAA Paper 2004-0841, 2004.
2. Roupassov D, Nikipelov A, Nudnova M, Starikovskii A (2009) “Flow Separation Control by Plasma Actuator with Nanosecond Pulsed-Periodic Discharge,” AIAA Journal, 2009, vol.47 no.1 (168-185).
3. Hassan, A.A., Straub, F.K., JanakiRam, R.D., Weems, D., “Boeing VGART (Variable Geometry Advanced Rotor Technology) Phase II Program (Active Rotor Technologies), Final Report,” Boeing Report No. L9K6-FR-03301, March 2003.
4. Narducci, R.P., Tadghighi, H., “Rotor Designs with Improved Static / Dynamic Stall Characteristics,” Final Report prepared for the National Rotorcraft Technology Center / Center for Rotorcraft Innovation, March 2010.
5. T. Srinivas, B. Vasudevan & A. Prabhu, “Performance of Fluidically Oscillating Jet” Turbulence Management and Relaminarization, H. Liepmann & R. Narasimha editors (IUTAM Symposium Bangalore 1987).
6. Lucas, N., Taubert, L., Woszidlo, R., Wygnanski, I., McVeigh, M.A., “Discrete Sweeping Jets as Tools for Separation Control”, AIAA 2008-3868, 4th Flow Control Conference, Seattle, Washington, June 23-26, 2008.
7. Sahlin, A., Johansson, A.V., “Design of guide vanes for minimizing the pressure loss in sharp bends,” Physics of Fluids A (ISSN 0899-8213), vol. 3, Aug. 1991, p. 1934-1940.
8. Eckert, Mort, Jope, “Aerodynamic Design Guidelines and Computer Program for Estimation of Subsonic Wind Tunnel Performance,” NASA TN D-8243, 1976.
9. Raghu, S., “Compact Fluidic Jet Arrays for Flow Control,” Report No. AF-NASA-2011-01, June 2011.
10. Nichols, R., Buning, P., “User’s Manual for OVERFLOW 2.1,” University of Alabama at Birmingham, Birmingham, AL.

Appendix A: Pressure Reconstruction Proof-of-Concept

Steady pressure measurements are common in wind tunnel experimentation, utilizing surface pressure integration to determine aerodynamic properties of lift, pressure drag, and pitching moments. This experimental measurement technique involves employing tubing systems that connect surface pressure ports to pressure transducers, shown in Figure 48. For steady flow conditions, the pressure as measured by the transducer, P_T , is equal in magnitude to the true surface pressure, P_S. However, frictional and viscous effects from the fluid-tubing interactions and pressure wave acoustic resonance cause distortion in amplitude and phase of the unsteady pressure wave. The result is that the pressure measured by the transducer is no longer representative of the local surface pressure. This error propagates through the data analysis, leading to incorrect representation of forces and moments on the airfoil.

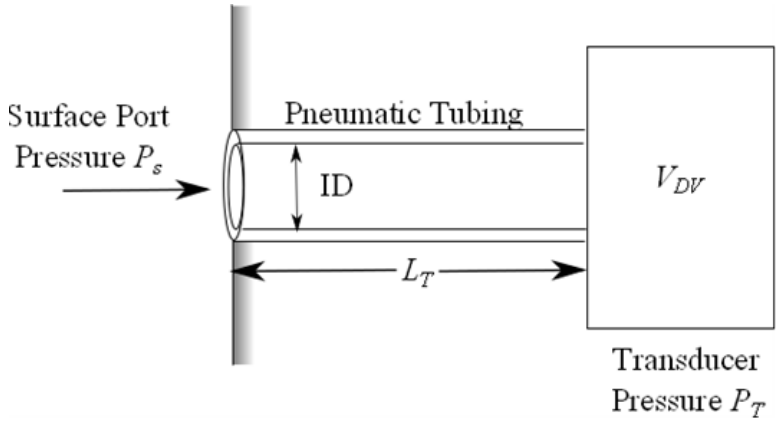

Figure 48: Schematic of a basic pressure tubing system.

There are two common approaches to increase the fidelity of the unsteady pressure measurements. The first is to implement higher quality transducers, such as those manufactured by Kulite or Endevco. Transducers such as these eliminate the need for a pneumatic line connecting the surface pressure tap to the transducer, as they are typically flush mounted to the surface. However, these are fragile, easily damaged, and prohibitively expensive. An alternative approach is to implement a conventional pressure system and then apply a correction, typically by developing a system transfer function. The experimental definition of the transfer function is simply the ratio of the system output to the system input in the complex frequency domain.

$$T = \frac{P_T(\omega)}{P_S(\omega)} \tag{1}$$

The de facto analytic transfer function for pneumatic pressure systems for aerospace and mechanical applications is the Bergh and Tijdeman[1] model. This relation was derived from

basic Navier-Stokes equations with assumptions based upon small sinusoidal pressure disturbances for tubing with small inner diameters, and is defined as

$$\frac{P_T(\omega)}{P_S(\omega)} = \frac{1}{\cosh(\Gamma L)+\frac{V_T}{V}k\Gamma L\sinh(\Gamma L)} \quad (2)$$

where the parameter L is the tubing length, V is the internal volume of the tubing, k is the polytropic factor and Γ is the wave propagation factor. The wave propagation factor is further defined as

$$\Gamma = \frac{\omega}{a}\left[\frac{\gamma J_0(i^{3/2}s)}{kJ_2(i^{3/2}s)}\right]^{1/2} \quad (3)$$

for which a is the mean velocity of sound, J_n is the Bessel function of the first kind of order n, and γ is the ratio of specific heats. The polytropic constant, k, models the wave compression and expansion and is defined as

$$k = \left[1+\frac{\gamma-1}{\gamma}+\frac{J_2(i^{3/2}s\sqrt{Pr})}{J_0(i^{3/2}s\sqrt{Pr})}\right]^{-1} \quad (4)$$

where Pr is the Prandtl number and s is the shear wave number which provides a measure of the tube wall shear effects as a function of tubing diameter, D, air density, ρ, and viscosity, μ.

$$s = \frac{D\sqrt{\rho\omega}}{2\mu} \quad (5)$$

Bench-top tests were designed to experimentally determine the transfer function, (1), and compare the results to the analytic transfer function, (2). Having validated the relationship, the analytic transfer function was then utilized to reconstruct attenuated and distorted signals. The reconstructed signals were then compared to the reference signals, validating accurate reconstruction.

Experimental Methods

Two bench-top experiments were conducted to describe the transfer function relating the reference unsteady pressure, P_S, to the pneumatically attenuated pressure, P_T, illustrated in Figure 49. For the acoustic configuration, Figure 49a, sinusoidal pressure waves were generated from a loud-speaker in a closed volume for specified frequencies. An Endevco 2-psi fast response sensor was used as the reference transducer to quantify the un-attenuated pressure wave. Tygon tubing was used to connect the closed volume of the loud-speaker to a single pressure port on a 5-psi Esterline ESP. The pressure measured by the ESP represented the pneumatically distorted signal. This configuration was utilized since the approach is easily implemented. However, the signal generated is of a low pressure, is limited in the frequency content by the frequency rating of the speaker (20-280 Hz), and is not readily adaptable to in-situ calibration.

A second bench-top setup was constructed and modeled after the Whitmore et al.[2] and Strike et al.[3] configurations, shown in Fig 2b. Compressed air was used to pressurize an accumulator tank, which was connected to a solenoid valve, which led into a pressure manifold. The reference transducer and the pneumatic tubing were connected to the manifold such that equivalent pressures were applied to both. A semi-infinite tubing line was also connected to the manifold and performed as a anti-resonance tube bundle, which allowed for signal conditioning of the step response. The step-function pressure wave was generated by the opening of the valve. The benefit of this configuration is that the compressed air source generated pressure signals of much higher pressure ranges as compared to the acoustic configuration. Additionally, the step response allowed for modeling of sharp transitions from low-to-high-pressures, and for the determination of the spectral response of all of the odd frequencies up to the Nyquist sampling frequency.

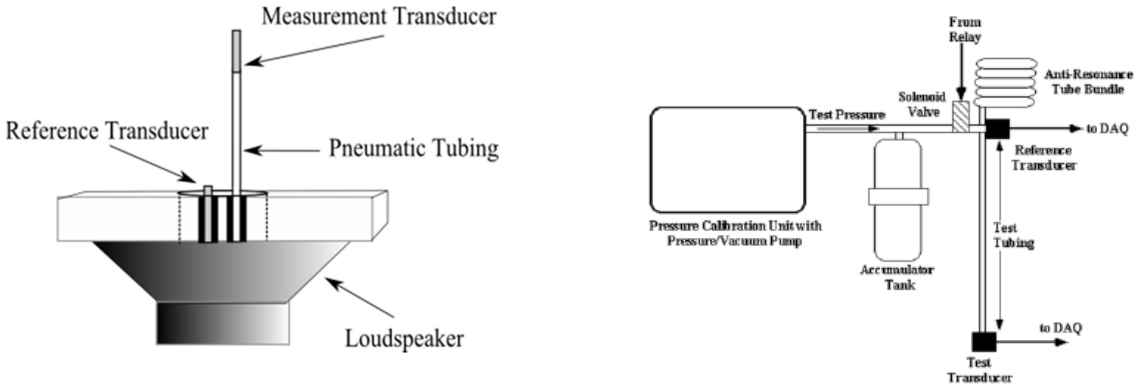

(a) (b)

Figure 49: (a) Acoustic and (b) step-response [2] bench-top block diagrams used to determine the pneumatic tubing transfer function

Both bench-top experiments were performed using an 18-inch length of Scanivalve Tygon tubing with an inner diameter of 0.034 ± 0.004 in. The acoustic configuration generated sinusoidal pressure waves at frequencies of 5 to 300 Hz at 5 Hz increments, and the transfer function was established at each increment. Data was collected at a sampling frequency of 1 kHz. The acoustic tests were performed for three different ESP pressure ports to establish uniformity within the ESP. The results presented for the step-function configuration are the ensemble averages of 250 tests. The data acquisition frequency was 3 kHz and 28 samples were collected per test.

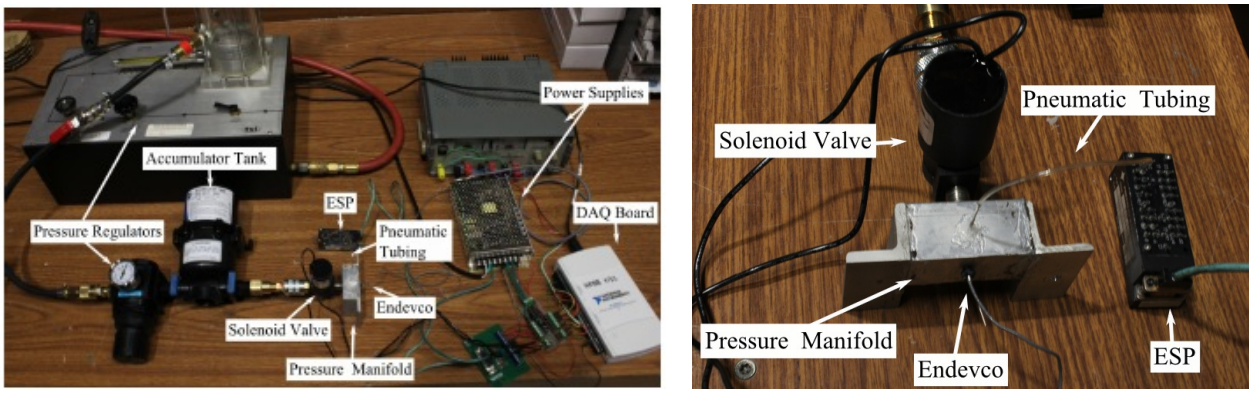

(a) (b)

Figure 50: (a) Step-response bench-top configuration with (b) an enlarged image of the solenoid valve and pressure manifold

Results

The experimental transfer function for both methods was found as the ratio of the pneumatic response to that of the reference signal in the frequency domain, Equation (1) Bode plots of the transfer function gain and magnitude from the experimental results are compared against the Bergh and Tijdeman analytic model [1] and are shown in Figure 51. For frequencies up to the speaker rating (280 Hz), the results from the acoustic and step-function experiments are in good agreement and within the analytic transfer function uncertainty. At higher frequencies, the experimental results from the step-function tests become noise dominated and diverge from the analytic model at approximately 600 Hz. This divergence is attributed to system limitations in the experiment. At frequencies above 600 Hz, the step-function pressure wave reaches a noise-threshold, indicated in the gain and phase plots.

The noise-threshold is further illustrated in Figure 52. An FFT was applied to both the reference and pneumatic signals from the step-response and the magnitudes are shown in Figure 52a. The signal-to-noise ratio, SNR, of both the reference and pneumatic signals are shown in Figure 52b. Both plots approach a mean constant minimum value at frequencies greater than 600 Hz, corresponding to the noise-threshold observed in the transfer function Bode plots. Beyond this threshold, the signal contains mostly white noise with noise on the same magnitude as the signal, indicated by a SNR of approximately 1.

To demonstrate the capabilities of the established transfer function, pneumatic pressure signals were reconstructed and compared to the reference signal. For the reconstruction, various pressure waves were generated, and data was collected at a sampling rate of 1kHz, such that

the Nyquist frequency was below the noise threshold. Figure 53 shows the reconstruction of multi-frequency signals using the acoustic bench-top configuration. Additionally, the reconstruction of the step-response is also shown in Figure 54. The results indicate that the established transfer function is capable of reconstructing a variety of signals for a broad frequency range.

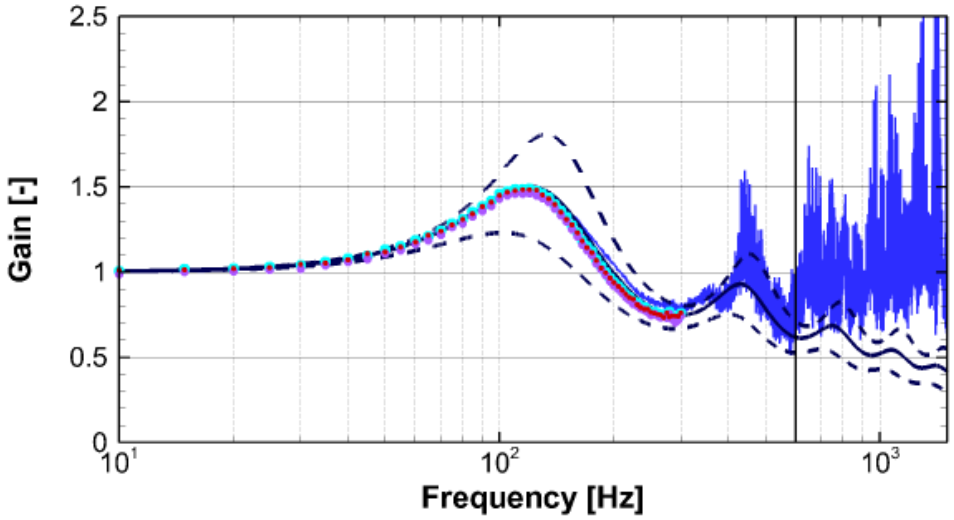

(a)

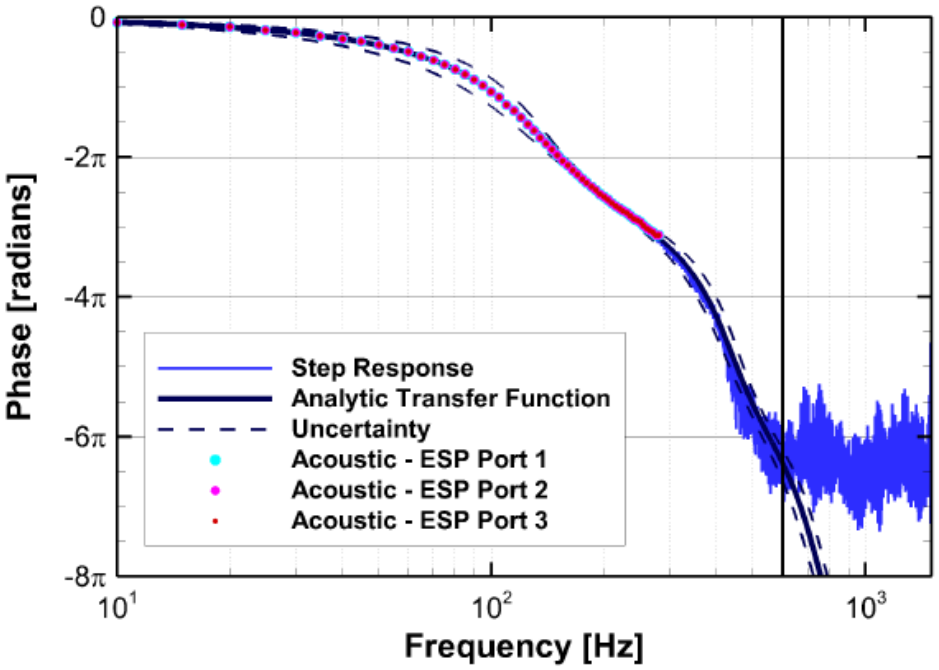

(b)

Figure 51: Transfer function (a) gain and (b) phase for 18-inch tubing from experimental results and Bergh and Tijdeman analytic model [1].

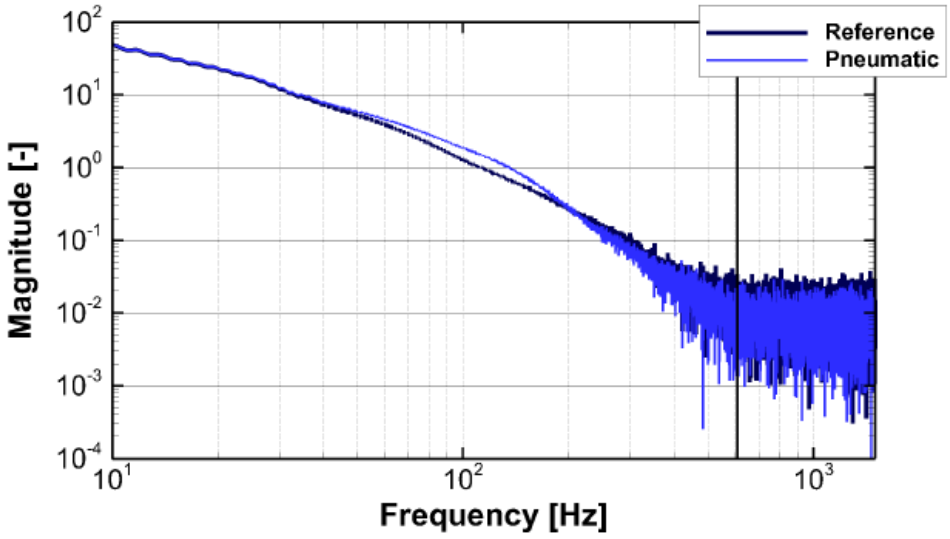

(a)

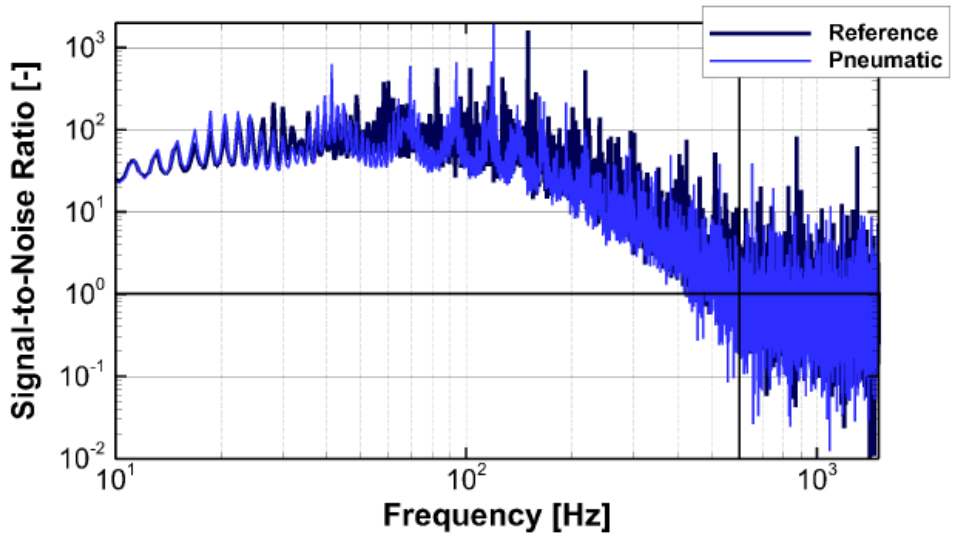

(b)

Figure 52: (a) FFT of pressure step-responses and (b) signal-to-noise ratios of the reference and pneumatically attenuated signals with noise threshold indicated at 600 Hz.

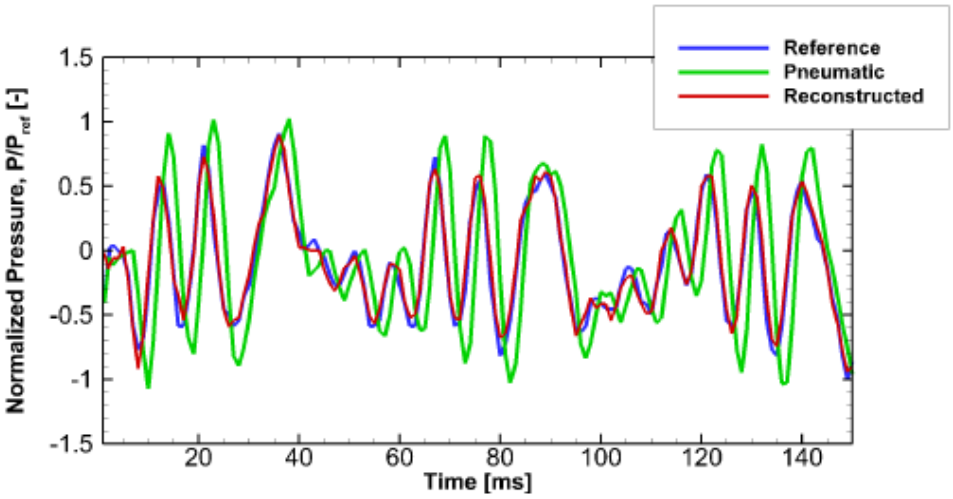

(a)

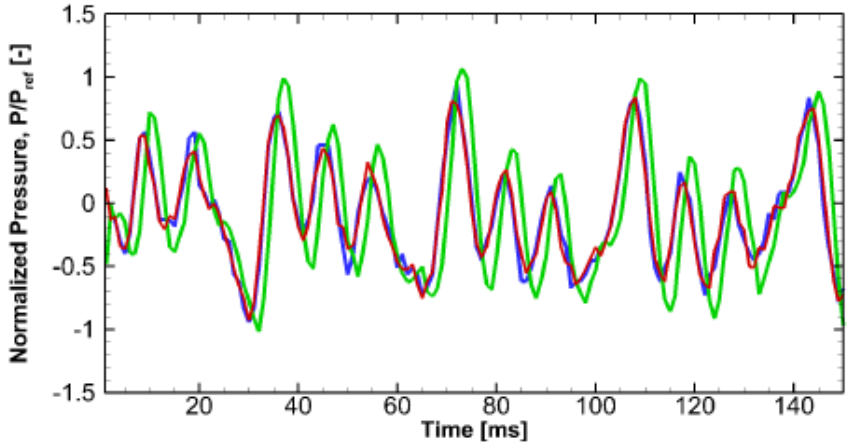

(b)

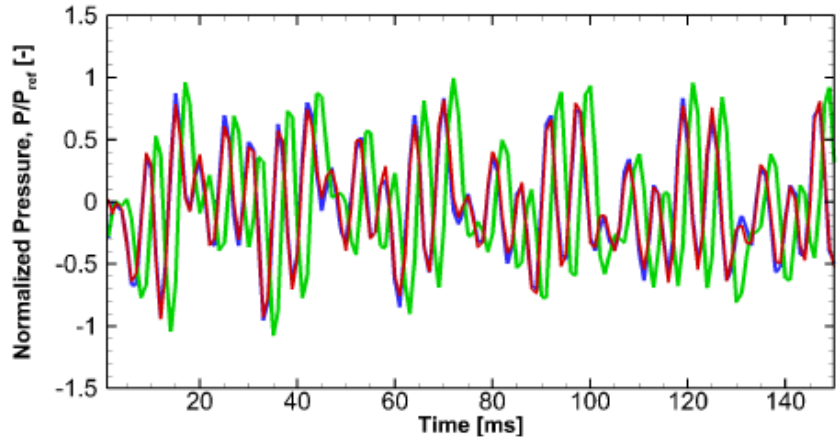

(c)

Figure 53: Reconstruction of multi-frequency signal (a) 4, 22, 40, 57, 75, 93, 110, 128 Hz, (b) 4, 31, 57, 84, 110 Hz, and (c) 4, 40, 75, 110, 145, 180 Hz for 18-inch length Tygon tubing.

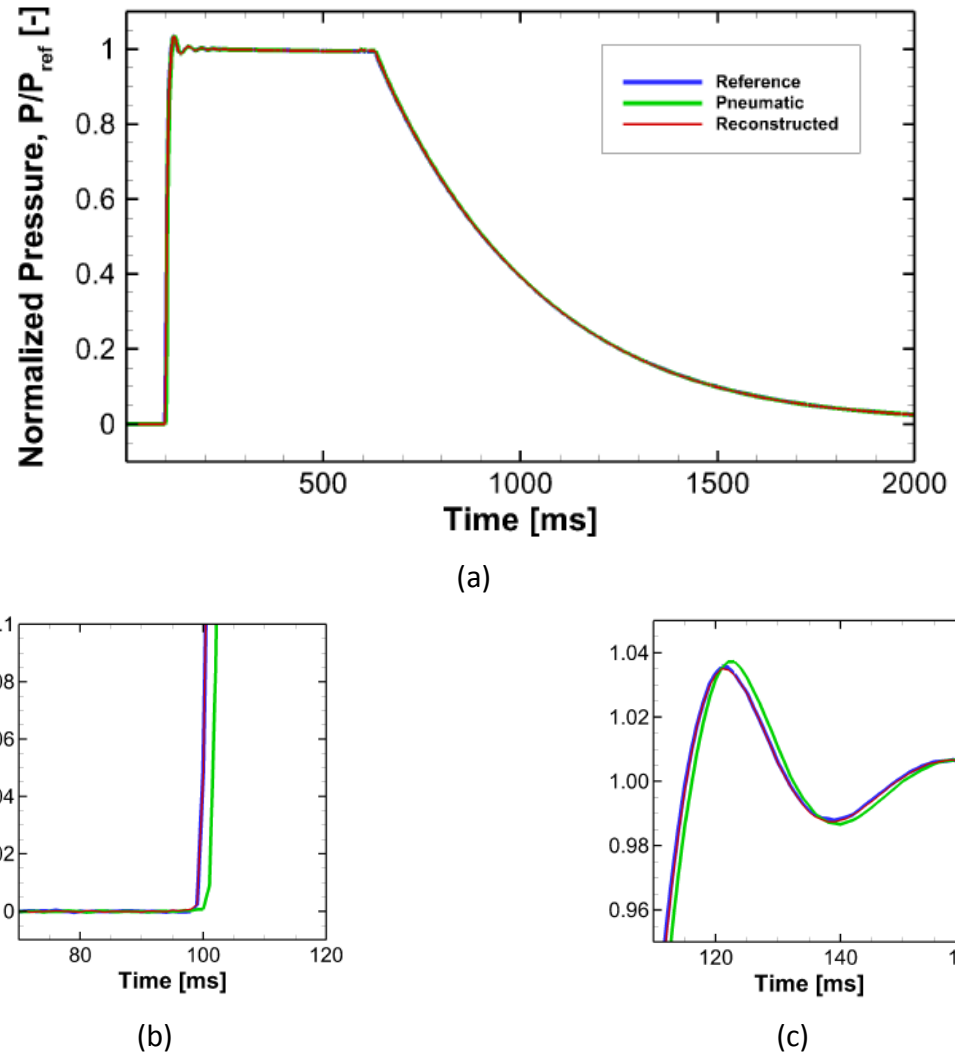

Figure 54: Reconstruction of (a) step function with close-up on (b) initial impulse and (c) overshoot for an 18-inch length Tygon tubing.

Conclusions

Two bench-top experiments were performed to establish the experimental transfer function of a pneumatic system for 18-inch length Tygon tubing. The experimental results were then compared to the analytic Bergh and Tijdeman transfer function and were found in good agreement up to 280 Hz. From 280 to 600 Hz, the experimental results from the step-response bench-top configuration are within the analytic uncertainty. Above 600 Hz, the signals reach a noise threshold and the experimental transfer function deviates from the analytic model. The capabilities of the transfer function were demonstrated by the reconstruction of the attenuated pressures as compared to reference signals. The results indicate that the transfer function is capable of reconstructing signals up to 600 Hz.

References

1. Bergh H., and Tijdeman H., “Theoretical and Experimental Results for the Dynamic Response of Pressure Measuring Systems," National Aero and Astronautical Research Institute, Amsterdam, Report NLR-TRF, 1965, pp. 328.
2. Whitmore S., Wilson M. D., and Eilers S. D., “Novel Technique for Reconstructing High-Frequency Transient Rocket Chamber-Pressure Measurements," *Journal of Spacecraft and Rockets*, Vol. 47, No. 3, 2010.
3. Strike J., Hind M. D., Saini M. S., Naughton J. W., Wilson M. D., and Whitmore S., “Unsteady Surface Pressure Reconstruction on an Oscillating Airfoil Using the Wiener Deconvolution Method," *Mechanical Engineering*, July 2010.

Appendix B: Coordinates of the VR-7 with 3 Degree, 4% tab

X/C	Y/C
1.000000	0.000719
0.998725	0.000656
0.994713	0.000452
0.988286	0.000124
0.982533	-0.000170
0.979558	-0.000322
0.972688	-0.000672
0.962887	-0.001202
0.956679	-0.001608
0.948328	-0.002224
0.940678	-0.002758
0.929307	-0.003520
0.920373	-0.004136
0.910828	-0.004806
0.900065	-0.005566
0.885672	-0.006586
0.877576	-0.007163
0.864494	-0.008096
0.854996	-0.008774
0.841323	-0.009741
0.823737	-0.010948
0.808968	-0.011909
0.796290	-0.012685
0.781617	-0.013538
0.764011	-0.014514
0.754161	-0.015044
0.738650	-

X/C	Y/C
	0.015870
0.722667	-0.016722
0.709640	-0.017419
0.697383	-0.018073
0.681444	-0.018920
0.665745	-0.019751
0.655457	-0.020298
0.643081	-0.020956
0.633453	-0.021468
0.618053	-0.022283
0.606293	-0.022904
0.593633	-0.023570
0.583689	-0.024098
0.571569	-0.024735
0.557582	-0.025474
0.545017	-0.026148
0.534180	-0.026733
0.524382	-0.027271
0.513130	-0.027877
0.501569	-0.028472
0.488496	-0.029084
0.475199	-0.029633
0.459342	-0.030211
0.444461	-0.030702
0.430106	-0.031133
0.415266	-

X/C	Y/C
	0.031516
0.401564	-0.031800
0.388038	-0.032012
0.372035	-0.032171
0.359144	-0.032221
0.340709	-0.032195
0.324389	-0.032112
0.310031	-0.032009
0.298499	-0.031905
0.287022	-0.031783
0.273968	-0.031619
0.261080	-0.031429
0.250701	-0.031256
0.237762	-0.031012
0.227646	-0.030794
0.214407	-0.030467
0.203459	-0.030173
0.192376	-0.029859
0.182918	-0.029558
0.172010	-0.029150
0.162850	-0.028763
0.156166	-0.028463
0.145612	-0.027958
0.135119	-0.027396
0.127451	-0.026935
0.120016	-

X/C	Y/C
	0.026442
0.113495	-0.025973
0.105953	-0.025387
0.100137	-0.024905
0.093405	-0.024318
0.087493	-0.023773
0.080322	-0.023079
0.073034	-0.022310
0.066270	-0.021537
0.060621	-0.020861
0.054918	-0.020165
0.047625	-0.019224
0.040302	-0.018194
0.034562	-0.017334
0.027340	-0.016099
0.023910	-0.015429
0.021529	-0.014923
0.018760	-0.014279
0.016134	-0.013599
0.014066	-0.013005
0.013115	-0.012712
0.012202	-0.012416
0.010785	-0.011922
0.009795	-0.011546
0.008324	-0.010926
0.007340	-0.010458
0.006201	-0.009843
0.005187	-

X/C	Y/C
	0.009211
0.004374	-0.008628
0.003587	-0.007974
0.002641	-0.007021
0.002172	-0.006454
0.001628	-0.005688
0.001035	-0.004658
0.000638	-0.003755
0.000366	-0.002920
0.000175	-0.002074
0.000077	-0.001408
0.000037	-0.000987
0.000000	0.000000
0.000075	0.001513
0.000508	0.003502
0.001034	0.005078
0.001937	0.007068
0.003215	0.009287
0.004857	0.011648
0.007301	0.014624
0.010204	0.017683
0.013294	0.020512
0.016204	0.022855
0.019479	0.025279
0.024115	0.028457
0.029065	0.031529
0.034398	0.034592
0.039630	0.037346
0.047162	0.040947
0.052875	0.043514
0.059026	0.046127
0.070347	0.050487
0.079208	0.053564
0.088547	0.056665
0.098601	0.059815
0.107870	0.062426

X/C	Y/C
0.116159	0.064540
0.126299	0.067007
0.136099	0.069288
0.151427	0.072500
0.166097	0.075140
0.177421	0.076985
0.190260	0.079015
0.201068	0.080610
0.213627	0.082209
0.226745	0.083633
0.239667	0.084849
0.254975	0.086056
0.264733	0.086695
0.282663	0.087601
0.301095	0.088207
0.319827	0.088495
0.336985	0.088477
0.351732	0.088265
0.372057	0.087732
0.395172	0.086844
0.411138	0.086008
0.428774	0.084827
0.440336	0.083924
0.453004	0.082846
0.468285	0.081441
0.479383	0.080346
0.494144	0.078781
0.507962	0.077198
0.526069	0.074968
0.539055	0.073268
0.551177	0.071608
0.563612	0.069834
0.577118	0.067813
0.597264	0.064653
0.610719	0.062486
0.624810	0.060192
0.636643	0.058262
0.651635	0.055822
0.666575	0.053396
0.679700	0.051259
0.698057	0.048246

X/C	Y/C
0.716153	0.045254
0.736054	0.041968
0.751313	0.039471
0.771478	0.036198
0.787647	0.033576
0.806846	0.030431
0.827900	0.026848
0.843089	0.024124
0.856674	0.021593
0.874227	0.018185
0.886250	0.015762
0.897739	0.013380
0.911865	0.010362

X/C	Y/C
0.922290	0.008073
0.930173	0.006298
0.938371	0.004388
0.941600	0.003640
0.943297	0.003261
0.945063	0.002893
0.947342	0.002475
0.948680	0.002271
0.950074	0.002094
0.951171	0.001979
0.952315	0.001882
0.954138	0.001778
0.955577	0.001739

X/C	Y/C
0.957127	0.001740
0.959847	0.001843
0.961402	0.001922
0.967176	0.002217
0.974230	0.002577
0.981654	0.002956
0.989048	0.003333
0.993640	0.003567
0.997393	0.003759
1.000000	0.003881

Appendix C: Optimal Pressure Tap Locations

Id	X/C	Y/C
1	1.24020	0.00040
2	1.20950	-0.00117
3	1.09300	-0.00924
4	0.98259	-0.01661
5	0.86172	-0.02312
6	0.74484	-0.02932
7	0.61786	-0.03603
8	0.51891	-0.03940
9	0.40545	-0.04014
10	0.32777	-0.03931
11	0.24428	-0.03743
12	0.15805	-0.03359
13	0.08200	-0.02682
14	0.05854	-0.02390
15	0.03641	-0.02053
16	0.02484	-0.01818
17	0.01309	-0.01476
18	0.00413	-0.00963
19	0.00009	0.00189
20	0.00430	0.01204
21	0.01188	0.02123
22	0.02112	0.02923
23	0.02872	0.03463

Id	X/C	Y/C
24	0.03991	0.04150
25	0.06212	0.05263
26	0.08635	0.06254
27	0.14503	0.08063
28	0.21026	0.09436
29	0.27478	0.10363
30	0.33171	0.10842
31	0.39389	0.11057
32	0.46030	0.10981
33	0.51963	0.10716
34	0.59027	0.10133
35	0.65089	0.09456
36	0.71049	0.08641
37	0.77751	0.07581
38	0.84080	0.06551
39	0.89938	0.05588
40	0.95976	0.04599
41	1.02480	0.03531
42	1.08750	0.02378
43	1.14520	0.01178
44	1.21040	0.00284
45	1.23990	0.00435

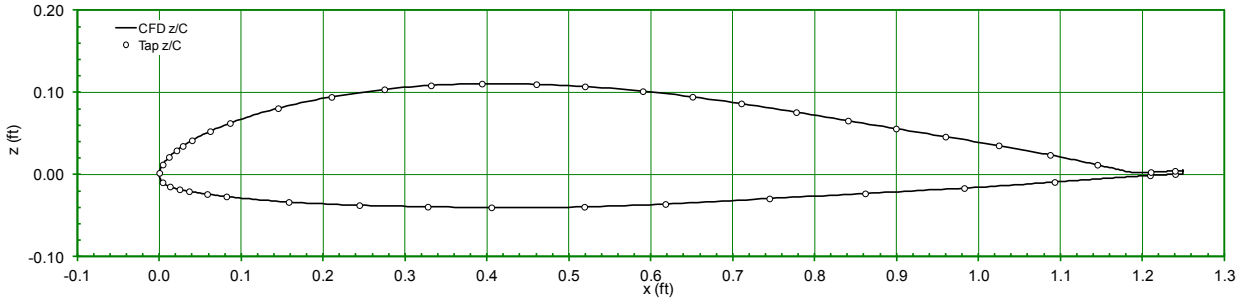

REPORT DOCUMENTATION PAGE

Form Approved
OMB No. 0704-0188

1. REPORT DATE *(DD-MM-YYYY)*	2. REPORT TYPE	3. DATES COVERED *(From - To)*
01-01-2014	Contractor Report	

4. TITLE AND SUBTITLE

Investigation of Active Flow Control to Improve Aerodynamic Performance of Oscillating Wings

5a. CONTRACT NUMBER

NNL13AA03C

5b. GRANT NUMBER

5c. PROGRAM ELEMENT NUMBER

6. AUTHOR(S)

Narducci, Robert P.; Bowersox, Rodney; McVeigh, Michael; Raghu; White, Edward

5d. PROJECT NUMBER

5e. TASK NUMBER

5f. WORK UNIT NUMBER

380046.02.07.03.02.02

7. PERFORMING ORGANIZATION NAME(S) AND ADDRESS(ES)

NASA Langley Research Center
Hampton, Virginia 23681

8. PERFORMING ORGANIZATION REPORT NUMBER

9. SPONSORING/MONITORING AGENCY NAME(S) AND ADDRESS(ES)

National Aeronautics and Space Administration
Washington, DC 20546-0001

10. SPONSOR/MONITOR'S ACRONYM(S)

NASA

11. SPONSOR/MONITOR'S REPORT NUMBER(S)

NASA/CR-2014-218146

12. DISTRIBUTION/AVAILABILITY STATEMENT

Unclassified - Unlimited
Subject Category 34
Availability: NASA CASI (443) 757-5802

13. SUPPLEMENTARY NOTES

Langley Technical Monitor: Brian G. Allan

14. ABSTRACT

The objective of this effort is to design a promising active flow control concept on an oscillating airfoil for on-blade alleviation of dynamic stall. The concept must be designed for a range of representative Mach numbers (0.2 to 0.5) and representative reduced frequency characteristics of a full-scale rotorcraft. Specifications for a sweeping-jet actuator to mitigate the detrimental effects of retreating blade stall experienced by edgewise rotors in forward flight has been performed. Wind tunnel modifications have been designed to accommodate a 5x6 test section in the Oran W. Nicks Low Speed Wind Tunnel at Texas A&M University that will allow the tunnel to achieve Mach 0.5. The flow control design is for a two-dimensional oscillating VR-7 blade section with a 15- inch chord at rotor-relevant flow conditions covering the range of reduced frequencies from 0.0 to 0.15 and Mach numbers from 0.2 to 0.5. A Computational Fluid Dynamics (CFD) analysis has been performed to influence the placement of the flow control devices for optimal effectiveness.

15. SUBJECT TERMS

CFD; dynamics stall; flow control; fluid dynamics; rotor; sweeping jet

16. SECURITY CLASSIFICATION OF:			17. LIMITATION OF ABSTRACT	18. NUMBER OF PAGES	19a. NAME OF RESPONSIBLE PERSON
a. REPORT	b. ABSTRACT	c. THIS PAGE			STI Help Desk (email: help@sti.nasa.gov)
					19b. TELEPHONE NUMBER *(Include area code)*
U	U	U	UU	77	(443) 757-5802